

Alma Mater Studiorum-Università di Bologna

DOTTORATO DI RICERCA IN
MECCANICA E SCIENZE AVANZATE DELL'INGEGNERIA

Ciclo 34

Settore Concorsuale: 09/A2- MECCANICA APPLICATA ALLE MACCHINE

Settore Scientifico Disciplinare: ING-IND/13- MECCANICA APPLICATA ALLE
MACCHINE

**NUMERICAL AND EXPERIMENTAL ANALYSIS OF 3D PRINTED
SMART STRUCTURES AND SYSTEMS**

Presentata da: **Mohamed Refat Mosatafa Ramadan**

Coordinatore Dottorato
Marco Carricato

Supervisore
Rocco Vertechy

Co-supervisore
Alfonso Pagani

Esame finale anno 2022

THIS PAGE IS INTENTIONALLY LEFT BLANK.

NUMERICAL AND EXPERIMENTAL ANALYSIS OF 3D PRINTED SMART STRUCTURES AND SYSTEMS

BY

MOHAMED REFAT

Submitted to the Department of Industrial Engineering
on May 16, 2022, in Partial Fulfillment of the Requirements for the
Degree of Doctor of Philosophy in Mechanics and Advanced Engineering Sciences

ABSTRACT

Flexure-based compliant mechanisms (CMs) open up novel possibilities for enriching smart structures performance. However, it is elusive, if not possible, to produce such structures with the conventional materials and processing techniques. As a result, devising novel materials and manufacturing process that seamlessly integrate such functionalities is required. Three dimensional (3D) printers of continuous fiber reinforced composites, such as MarkTwo (MT) by Markforged, can be used to manufacture such structures. To date, research works devoted to the study and application of flexible elements and CMs realized with MT printer are only a few and very recent. A good numerical and/or analytical tool for the mechanical behavior analysis of the new composites is still missing. In addition, there is still a gap in obtaining the material properties used (e.g. elastic modulus) as it is usually unknown and sensitive to printing parameters used (e.g. infill density), making the numerical simulation inaccurate.

Consequently, the aim of this thesis is to present several work developed. The first is a preliminary investigation on the tensile and flexural response of Straight Beam Flexures (SBF) realized with MT printer and featuring different interlayer fiber volume-fraction and orientation, as well as different laminate position within the sample. The second is to develop a numerical analysis within the Carrera's Unified Formulation (CUF) framework, based on component-wise (CW) approach, including a novel preprocessing tool that has been developed to account all regions printed in an easy and time efficient way. Among its benefits, the CUF-CW approach enables building an accurate database for collecting first natural frequencies modes results, then predicting Young's modulus based on an inverse problem formulation. To validate the tool, the numerical results are compared to the experimental natural frequencies evaluated using a digital image correlation method. Further, we take the CUF-CW model and use static condensation to analyze smart structures which can be decomposed into a large

number of similar components. Third, the potentiality of MT in combination with topology optimization and compliant joints design (CJD) is investigated for the realization of automated machinery mechanisms subjected to inertial loads in particular, a pusher mechanism is considered.

Finally, we hope that the developed models in this thesis would help unlock the full potential of 3D printing, in particular, fused deposition modeling technique for smart structures design, and CUF-CW tool as an analysis tool of such printed parts and for the optimization of printed laminated composite.

Thesis Supervisor: Rocco Vertechy

Title: Professor of Mechanics of Machines

Thesis Co-Supervisor: Alfonso Pagani

Title: Associate Professor of Aerospace Structures

Giovanni Berselli

Title: Professor of Mechanical Engineering & Robot Design

Thesis Reader

Marco Fontana

Title: Associate Professor of Mechanics of Machines

Thesis Reader

ASTRATTO

I meccanismi con elementi flessibili, noti col termine inglese “Compliant Mechanisms” (CM), consentono la realizzazione di strutture intelligenti ad alte prestazioni. Tuttavia, produrre tali strutture con i materiali e le tecniche di lavorazione tradizionali è molto difficile. Grazie al recente sviluppo delle tecniche di produzione additiva, una possibilità per la realizzazione di queste strutture è la stampa tridimensionale (3D) di compositi a matrice polimerica rinforzati con fibre continue, ad esempio mediante la stampante MarkTwo (MT) di Markforged. Ad oggi, poche sono le ricerche dedicate allo sviluppo e all'applicazione di strutture flessibili e CM realizzate con 3D-MT. Non sono ancora disponibili, infatti, strumenti numerici e/o analitici che consentano di predire il comportamento meccanico dei nuovi compositi stampati, e di analizzare i componenti meccanici o le strutture fatti con essi. La correlazione tra i parametri di stampa (ad esempio, la densità di riempimento e la modalità di deposizione delle fibre) e le caratteristiche meccaniche (ad esempio, il modulo elastico) del composito realizzato è inoltre ancora abbastanza sconosciuta.

In questo contesto, lo scopo di questa tesi è di gettare le basi per la risoluzione di questi problemi. Una prima attività svolta riguarda lo studio sperimentale del comportamento a trazione e a flessione di lamine rettilinee flessibili (Straight Beam Flexures, SBF) realizzate mediante 3D-MT e caratterizzate da diverse frazioni volumetriche e disposizioni delle fibre all'interno del medesimo strato e in strati differenti. La seconda attività riguarda lo sviluppo di uno strumento per l'analisi numerica di queste SBF, basato sulla formulazione unificata di Carrera (Carrera Unified Formulation, CUF) utilizzando l'approccio “component-wise” (CW), che include un nuovo elemento di pre-elaborazione che consente di considerare tutte le regioni stampate in modo semplice e con un ridotto tempo computazionale. Tra i suoi vantaggi, l'approccio CUF-CW consente di raccogliere le frequenze naturali dei primi modi di vibrare e di prevedere il modulo di Young del composito sulla base di una formulazione del problema inverso. Per convalidare lo strumento, i risultati numerici sono confrontati con le frequenze naturali valutate sperimentalmente mediante un approccio basato sulla correlazione di immagini digitali. Come terza ed ultima attività, le potenzialità della stampa mediante MT, in associazione con l'ottimizzazione topologica e la progettazione di meccanismi con membri/giunti flessibili (Compliant Joint Design, CJD), sono state investigate nel contesto della realizzazione di meccanismi per macchine automatiche soggetti a carichi inerziali. In particolare, un meccanismo spingitore è stato riprogettato e ottimizzato per essere prodotto mediante la stampante MT con l'obiettivo di ridurre la

coppia motrice richiesta al movente.

Dedication

This work is dedicated for my father, Refat Ramadan, and my mother, Amina Omara. For caring their four children, educating and loving. Making us believe that there is no wall for knowledge. I aspire to one day to be as successful as them. May Allah keep them safe and reward them with the highest level of all rewards... Amen.

ACKNOWLEDGEMENT

I would like to thank so many. All gratitude is due solely to God (Allah) for his inestimable mercy and blessing, which he has bestowed upon his salves. My country (Egypt) for its munificence, by it I learned much civilization. I would like to thank my family for their never-ending love and support throughout the years: My Mother for always being there for me, her great love, dedication and bringing a smile to my face, by her I would like to be move onward. My Father for his support and encouragement, by him I would like to be inspired. My older sister Prof. Rania, who supported me a lot during my entire life, my siblings Rania (again :)), Dina, and Mostafa, for always supporting me, especially with their childern "Ahmed (Habozo), Kenzy (Fotna), Bissan (Bisanovo), Refat (Krombolosti), Rital".

I would like to thank my advisor Prof. Rocco Vertechy for his support during the period even with a lot of politics confrontation. Also, I would like to thank my co-advisor Prof. Alfonso Pagani for his unlimited support and guidance throughout this thesis. Prof. Pagani had an indescribable impact on my development as a scientist and I will be forever indebted to him. Thank you. Special thanks go to my inspiring and role professor, Prof. Erasmo Carrera, who I have worked and had conversation during my time at PoliTO, by him I would like to be guided.

I would like also to thank the Italian Ministry of Foreign Affairs and International Cooperation (MAECI) for supporting me under PhD fellowships scheme for foreign and Italian citizens living abroad awarded by the Italian Government. Namely, Drs. Susi Baldasseroni and Mario Izzi from the (MAECI) and Prof. Claudio Margottini from the Italian Embassy in Cairo.

Many thanks to all the MUL2 group members, from whom I learned a lot across the period at Polito. My time here in Turin has been enjoyable because of all the great friendships: (in alphabetical order) Alberto Majano, Prof. Enrico Zappino, Marco Enea (Che-ca.), Rodolfo Azzara (Rudi always teach me "come non perdere il treno"), Riccardo Augello (Riccardissimo). Also, many thanks to my friends from Bologna Ivo Campione and Roberto Di Leva (8:10). My friends from Egypt for their constant support and longterm friendship: Malik Wagih (who is now just got his PhD from MIT and will be a famous professor soon), Mohamed Ezz, Mohamed Samir and Khaled Khafagy. A special thanks goes to Profs. Josep Costa, Pere Maimí (Master supervisor), Jordi Renart, Iman El Mahallawi, khalil elkhodary, and Tarek Hatem for their support and friendship.

Outline

1 Introduction	1
1.1 Context	1
1.2 Research Objectives and Thesis Outline	2
2 Background and Motivation	5
2.1 Three Dimensional Printing	6
2.1.1 Vat Photo-Polymerization	7
2.1.2 Binder Jetting	8
2.1.3 Material Jetting	8
2.1.4 Material Extrusion Process	8
2.1.5 Powder Bed Fusion	9
2.1.6 Sheet Lamination	9
2.1.7 Directed Energy Deposition	10
2.2 Compliant Structures and Mechanisms	10
2.3 Flexure-Based Compliant Mechanism	15
3 Mechanical Characterization	18
3.1 Description of Mark Two Printer	18
3.2 Preliminary Experimental Study	22
3.2.1 Samples Manufacturing	22
3.2.2 Experimental Results and Discussion	24
3.3 Analytical Models	28
3.3.1 Classical Laminate Theory (CLT)	28
3.3.1.1 Preliminary Design of MT Beam	34
3.3.2 Volume Averaging Stiffness Method (VAS)	37
3.3.3 Analytical Models Verification	40
3.4 Conclusion	44
4 Numerical Approach	47
4.1 Numerical Background and Motivation	47

4.2	Structural Formulation	50
4.2.1	Preliminary Considerations	50
4.2.2	Carrera Unified Formulation	52
4.2.2.1	Layer Wise	52
4.2.3	High Fidelity Modeling of 3D Printed Structure	55
4.3	Modeling Techniques and Guidelines for MT Structures	58
4.3.1	CUF Requirements and Installtion	59
4.4	Numerical Results	59
4.4.1	Analysis of MT Printed Beams	63
4.5	New Approach for FDM/MarkTwo Material Characterization	67
4.5.1	Infill Material Characterization	68
4.6	Experimental Verification	70
4.7	Static Condensation	71
4.8	Conclusion	74
5	Industrial Application	76
5.1	Introduction	77
5.2	The Original Mechanism and the New Design Procedures	78
5.2.1	Mechanism Fabrication by MT	80
5.2.2	Substitution of Links and Kinematic Pairs with CJ	82
5.2.3	Size Optimization of the Flexible MT Laminates	82
5.2.4	Mechanical Dissipation Experimental Analysis	84
5.3	Results	85
5.4	Conclusion	86
6	Future Work Directions	88
6.1	Experimental Characterization	88
6.2	Numerical Analysis	89
6.3	Compliant Joint Application	90

List of Figures

Figure 1.1	Graphical illustration of the thesis work	4
Figure 2.1	Example of generic process of AM/3D printing technology (i.e. prosthetic hand)	7
Figure 2.2	Scheme of different 3D printing techniques	8
Figure 2.3	Scheme of material jetting process	9
Figure 2.4	Scheme of different 3DP techniques	10
Figure 2.5	Scheme of different 3DP techniques	12
Figure 2.6	Conceptual illustration of compliant mechanism and rigid body mechanism . .	13
Figure 2.7	Comparison between S_y to E ratio, and R for different materials	14
Figure 2.8	Several 3DP techniques with the corresponding materials, and polymerization methodologies	14
Figure 2.9	Conceptual illustration of flexure-based compliant structure	16
Figure 3.1	MarkTwo printer desktop	19
Figure 3.2	Schematic overview of the matrix and reinforcement feeding system of MT desktop printer	19
Figure 3.3	Graphical user interface of different options of Eiger software (GUI-Eiger) . .	20
Figure 3.4	Top view of a slice of printed part with different infill patterns: a) Triangular, b) Hexagonal and c) ± 45 Rectangular	21
Figure 3.5	Top view of a slice of printed part with different infill patterns: a) Concentric, b) Isotropic	21
Figure 3.6	Example of tensile specimens configurations	23
Figure 3.7	Mechanical test benches	25
Figure 3.8	Stress-strain curves	26
Figure 3.9	Bending test results	27

Figure 3.10	Laminate geometry of typical deformation in the x-z plane	29
Figure 3.11	Example of tensile specimens configurations	41
Figure 3.12	E_T with various infill density and pattern	43
Figure 4.1	MT Laminated beam and its related Cartesian coordinate system	50
Figure 4.2	Example of typical solid MT cross-section discretized by; a) Four, b) Nine, c) sixteen Lagrange points	53
Figure 4.3	Representation of the finite element (FE) and Lagrange expansion (LE) theories employed over the macroscale structure of MT printed laminated solid beam	54
Figure 4.4	Component-wise approach	55
Figure 4.5	Left: Cross section L9 expansion discretization, middle: FEM discretization four noded beam element of MT printed laminated honeycomb (infill) beam, Right: Top view of the printing features of the infill region with triangular pattern	56
Figure 4.6	Assembly procedure of the stiffness matrix through ESL, LW and CW approaches	58
Figure 4.7	Flow diagram of the novel CUF 3D	60
Figure 4.8	Example of CUF-3D input file	61
Figure 4.9	a) The fifty-layer nylon printed beam, b) The fifty-layer CFN printed beam	62
Figure 4.10	Mesh Convergence Study for σ_{yy} with different beam elements at L9	62
Figure 4.11	Mesh Convergence Study for σ_{yz} with different beam elements at L9	63
Figure 4.12	Distribution of stresses through the thickness of a cantilever beam (ISO CB): left) σ_{yy} , right) σ_{yz}	64
Figure 4.13	Distribution of stresses σ_{yy} through the thickness of a composite cantilever beam (ORTCB)	65
Figure 4.14	Distribution of stresses σ_{yz} through the thickness of a composite cantilever beam (ORTCB)	65
Figure 4.15	Distribution of stresses σ_{yy} through the thickness of a composite fixed ended beam (ORTFE)	66
Figure 4.16	Distribution of stresses σ_{yz} through the thickness of a composite fixed ended beam (ORTFE)	67
Figure 4.17	Flowchart for the new approach of predicting material properties of 3D-FDM structure	68

Figure 4.18	Left: Infill beam considered for infill component material characterization, right: Top view of infill part within the beam	69
Figure 4.19	Scatter plots comparing the observed frequency for first mode of the various FDM infill beams	70
Figure 4.20	Left: Electro-dynamic shaker testing system, right: digital image correlation . .	71
Figure 4.21	a) Left: Generic isotropic solid FDM structure with equivalent single layer (Taylor), Right: Layerwise (Lagrange polynomials); b) Left: Generic FDM composite structure with equivalent single layer (Taylor), Right: Layerwise (Lagrange polynomials)	72
Figure 5.1	Stephenson six-bar planar linkage	79
Figure 5.2	Schematic of original pusher mechanism	79
Figure 5.3	a) Schematic of original pusher mechanism, b) novel mechanism proposed . . .	81
Figure 5.4	Kinematic equivalent mechanism	83
Figure 5.5	Test platform for the damping measurement	85
Figure 5.6	Kinematic equivalent mechanism	86
Figure 5.7	RMS motor torque surface	87

List of Tables

Table 2.1	Comparison of different 3DP techniques	11
Table 3.1	Sample codes	22
Table 3.2	Samples part settings used for comparison between experimental and proposed analytical models	41
Table 3.3	Comparison of measured and predicted elastic moduli and Poisson's ratio	42
Table 3.4	Mechanical properties of the matrix materials obtained by Markforged under ASTM D638	46
Table 3.5	Mechanical properties of the reinforcement materials obtained by Markforged under ASTM D638	46
Table 4.1	Details of Taylor expansion	54
Table 4.2	Material properties and LSS used for the numerical analysis	61
Table 4.3	Comparison of DOF, stresses generated from various models	64
Table 4.4	Comparison of stresses generated from various models for fixed ended beam . .	66
Table 4.5	Validation of results between experimental and CUF-CW modeling of various Infill percentages	71
Table 4.6	Models parameters used for static condensation verification	73
Table 4.7	Comparison of Displacement obtained by full K and condensed matrix	74
Table 5.1	Mechanism dimensions	80
Table 5.2	Material properties used and LSS	85

List of Acronyms

3D – CAD Three-dimensional computer Aided Design

3DP Three-dimensional printing

4DP Four-dimensional printing

ζ Damping ratio

ABS Acrylonitrile butadiene styrene

AM Additive manufacturing

AMed Additive manufactured

CAM Computer aided manufacturing

CCBF Circular curve beam flexure

CFRT Carbon fiber reinforced thermoplastic

CJ compliant joints

CJD Compliant joints design

CNC Computer numerical control

CS Compliant structure

DOD Drop on demand

E Young's modulus

FDM Fused deposition modeling

FRP Fiber-reinforced plastic

HSHT high strength high temperature

MST Material subtractive techniques

MT MarkTwo

PA Polyamide

PC Polycarbonate

PDC Product development cycle

PLA Polylactic acid

PMCs Polymer matrix composites

PRB Pseudo-rigid-body

R Material resilience

RMS Root mean square

RP Digital image correlation

RP Rapid prototyping

SBF Straight beam flexure

SO Size optimization

STL STereoLithography

STL Standard tessellation language

S_y Yield strength

TMT Traditional manufacturing techniques

TO Topology optimization

CUF Carrera Unified Formulation

CW Component wise

ESL Equivalent single layer

HLE Hierarchical Legendre expansion

LE Lagrange polynomials

LPs Lagrange points

LW Layer-wise

MC3DPS Multicomponent 3D printed structures

TE Taylor expansion

Chapter 1

Introduction

1.1 Context

Machine structural elements, and mechanical robots are primarily made of hard materials, which restrict their ability to steer/maneuver nimbly in constrained environments or adapt their shape in response to stimuli [1]. A novel design paradigm of adaptive soft structure is to exploit the structural instability triggered by loss of stiffness (elastic instabilities), to create well-behaved shape adaption and multi-functional structure [2–7]. It is elusive, if not possible, to produce such structures with the conventional materials, and manufacturing techniques. Consequently, the development of new materials and manufacturing techniques that can be integrated and produce such structures is a challenge. Further, devising novel numerical and/or analytical tools to analyze/predict the mechanical response of such new structures is required.

Three-dimensional printing (3DP) technology, “also referred to as, additive manufacturing (AM)”, has the ability to produce complex composite structure with high functionalities and without typical waste of materials compared to the conventional manufacturing techniques [8]. 3DP of composite structures provides the ability to control precisely different materials properties including thermal, optical, physical, and electro-chemical. Such benefits may also result in transformations of the printed structures shape leading to the so called four dimensional printing (4DP) [9].

Generally, 3DP of polymers is used in a wide variety of high-tech applications, for example, to print organs and tissues in biomedical engineering industries [10], to create complex lightweight structures in aerospace industries [11], as well as creating structural models in architecture field [12]. However, 3D printed (3DPed) polymer parts are known to suffer from low strength, and lack of end user load bearing parts. Such limitations restricts the adoption of 3DPed polymer parts from it's severe applications [13]. 3DP of polymer matrix composites has recently been proposed to address the shortcomings of 3DPed polymer structures. The proposed solution is to use fused deposition modeling (FDM) to deposit continuous fiber reinforcement in a polymer matrix to achieve a more useful and functional structure/system.

The literature review revealed that many studies focus on 3DP of short fibers, and their relevant parameters on mechanical and fracture properties, and only few cases addressed the 3DP of continuous fibers polymer composites [13]. In addition, there is a lack of comprehensive studies that focus on 3DP of soft structures. The choice of the fiber-reinforced plastic (FRP) composites is due to its high strength to weight, and stiffness to weight ratios [14]. Most of 3DP/FDM procedures for fiber reinforced composite materials are still under development, and a number of problems still remain unsolved. To name a few: alignment of fibers, weak debonding between fibers and polymer matrix, and void formation during the printing process that can lead to delamination. For design and verification purposes, a major issue is the lack of knowledge on the dependency of material properties on process parameters, such as the infill percentages, as obtaining them via experimental techniques are expensive and can not cover all parameter variations. Novel modeling tools based on a good understanding of material sensitivity and new experimental paradigms are therefore needed for the development of reliable 3DPed adaptive soft structures made of plastic composites.

1.2 Research Objectives and Thesis Outline

As previously mentioned, 3DP introduces a new paradigm on how products are designed and fabricated [15]. Among various 3DP technologies, FDM is a promising technique that is gaining a wide recognition for producing complex continuous fiber reinforced composites parts regardless of manufacturing skills or labour cost [16, 17], and thanks to the availability of affordable machines that are easy to use and minimize waste of material [18, 19], and variety of materials that can be used including plastics, ceramics, composites and metal powder [20–22]. Despite the results available in the literature, there is still a gap in fully understanding FDM and optimizing the related process in producing finished composite parts which can be employed in the industrial field. In addition, there is still a very limited understanding of the dependency of the material properties of the 3DPed composite structure on the process parameters, which cannot be found solely via experimental investigation as it would be excessively expensive to cover all parameter variations. In this thesis, we aim to address these gaps in the literature, by developing a preliminary experimental investigation paradigm for producing flexible beams and a computational framework to handle and elucidate the mechanical responses. In particular, the aim of this work is to answer the following questions:

- What is the proper position of the reinforcement filaments within the printed part to produce a straight beam flexure ? Could it also provide an effective mean to tune the selective compliance ?
- Can we have a numerical and/or analytical tool to predict and analyse the mechanical response of the FDM printed part? Could the numerical tool be with very low computational cost with accurate results ?
- Would it be possible to predict the material properties of the FDM-MT printed structures based on various infill densities with the numerical tool instead of performing experimental testing?
- Would it be possible to combine FDM-MT, topology optimization (TO), and Compliant joints design (CJD), to optimize the performances of automated machinery mechanisms subjected to inertial loads ?

Therefore, the thesis will use a combination of analytical, experimental and numerical work to answer the above mentioned questions and is structured as described in the following (Fig. 1.1). Chapter 2 presents an overview of additive manufacturing including various 3D printing techniques available together with a literature review of compliant mechanisms. Chapter 3 provides a preliminary experimental investigations of the influence of reinforcement amount, position and printing pattern on the the mechanical response of printed carbon fiber reinforced composites. Specifically, tensile and bending experimental tests are performed on nine different specimens. Envisaged application of printed specimens is as flexible elements in compliant mechanism. Moreover, it lists and discusses the capabilities of both the classical laminate theory (CLT) and volume average stiffness method (VAS) models to predict the elastic properties. Comparison of models results and experimental results is provided with the aim of understanding the effect of various parameters on the printed samples. Chapter 4 provides an accurate numerical analysis/modeling of MT parts and responds to the need of a comprehensive numerical assessment of various theories within the CUF framework at low computational cost. It also includes a novel preprocessing platform within the Carrera's Unified Formulation (CUF) which easily describes the modeling parameters and discretization in an accurate and time efficient way that accounts all the details of the MT printed component. Lastly, Chapter 5 illustrates the potentiality of FDM in combination with TO and CJD for the optimization of automated machinery mechanisms subjected to inertial loads.

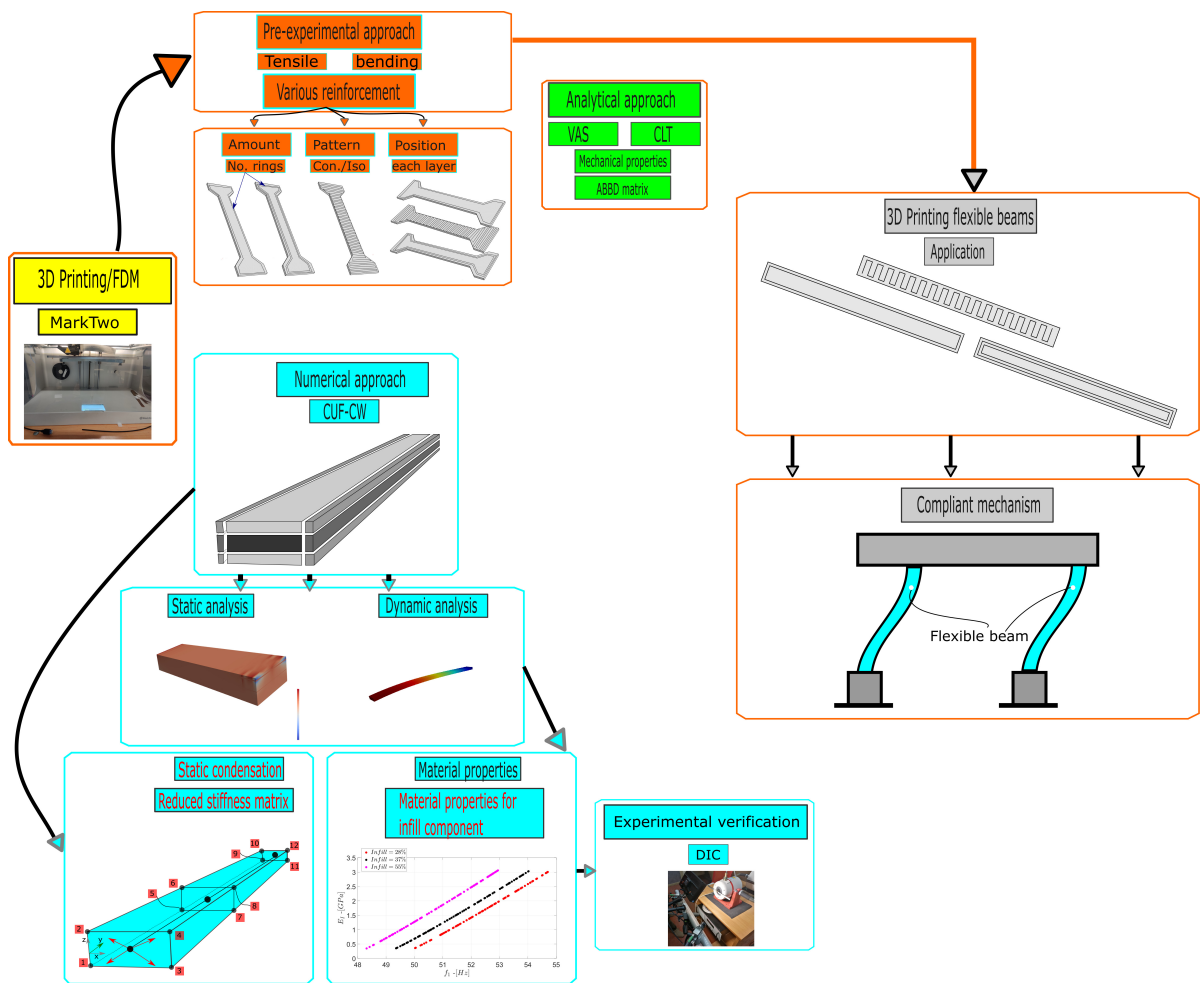


Figure 1.1: Graphical illustration of the thesis work

Chapter 2

Background and Motivation

Additive manufacturing (AM) is referred to the rapid prototyping (RP) and three-dimensional (3D) printing technologies. AM was initially applied to simple model making (e.g. visualization model) that is usually demanded to validate and understand the purpose of the designer when presenting the conceptual design. For example, 3D printing technique is used for expeditiously fabricating parts (e.g. prototypes) in a variety of applications, from which final product or further development will be derived.

Successively, AM technology has evolved as accuracy, material, and final product quality are improved. Moreover, models were rapidly utilized to deliver information about form, fit, and function that is formalized as 3Fs. In this latter, form describes the general intent of the design, and understand the shape. Fit represents the ability of the parts to be built to the tolerances required for assembly objectives. Function refers to the novel material properties, which means the parts could be managed so that they could be determined based on how they would work [23]. For such focal process, RP users' have found the term inaccurate to describe the process and undervaluing it's numerous applications. The advancement in the output product quality makes AM machines directly produce many parts that are closer to the final product quality. This required formalizing a new terminology that thoroughly describe the process and it's recent applications by one of the American Society of Testing and Materials (ASTM) Technical committees'. In the meanwhile, the term RP is essentially evolved to additive manufacturing [24, 25]. Nowadays, AM is considered to be one of a series of disruptive technologies that are changing the conventional way of product development or set up a new business in a new and effective way. Generally, traditional manufacturing techniques (TMT) requires a precise investigations of the part geometry to determine a process planning such as appropriate tools, techniques, and additional fixtures that maybe necessary to complete the production of the final part. In contrast, the concept of 3DP is based on physical prototype generated directly from complex three-dimensional computer Aided Design (3D-CAD) tool, without the need for process planning or any further fixtures. The next section is about the latest methods of AM and especially 3D printing, which earlier was developed only for prototyping, but now, is extended to manufacturing purposes.

2.1 Three Dimensional Printing

3D printing technology was initially invented/introduced by Charles Hull in the 1980s [13, 26] for constructing models and prototype components [27–29]. It has a number of advantages including fabricating complex geometries that cannot be produced by TMT, overheads minimization and human friendly interaction, and hence expedite product development cycle (PDC). Currently, the high tech tool 3D printing with the advancement in plastic material allowing the addition of reinforcement, has broaden its capabilities to produce finished components. Further, it can be adopted to produce complex parts by integrating CAD, computer aided manufacturing (CAM) and computer numerical control (CNC) [12]. Most of commercialized 3D printing machines produce components using layers of materials added together; each layer describes a finite 2D cross-section of the part generated from the 3D-CAD data. Reducing the layers thickness increases the resulting parts accuracy to the original 3D-CAD model. A number of factors have an influence on the materials and mechanical properties of the additive manufactured (AMed) structures; for example materials used, how the layers' are bonded together and their directions, and the way of the layers' are generated. It also affects the time required for producing the part as well as post-processing time, the size of the machine, and finally the total cost of both the process and machine [23]. 3D printing technique based on several stages involves translation of the CAD data into a physical fabricated part. 3D printing steps, and degrees are determined according to the size of the parts required. For example, complex large engineering parts may involve the 3D printing during various iterations, and steps throughout the whole product development stage. It also may require additional post-processing such as painting, cleaning, and priming before it's final release. Thus, the 3D printing is being useful for the intent without taking into account the tooling problems. Most AM/3D printing machines include 8 stages as shown in Fig. 2.1. 1) CAD: It includes the generation of the external geometry of the AM/3D printed part using any CAD solid model software. The output design should be a 3D solid model, or a surface representation created by optical or laser scanning. 2) Conversion to standard tessellation language (STL): the machine accepts only the CAD geometry in STL format. The STL represents the surface geometry without any texture and color, and also calculates the slices formed. 3) Transfer to AM/3DP machine: checking orientation, and size for building the output product. 4) Machine setup: it's considered a very important step as it includes energy sources, materials constraint, timing and layer thickness which should be settled preceding to the machine running. 5) Build: it is an automated process without any supervision, or human inter-

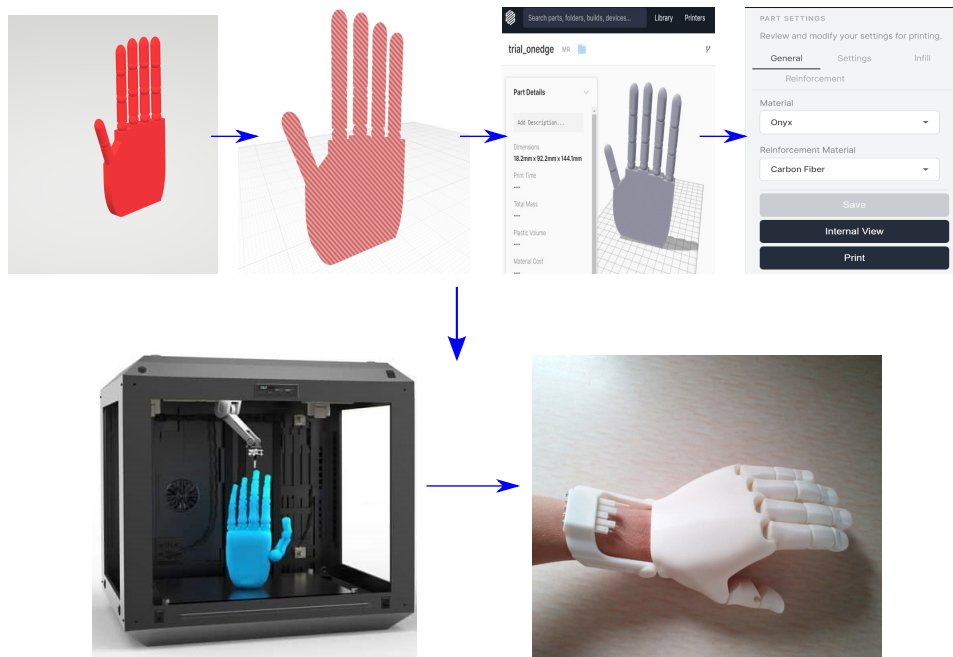


Figure 2.1: Example of generic process of AM/3D printing technology (i.e. prosthetic hand)

action; only few superficial monitoring must be considered (e.g. running out of power, or material). 6) Removal: the manufactured part must be removed once the machine has finished the part building. 7) Post-processing: experienced manual manipulation such as: careful cleaning, painting, and priming may be required to the produced part prior to its commercialization or final release. 8) Applications: after post-processing, the part is being ready for usage; however; specific applications require further treatment before it is being acceptable for using (e.g. surface treatment, and finishing) [23].

In the following sub-sections, a number of 3D printing processes will be reviewed.

2.1.1 Vat Photo-Polymerization

The model part is created by placing a vat of liquid photo-polymer resin layer over layer, then an ultraviolet light is applied over the specific area that needs to be cured. Worktable layout transfer produces components made downwards after each new layer is cured while more layers are built on top of the part. Some machines utilizes a blade to give a smooth resin base as shown in 2.2a.

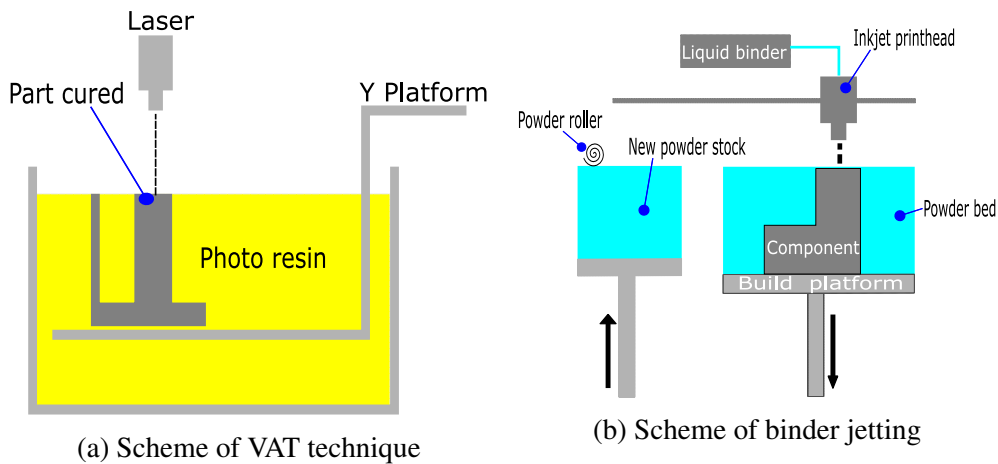


Figure 2.2: Scheme of different 3D printing techniques

2.1.2 Binder Jetting

It utilizes two materials: powder based material as a build material that is placed over the worktable layout via a roller and a binder as an adhesive on top of the powder where demanded. Print head /nozzle moves horizontally along the x and y axes of the machine and places alternative layer of both material. The powder material is placed over the worktable layout via a roller, whereas the print head places the binder adhesive. The worktable layout is lowered by the components' layer thickness as illustrated in Fig.2.2b.

2.1.3 Material Jetting

The idea of material jetting is similar/based on two dimensional (2D) inkjet printer. The printer head is positioned above the build worktable where the material is dropped continuously or by drop on demand (DOD) using either piezoelectric or thermal method. The dropped material/deposited material solidifies and first layer is then created; sometimes layers are cured by an ultraviolet light as shown in Fig.2.3.

2.1.4 Material Extrusion Process

FDM is a common material extrusion process and is trademarked by the Stratasys® company. Material is heated and then deposited via nozzle based on using a layer by layer approach. The nozzle moves horizontally along x and y direction and the worktable moves vertically after each layer is

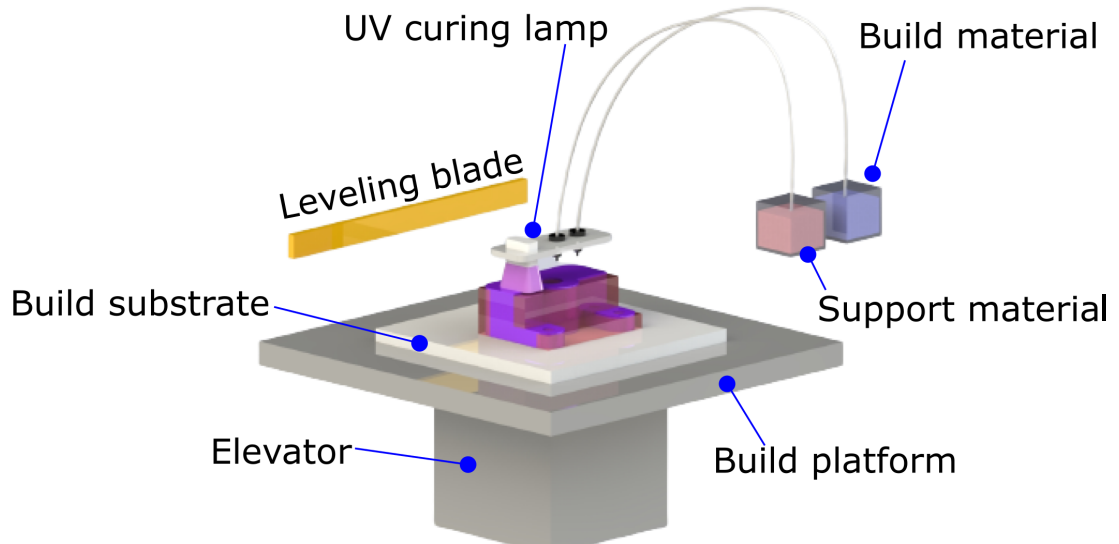


Figure 2.3: Scheme of material jetting process

created. Layers are bonded/fused together upon deposition as the material is in a melted state as shown in Fig.2.4a.

2.1.5 Powder Bed Fusion

The powder bed fusion (PBF) covers a number of terminologies: Direct metal laser sintering (DMLS), Electron beam melting (EBM), Selective heat sintering (SHS), Selective laser melting (SLM) and Selective laser sintering (SLS). Generally, PBF utilizes an electron beam or a laser to melt the material and powder together. EBM with metals and alloys is used to produce functional parts. The process of DMLS is same as SLS but it is used for metals instead of plastics. Opposed to other techniques, SHS uses a heated thermal print nozzle to fuse the powder material together. Layers are placed using a roller in between fusion of layers (Fig. 2.4b). SLS are now used for part production in aircraft industries.

2.1.6 Sheet Lamination

Sheet lamination includes laminated object manufacturing (LOM) and ultrasonic additive manufacturing (UAM) techniques/methods/processes. LOM is based on a layer by layer approach, however it uses paper as a material and adhesive for bonding layers together. Whereas, UAM utilizes ribbons or metal sheets, which are bonded together via ultrasonic welding. Additional CNC machining

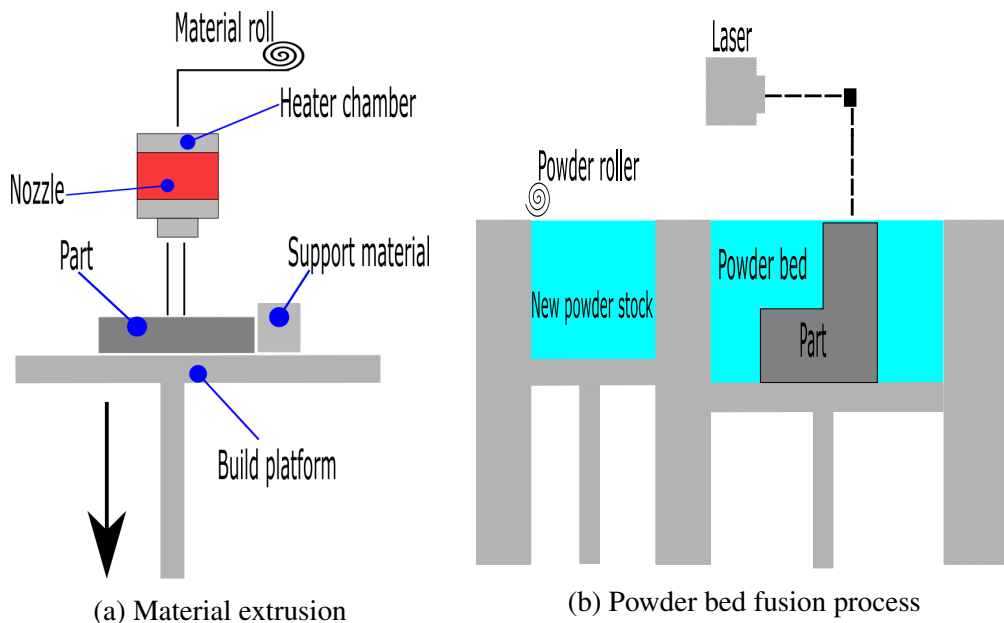


Figure 2.4: Scheme of different 3DP techniques

is required for the removal of unbounded metals. Fig. 2.5a shows a scheme of sheet lamination process.

2.1.7 Directed Energy Deposition

Directed Energy Deposition (DED) covers a number of terminologies, namely: Laser engineered net shaping, directed light fabrication, direct metal deposition, 3D laser cladding. It is considered the most complex printing process and mainly used to repair or/and modify material to existing parts. The DED machine includes a nozzle that is fixed on a multi axis arm, which places melted material over the platform, where it solidifies. The idea is similar to material extrusion process; however, opposed to material extrusion process, the nozzle has the ability to move in multiple directions. The material deposited can be in wire or powder form.

2.2 Compliant Structures and Mechanisms

The demand for a high level of multi-functional material in terms of strength, flexibility, and lightness coupled with the need for deployment in extreme environmental conditions, has increased in a wide range of engineering industries, particularly in aeronautics and space applications. To this end, advanced adaptive/smart structures have been developed to adapt, or alter their materials properties,

Table 2.1: Comparison of different 3DP techniques

3DP Technique	Advantages	Disadvantages
Vat Photo-polymerization	Fast process Very precise Large build areas	Costly Require post processing time Limited variety of material used
Binder jetting	Variety of material types can be used Considered to be the most fastest method	Not appropriate for structural parts Require support material
Material jetting	Very precise of deposition Multiple parts at the same printing time	Limited variety of material used Require support material
Material extrusion process	Cheap process ABS plastic can be utilized	The quality is limited by nozzle radius Printed structures have imprecise dimensions
Powder Bed fusion (PBF)	Inexpensive Good for visual models Variety of material types can be used Easily integration into a small scale	Long printing time Restricted printed size High powder usage Low material structural properties
Sheet lamination	Inexpensive Fast including fast cutting High quality with fast printing	Limited type of material used Finishes depending on plastic material Fusion methods require search
Directed Energy Deposition (DED)	Control structure to high degree	Limited type of material used

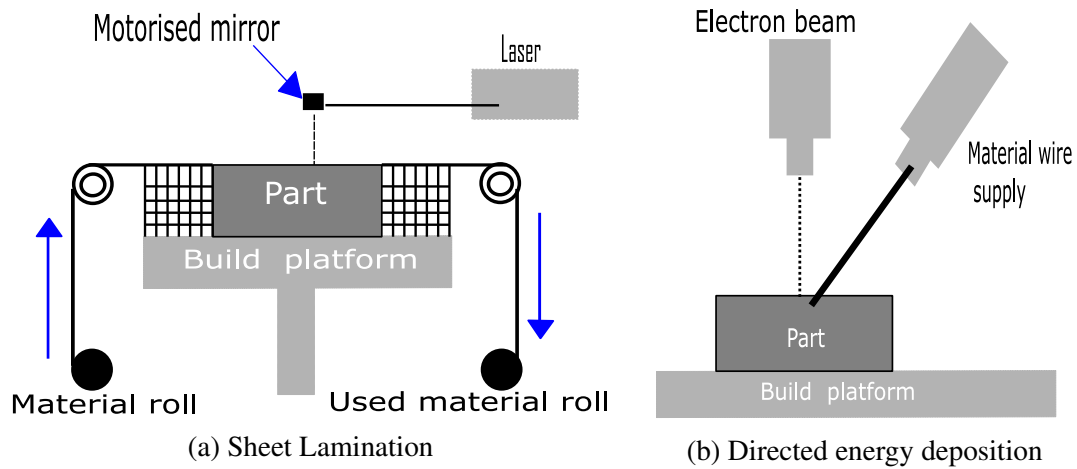


Figure 2.5: Scheme of different 3DP techniques

and/or geometric shape in response to external stimuli [30]. The literature review revealed that most adaptive structures tailor their shape via either inducing particular stress field into a structure [3–6, 31, 32] or altering the constituent materials properties [2, 33–40]. For example, a novel study by Arena et al. [2] demonstrated that adaptive structures are now capable of storing load before plastic deformation occurs, and therefore failure modes such as buckling will not consider being a catastrophic failure. In addition, adaptive compliant structure/mechanism can perform sophisticated tasks via the elastic strain/deformation of their parts and therefore it could be able to bear a load without being damaged [41–43]. Figure 2.6 presents the conceptual illustration of compliant mechanism compared to rigid body one. Unlike conventional structure, the compliant structure (CS) has the ability to combine various functions, with a minimum number of parts. This leads to numerous advantages that include no wear, backlash, or particles produced as well as no lubrication needed [30, 44–46]. CS is particularly applied to small-scale size and high precision applications as well as it's appropriate for a monolithic manufacturing [30, 47–49].

The fundamental concept of designing a reliable compliant structure is to exhibit a flexible and high strength material behaviour. This is useful, for instance, in flexible endoscopes which used to perform a minimally invasive procedure, which are capable to enter the body using a tiny holes as well as interact with very delicate structures in a very uncertain environment. When we design the compliant structure, we need to look for high strength with low Young's modulus material. This could be done by comparing the ratio of yield strength (S_y) to E , and resilience (R) of material (Equation. 2.1).

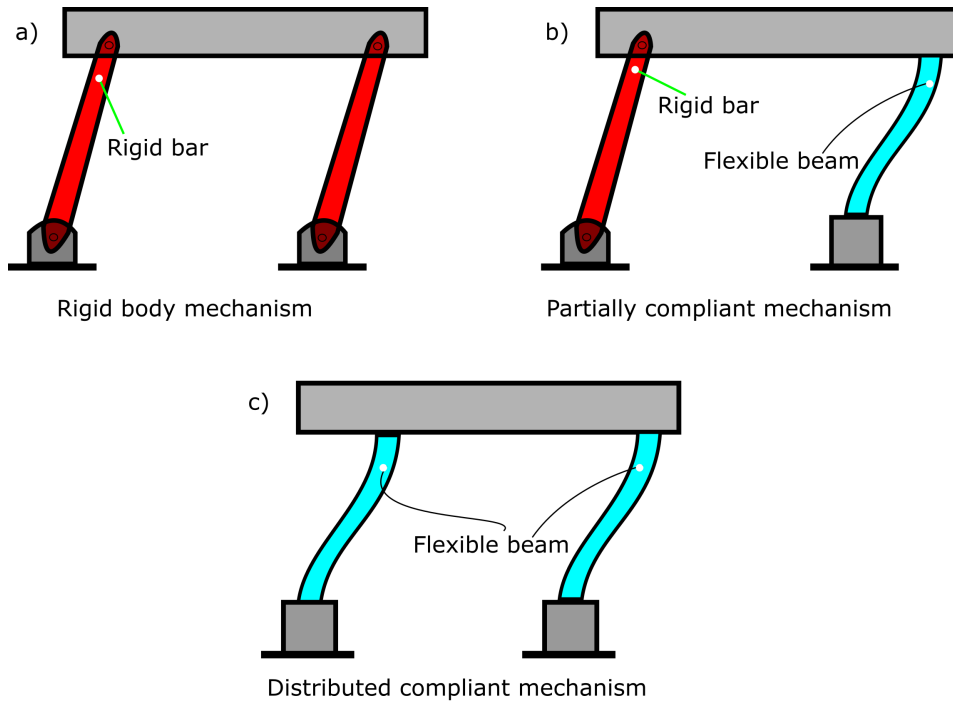


Figure 2.6: Conceptual illustration of compliant mechanism and rigid body mechanism

$$R = \frac{0.5 \times S_y^2}{E} \quad (2.1)$$

Figure 2.7 shows resilience, and yield strength to Young's modulus for several materials, showing the better properties of polymers. In addition, visco-elastic properties can cause a temporary bi-stability in a deformed shape; and when this bi-stability is lost, the structure shape returns to its initial configuration [33].

The choice of polymer materials in 3DP industry is due to its low weight, low cost, and processing flexibility [13]. For example, thermoplastic polymer materials including polyamide (PA)[50], polycarbonate (PC)[51], acrylonitrile butadiene styrene (ABS) [52–54], and polylactic acid (PLA)[52, 54, 55] as well as thermosetting polymer materials including epoxy resins could be 3D printed [13]. Epoxy thermosets require ultraviolet or heat assistance during the curing process to complete the polymerization. Moreover, the epoxy initially shows low viscosity, which increases sharply once the curing starts [56–58]. Hence, epoxy thermoset is highly appropriate for UV and thermal assisted printing process [13]. Figure 2.8 shows the several 3DP techniques with the corresponding materials, and polymerization methodologies [59, 60]. However, the 3DPed polymer products are known to suffer from modest mechanical properties and, thus, are typically not appropriate to produce end user load bearing

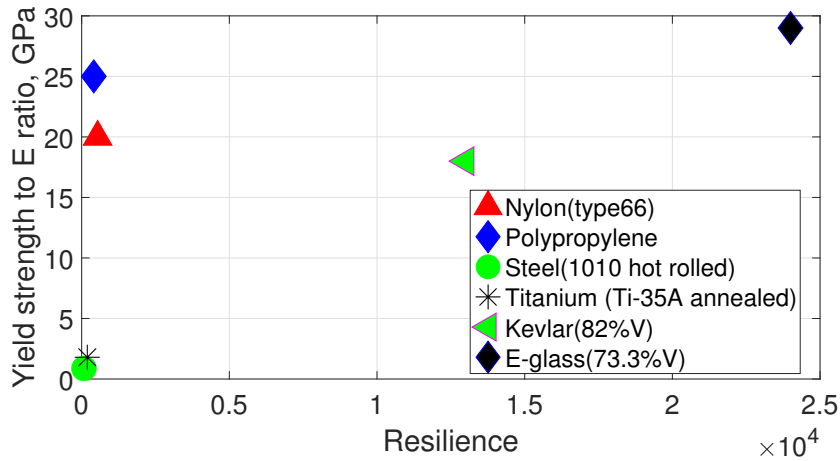


Figure 2.7: Comparison between S_y to E ratio, and R for different materials

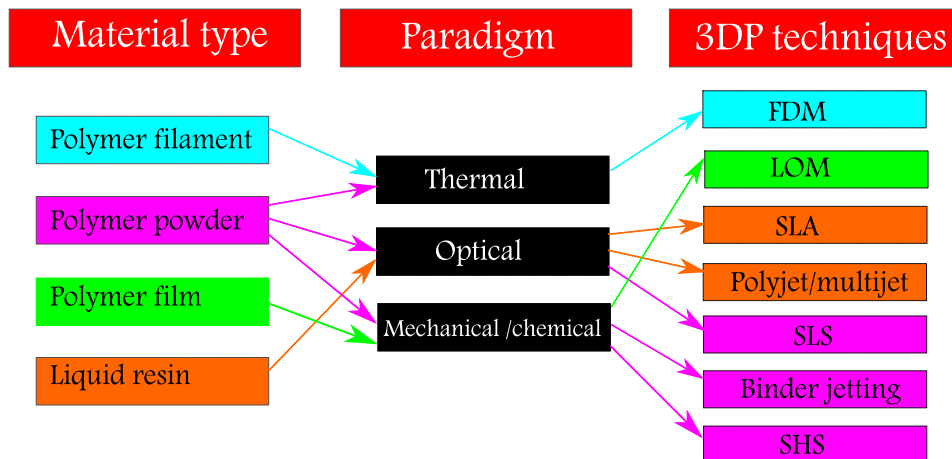


Figure 2.8: Several 3DP techniques with the corresponding materials, and polymerization methodologies

parts [13]. Therefore, it is important to find a way to reduce these limitations. Fabricating of PMCs parts via 3DP has been widely adopted for solving the drawbacks of low strength, by embedding reinforcements into a matrix to achieve a more useful and functional structure/system [13, 61]. In addition, reinforcements embedded into a structure can provide further functionalities including bio-compatibility as well as higher heat and electrical conductivity [62]. Several conventional manufacturing techniques including casting, machining, and molding have been used to produce composite components based on material removal process [13, 63]. These techniques are well studied and controlled; however, the ability to control the produced internal structure is still limited. Compared to the previous mentioned conventional techniques, 3DP technology has the ability to produce high functionality parts without

typical waste. Adjusting the CAD-model data controls the geometry and size precisely [13].

2.3 Flexure-Based Compliant Mechanism

Flexure-based compliant mechanism is a kind of mechanical system that employs flexural hinges in place of conventional kinematic pairs to realize articulated mechanisms which do not require lubricant or backlash but featuring limited range of motion [64] as depicted in Fig. 2.9. It is applied in a variety of applications, including minimally invasive surgery [64–66], micro-electro mechanical systems (MEMS) [67, 68], and spanning high precision manufacturing [69, 70]. Many studies have been carried out on the design and comparative analysis of straight beam flexures and compliant mechanism formation [71–73]. Lobuntiu and Collin [74] have compared compliance of two-segment circular axis symmetric notch flexure with a straight axis counterpart. Parvari Rad et al. [75] have analyzed the spatial compliance of circular curve beam flexure (CCBF) including different geometric configurations. Recently, Berselli et al. [76] have introduced CCBF and compared its compliance and achievable rotation with that of a straight beam. Although the above-mentioned research done, investigation on compliant hinges specially designed for spatial mechanism is still limited. Smith [77] introduced compliant universal joints manufactured from circular leaf springs, which deliver axial translation for self-alignment application. Nevertheless, the developed joints are influenced by substantial stress concentration that restricts their motion range [77]. Moon et al. [78] analyzed a compliant revolute hinge based on torsion beams of different geometric types. Machekpohsti et al. [79] obtained a compliant constant velocity double-hook universal joint by integrating two universal joints. In addition, several authors [80, 81] used two in-series connected flexure notch hinges with orthogonal axes to use fully compliant universal joints. Jacobsen et al. [82] developed lamina emergent flexures, and used them to create 3—RRR spherical mechanisms. However, the development of the above-mentioned mechanisms is usually a tedious process and fabricating them in a single step and without post-manufacturing assembly is always a challenge [83]. Hence, 3DP-FDM can be utilized as an attainable method for fabricating such mechanisms due to its many advantages and high flexibility compared to conventional manufacturing techniques [83]. A lot of research has been carried out on employing the use of additive manufacturing (AM) techniques to construct non-assembly mechanisms [83]. Yang et al. [84] produced kinematic pairs by SLM, and stated that multi-articulated mechanisms whose primary role is that of mechanical motion could be printed with a good accuracy using current AM technique without

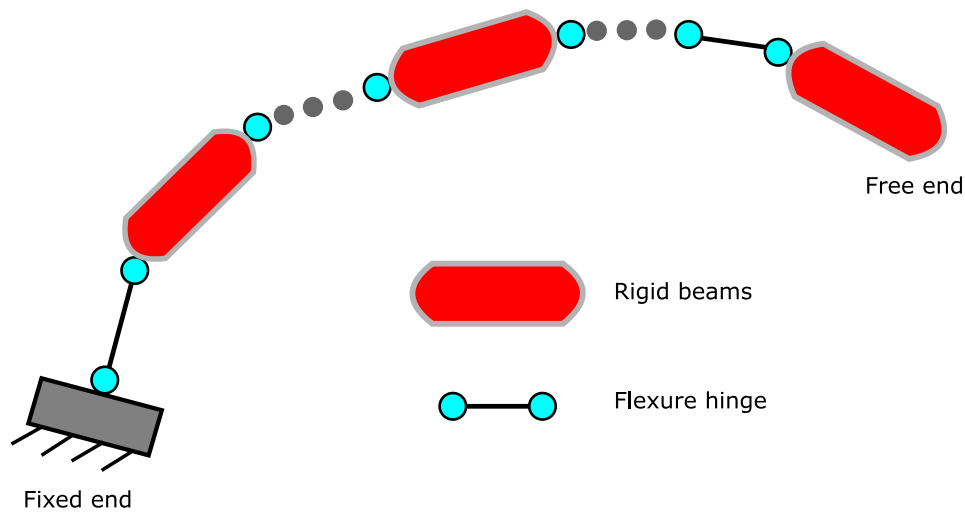


Figure 2.9: Conceptual illustration of flexure-based compliant structure

requiring any post-assembly procedures. Moreover, a number of research groups have successfully printed non-assembly mechanisms with good kinematic characteristics and satisfactory performance with several 3DP techniques. For example as in the following:

- (i) Soft robots that were printed using flexible materials and fluid [85, 86].
- (ii) Fully assembled actuators that are used with more extensive AM based techniques [87]
- (iii) Metallic joints [88–90]
- (iv) Polymer mechanisms [91–93]

Geometric configuration and printing materials feature the most important role in determining the mechanical performance of flexure hinges and mechanisms made thereof [94].

Various compliant shapes have been constructed to obtain distinctive motion types using different AM techniques [94]. For example, flexural hinge type joints were printed with SLS [95] and material extrusion [96, 97]. A trispiral joint and translational joint [98] were created with FDM. In addition, it has been revealed that AM is useful for reducing parasitic motion and providing stability, which both are considered predominant in the design of compliant joints. The addition of multiple joints and links to parallel layers was properly evaluated, and additional guidelines for compliant joint designs were provided to ensure the correct performance of compliant mechanisms [94]. Although 3DP shows the ability to produce successful non-assembly mechanisms, extensive evolution in the design and manufacturing of the above-mentioned examples shows that the scope of attainable mechanism

complexity still has substantial limitations [94]. It is crucial to meticulously grasp each 3DP technique to fully leverage their potentialities and minimize disadvantages in order to understand what level of mechanism complexity can be produced with a single-step fabrication [94]. In addition, thanks to their inherent energy-storing capabilities, compliant mechanisms have also been used to realize systems with prescribed load-motion profiles. Examples are gravity balancing mechanisms and stiffness compensators for smart-material actuators. A specific case of study is analyzed in this work in Chapter 5, which investigates the potentialities of compliant mechanisms to reduce the torque requirements of machines undergoing cyclic motions and subjected to predominant inertial loads. After introducing the underlying concepts, Chapter 5 describes a general design procedure that enables to synthesize the flexible elements of compliant mechanisms for given load and motion conditions and applies it to the realization of a compliant Stephenson six-bar linkage made of carbon fiber reinforced thermoplastic (CFRT) with FFF manufacturing process.

Chapter 3

Mechanical Characterization

In this chapter, a preliminary experimental investigation of the influence of reinforcement amount, position and printing pattern on the printed carbon fiber reinforced composites is presented. In particular, tensile and bending experimental tests are performed on nine different specimens. Envisaged application of printed specimens is as flexible elements in compliant mechanism. The application will be discussed separately in Chapter 5. Moreover, classical laminate theory (CLT) and volume average stiffness method (VAS) models developed earlier used to predict the elastic properties of the considered specimens, and verified to the experimental results with the aim of understanding the effect of various parameters on the printed samples. The obtained results are adopted later in the numerical analysis performed in Chapter 4. This chapter is organized as follows: Section 3.1 presents a general overview of the Mark Two[®] (MT) printer settings, various materials, and printing patterns; Section 3.2.1 describes specimens manufacturing and configuration considered for the experimental campaigns; Section 3.2.2 discusses the results and conclusion. Sections 3.3.1 and 3.3.2 also illustrate the applicability of both CLT and VAS towards the MT printed parts. Finally, some meaningful overall conclusions based on the above experimental and analytical analysis are reported in Section 3.4.

3.1 Description of Mark Two Printer

The specimens created for the preliminary mechanical characterization were printed by using a MT desktop printer. The MT printer is a compact printer with a print bed of a $320mm \times 231mm \times 154mm$ in length, width and height, respectively as shown in Fig. 3.1. This 3D printer series is unique as it has the capability of producing thermoplastic (e.g. nylon) parts embedded with continuous fiber reinforcements including carbon, glass, high strength high temperature (HSHT) fiberglass and kevlar. MT includes two nozzles, each nozzle connected to separate material spool in which the first nozzle is for printing matrix, whilst the other one is for reinforcement deposition as illustrated in Fig. 3.1b. The schematic overview of the matrix and reinforcement feeding systems of MT printer desktop is presented in Fig. 3.2. In the Fig. 3.2, teal color refers to the matrix filament system spool, while gray color

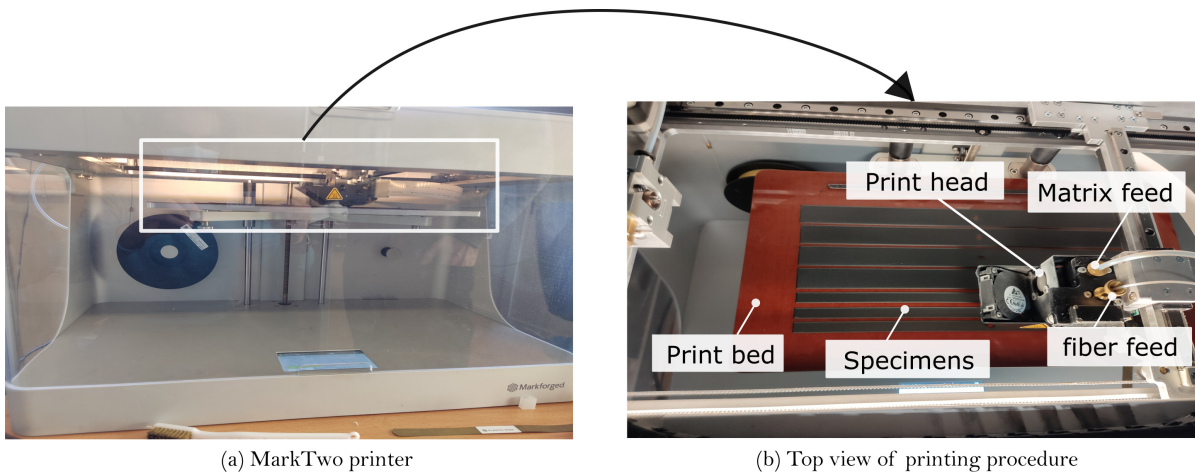


Figure 3.1: MarkTwo printer desktop

refers to the fibre filament system. Both feeders are similar, however, a cutting tool is included in the reinforcement extruder to cut the fiber at specific length. The matrix material filament spool is fed to the extruder, which then pulls the filament from the spool into the tube towards the print head. Inside the printing head, the thermoplastic material such as nylon is heated to $265^{\circ}C$, which is above the melting temperature, making the nylon ready to be deposited. MT deposits only one type of material at a time, that is either matrix filament (nylon) or reinforcement, never both at the same time. Markforged® has published data sheets including the mechanical properties of various materials as presented in Tables 3.4 and 3.5. In the current study, only carbon fibers were utilized as reinforcement in the components fabrication.

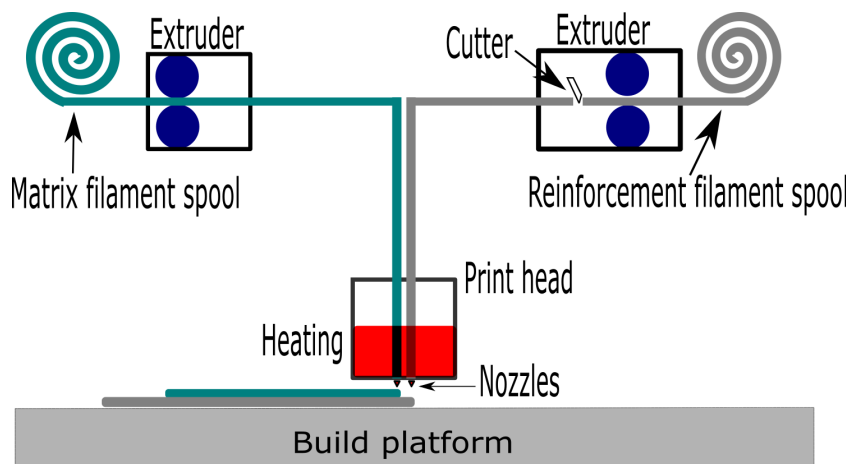


Figure 3.2: Schematic overview of the matrix and reinforcement feeding system of MT desktop printer

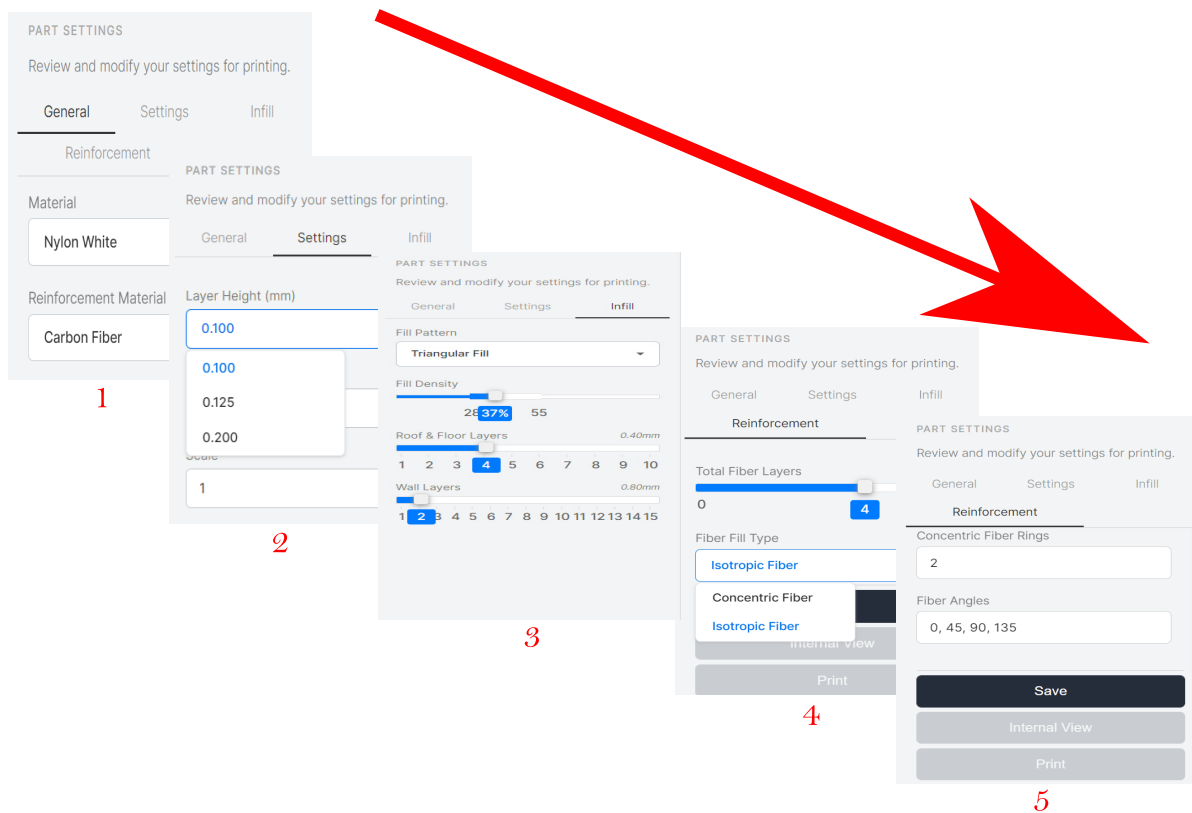


Figure 3.3: Graphical user interface of different options of Eiger software (GUI-Eiger)

MT printer has its own cloud based slicing software called “Eiger” for uploading the STere-oLithography (stl) file to the printer. Eiger software has a variety of parameters for altering the stl file, according to the users specifications, such as: infill pattern for matrix, printing pattern for reinforcement, infill density for both materials, layer thickness for reinforcement, number of walls, roofs, and bottoms. Figure 3.3 shows user interface of the standard group of parameters that can be changed based on each user demand. The parameters that are illustrated in Fig. 3.3 will be explained from left to right. After importing the .stl file, the first option (1) is to choose the matrix material (e.g. nylon, onyx) and reinforcement material (e.g. carbon fibers, glass fiber and so on). Second option (2) is allowing to choose thickness for each layer deposited for CF (0.1, 0.125, 0.2), instead matrix layer has a fixed thickness of 0.125 mm. Third sub-figure (3) refers to the infill pattern: the user is able to choose between triangular, rectangular, hexagonal as shown in Fig. 3.4 as well as gyroid and solid fill. The fourth option (4) is applicable only when reinforcement is added, and enables to choose fiber fill type as shown in Fig. 3.5. The last option (5) is to choose fiber angles for each layer and number of concentric fiber rings.

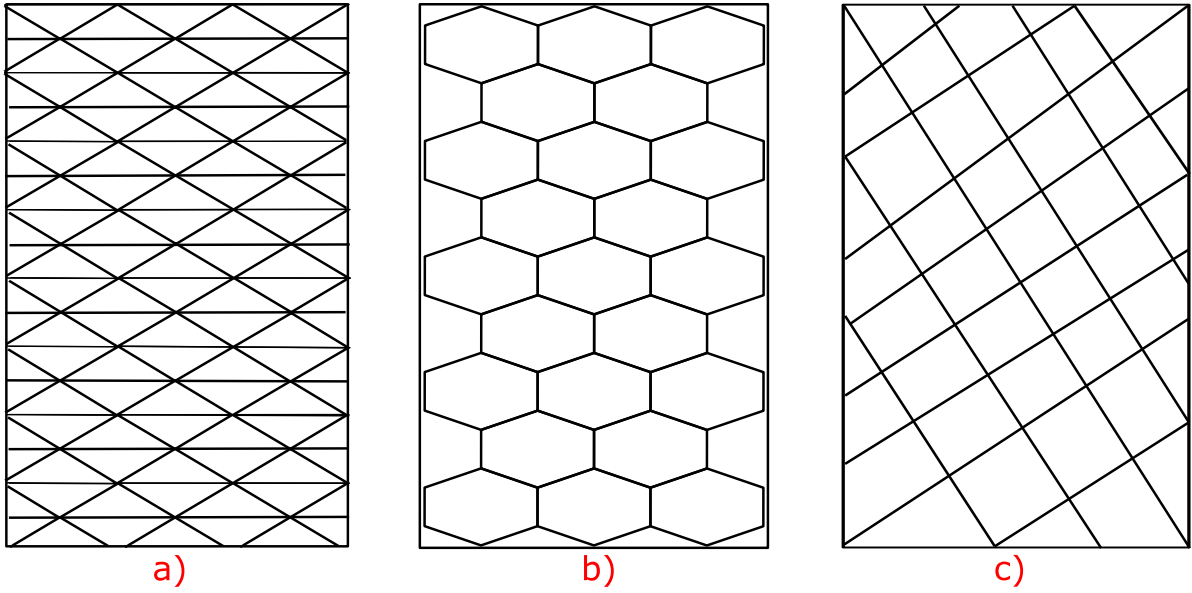


Figure 3.4: Top view of a slice of printed part with different infill patterns: a) Triangular, b) Hexagonal and c) ± 45 Rectangular

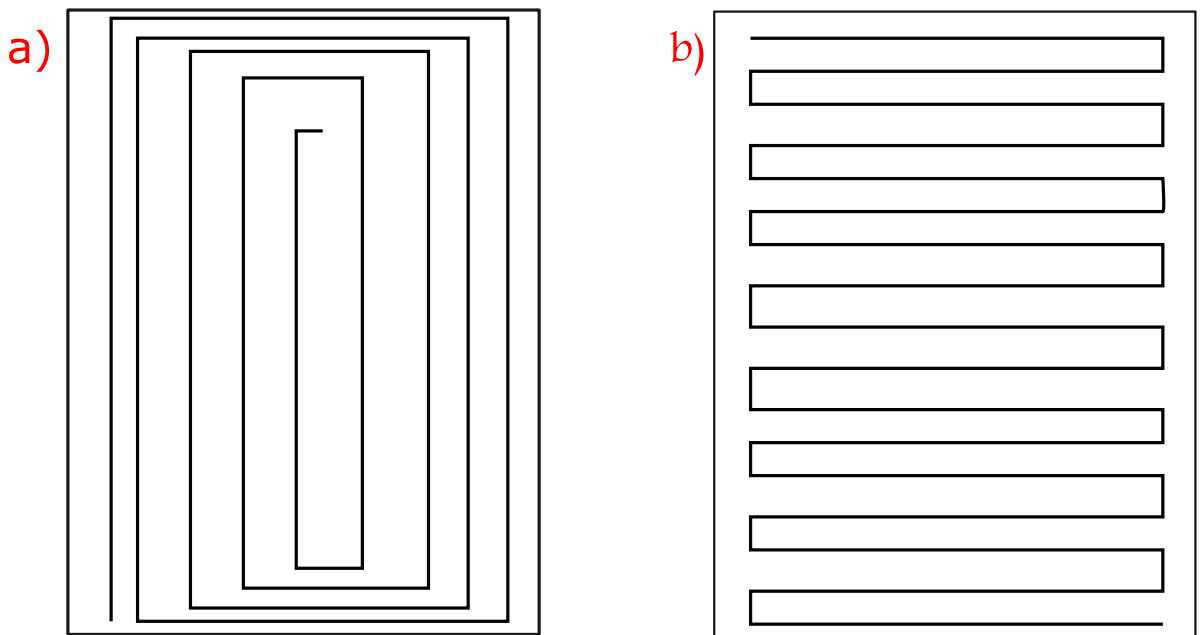


Figure 3.5: Top view of a slice of printed part with different infill patterns: a) Concentric, b) Isotropic

Table 3.1: Sample codes

Sample code	Printing pattern	Position of CF within the sample	# rings
S1	100% nylon	-	-
S2	C	6 th	1
S3	C	6 th	2
S4	C	6 th	3
S5	C	6 th	4
S6	C-I	6 th – 3 rd & 9 th	4-1&1
S7	C	3 rd & 9 th	2
S8	C	4 th – 8 th	2
S9	C	5 th & 7 th	2

3.2 Preliminary Experimental Study

3.2.1 Samples Manufacturing

As stated earlier, MT printer has been used to manufacture the samples for mechanical testing and also the straight beam flexures (SBF) used in Chapter 5 compliant mechanism application. Even though the printer parameters were generally stated earlier, the exact settings that were used will be stated here. Various amounts of carbon fiber on different layers was embedded in a white nylon matrix. This chapter investigates the influence of various filament amounts in a layer and of the positioning of the reinforced layers within the specimens on the tensile and flexure behaviors of the printed specimens. Figures 3.6a and 3.6b present the samples with geometrical features of a total length of 65mm for tensile tests (dog-bone shape) and 98mm for bending tests (rectangular shape), both specimens having the same width of 1.5mm and thickness of 1.375mm (namely 11 layers, hence 6-th layers considered to be the central layers). For the sake of brevity, only two samples are presented in Figs. 3.6c and 3.6d. Sample S2 configuration is shown in Fig. 3.6c, in which left dog bone refers to the whole printed sample, and right sub-figure refers only to one layer (6th layer) with one concentric ring of carbon fiber deposited. Whilst sample S6 configuration is presented in Fig. 3.6d, where right part illustrates the difference between layers with deposited isotropic and concentric ring fibers. Table 3.1 lists all samples with the codes used, in which, "C" refers to concentric ring, and "I" refers to isotropic with fibers oriented in the direction transversal to that of the tensile load.

The tensile test bench shown in Fig. 3.7a which consists of the specimen (1), frame (2),

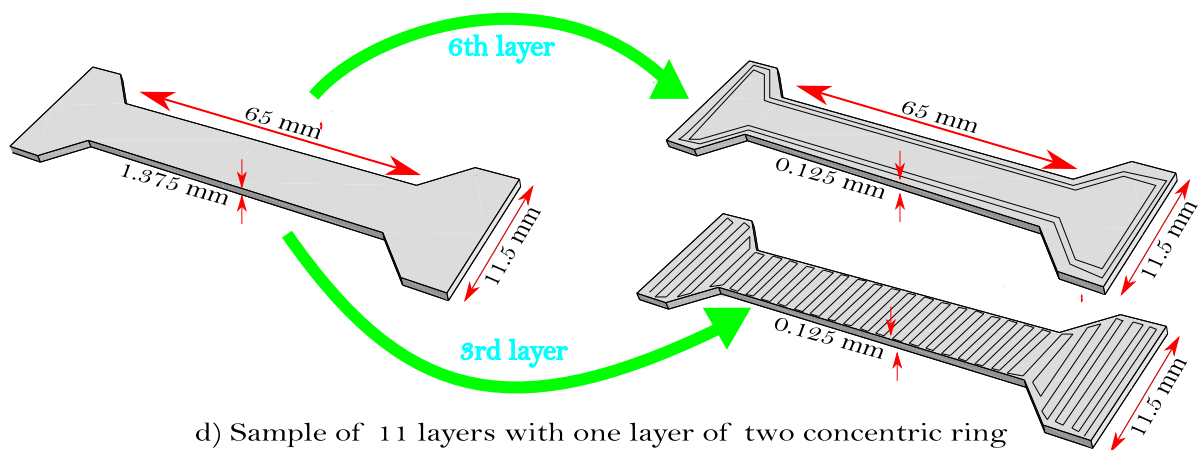
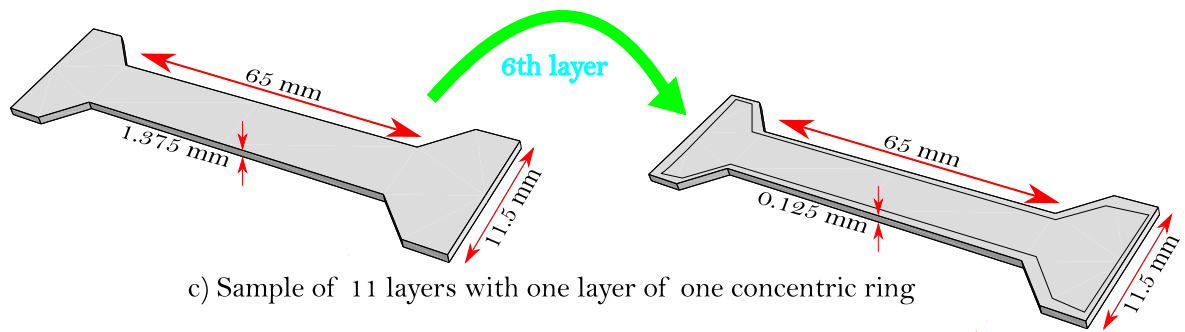
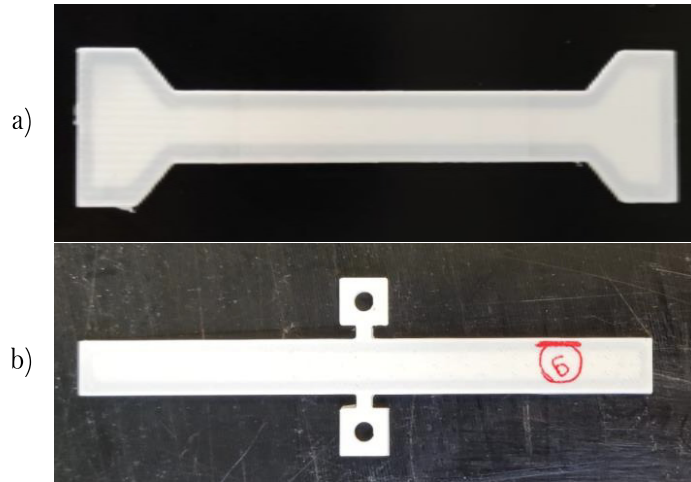


Figure 3.6: Example of tensile specimens configurations

a ball screw transmission powered by a brush-less servo motor to make an electro-cylinder (3), two clamps (4), a load cell (NS WL 1-500 kg) (5) that is an electro-cylinder made by a brush-less servo motor and an extensometer (6) which is mounted over the specimen. The procedure of the tensile test organized according to following steps:

1. The sample is connected to the two clamps, then the extensometer is mounted over the sample,
2. A preliminary traction force of 6N is applied to check for any misalignment with respect to the force direction, which is considered the sample homing position.
3. A constant velocity of 0.25 mm/s is applied until a strain rate of 0.7% is reached. Once the strain value of 0.7% is reached, the sample is brought back in the opposite direction to its homing position with the same velocity.
4. Step 3 is repeated four times.

The bending test bench is instead shown in Fig. 3.7b. It is composed by a specimen (1) whose ends are connected with two clamps (2) mounted with revolute pairs on two sliders (3), so as to enable specimen ends rotation and translation, an electro-cylinder connected to the mid of the specimen with a third clamp (4), a load cell (5) and a frame (6). Two encoders are used to measure the rotation of the clamps with respect to the respective slide, whereas two laser sensors are used to measure slider translation. The load cell is connected between the electro-cylinder and the third clamp. The procedure for the bending test was organized according to the following steps:

1. The sample was connected to the three clamps
2. A constant velocity of 2.5 mm/s is applied until the sample ends perform a rotation of 18°
3. Step 2 is repeated four times.

3.2.2 Experimental Results and Discussion

The tensile test results are arranged in two groups: samples (S2-S6) with CF embedded along the longitudinal direction only in the central layer (central plane) as well as nylon only sample as shown in Fig. 3.8a; and samples (S7-S9) for CF deposited far from the central layer as shown in Fig. 3.8b. Instead, the bending tests results (angular deflection vs bending moment) are illustrated in

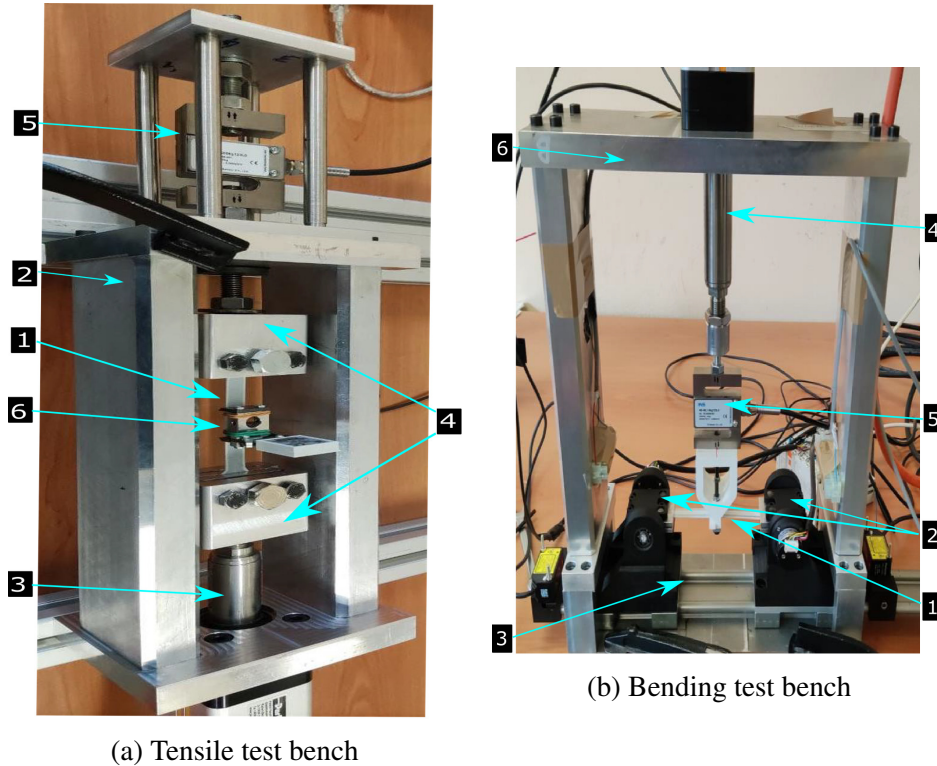
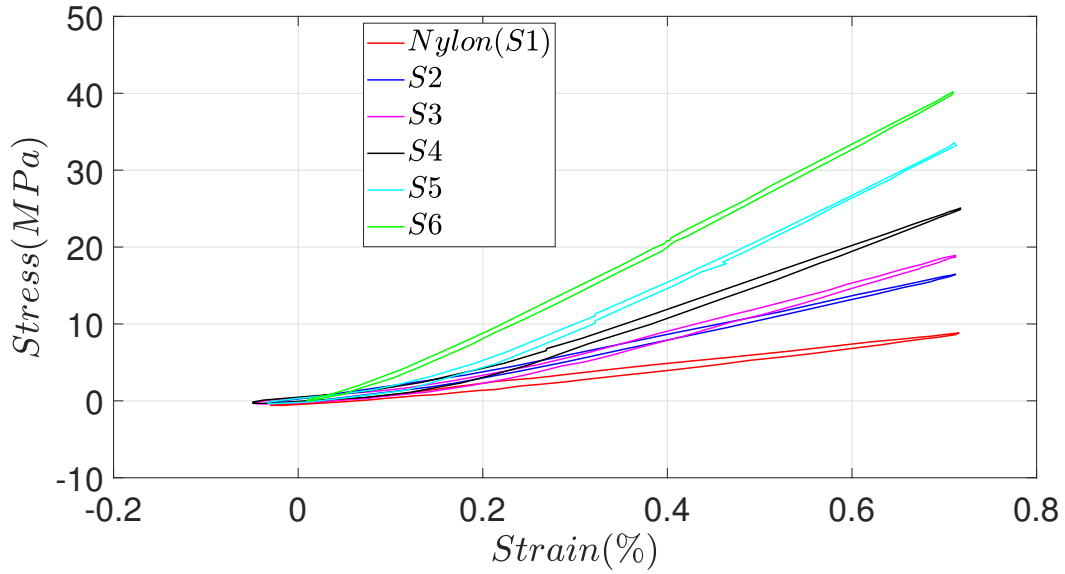


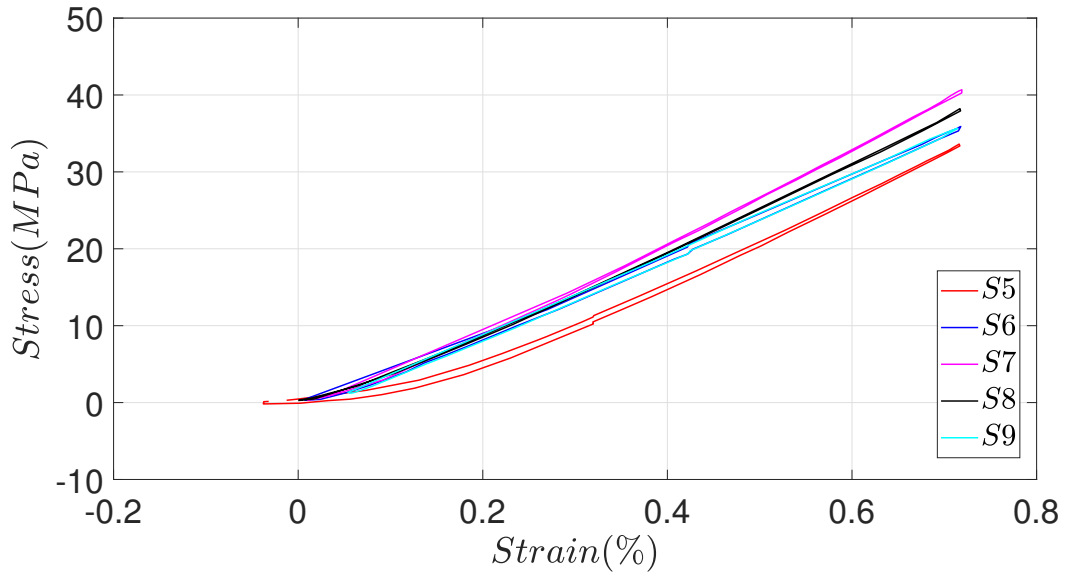
Figure 3.7: Mechanical test benches

Figs. 3.9a and 3.9b. It is shown that, by increasing the number of CF filament, the stress value raised at 0.7% strain. The maximum value of 40 MPa reached by sample 6 (S6), which means that the isotropic fiber in the transverse direction (90°) also contributes to increasing the tensile value. In contrast, the minimum value of 9 MPa is reached by S1 which has no fiber embedded as expected. All samples belonging to the second group show a similar behavior in which a maximum tensile stress of 39.1 MPa was obtained with a standard deviation of 3.67 MPa. From the bending test results, it can be seen that samples (S1-S5) show a similar trend, proving that the fiber filaments deposited on the central layer do not significantly affect the flexural stiffness. Also in this case, the highest value of the bending moment (65 Nmm) is reached by sample S6, meaning that isotropic fibers at 90° also contribute to increasing the flexural stiffness. The mean value of the maximum moment computed for samples (S1-S5) is 47.5 Nmm with a standard deviation of 10.2 Nmm. The lowest value is achieved by S1. Overall, the experimental results revealed the following:

1. When a uniaxial tension is applied, the position of longitudinal fiber (concentric printing pattern) within the sample does not have any influence on the tensile stiffness. On the contrary, number

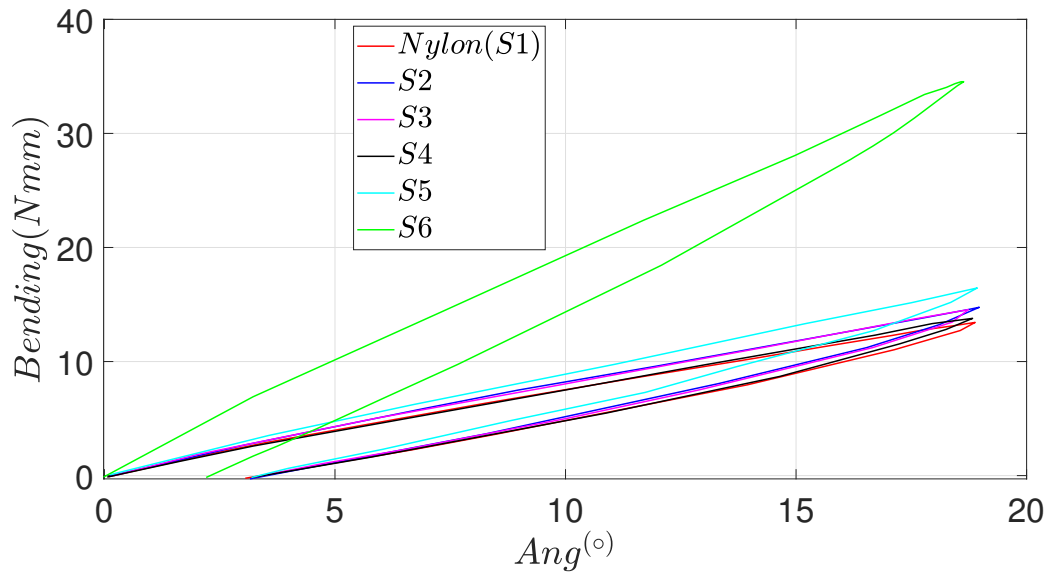


(a) CF deposited in the central plane (S2-S6)

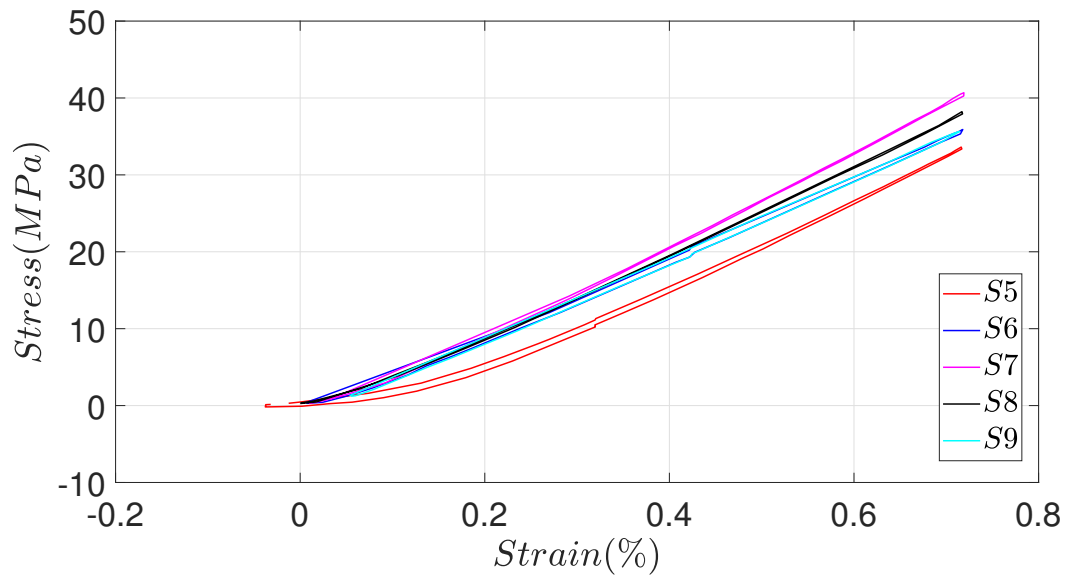


(b) CF deposited away from the central plane

Figure 3.8: Stress-strain curves



(a) CF deposited out of the central plane (S2-S6)



(b) CF deposited out of the central plane (S1-S6)

Figure 3.9: Bending test results

of fibers deposited have an effect on the tensile stiffness results as shown in samples 5, 7, 8 and 9. Whereby these samples have the same number of fibers but in different sample position (e.g. in S5, 6th layer have a 4 concentric ring, although, S9 having 2 rings in the 5th layer and other 2 in the 7th layer) with the same tensile results.

2. When a bending is applied, the flexural stiffness is not affected by the amount of longitudinal fibers added on the central layer, however, the concentric ring out of the central layer plays a key role as shown in S7.
3. Transversal fibers deposition such as S6 slightly rise both the tensile and flexural stiffness, however more experimental tests need to be carried out to fully understand the contribution of such printing pattern.

3.3 Analytical Models

3.3.1 Classical Laminate Theory (CLT)

MT printed parts are build up by stacking a number of layers, also called plies or laminas. Each ply can be of distinct materials, having different mechanical properties, thickness, and orientation which results in what is called or known as laminate. The mechanical properties of the laminate are determined by its stiffness matrix, which can be calculated from the properties of each ply including their material properties, thickness, and orientation (which is called their stacking sequence/ply book). A lot of theories have been developed including classical laminate theory (CLT), shear deformation beam theory (SDBT), state space approach (SSA) and so on. In this section only CLT is illustrated. CLT, like thin beam theories, is used for thin beams/plates with negligible shear deformation effect and rotary inertia. The behavior of the laminate is based on linear/classical laminate theory, which is presented in the following section and that could be used in a preliminary design stage. The following assumptions should be considered in analyzing MT printed laminated composite:

1. Each lamina has an orthotropic properties.
2. Each lamina is elastic.
3. Bond between layers is of zeros thickness, hence overall thickness of laminate is the summation of each laminae thickness.

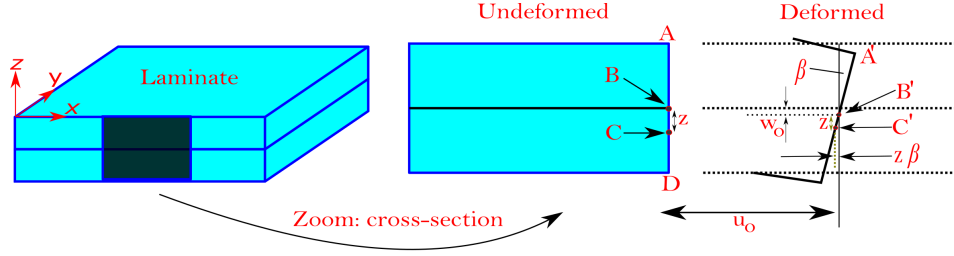


Figure 3.10: Laminate geometry of typical deformation in the x-z plane

4. Bond is completely rigid (no slip occurs between plies interfaces), which means no shear strain exists between layers ($\gamma_{yz} = \gamma_{zx} = 0$).
5. The laminate deforms according to the Kirchoff assumptions: 1) Normals to the midplane remain straight and normal to the deformed midplane after deformation; 2) Normals to the midplane do not change length.

By considering the laminate presented in Fig. 3.10. The middle surface is located central through the thickness of the laminate. Based on the above mentioned hypotheses, the origin of the laminate is at the mid-plane that is $z = 0$. After adding a load, three things occur: a) Line AD translates in the horizontal direction x axis, b) Line AD rotates around z axis and c) Point B' moves downwards along the thickness direction. Therefore, the displacements at every point through the thickness can be obtained as shown in Eq. 3.1.

$$\begin{aligned}
 u(x, y, z) &= u_o(x, y) - z \sin(\beta) = u_o(x, y) - z\beta \\
 v(x, y, z) &= v_o(x, y) - z \sin(\alpha) = v_o(x, y) - z\alpha \\
 w(x, y) &= w_o(x, y)
 \end{aligned} \tag{3.1}$$

where u and v are the displacements along the x and y , respectively at each point (x, y, z) directions and w refer to the displacement along the z at each point (x, y) directions as presented in Fig. 3.10. u_o , v_o and w_o are the displacement components for the midsurface at $z = 0$. As the $\varepsilon_{zz} = 0$, and noting that practical values of β and α are very small, the transverse deflection is the same for any point through the thickness of the printed laminate as below:

$$\begin{aligned}
 \beta &= \frac{\partial w}{\partial x} \\
 \alpha &= \frac{\partial w}{\partial y}
 \end{aligned} \tag{3.2}$$

Consequently, by substitution Eq. 3.2 in Eq. 3.1, the displacements u and v in the x and y - directions, respectively can be expressed as in Eq. 3.3

$$\begin{aligned} u(x, y, z) &= u_o(x, y) - z \frac{\partial w_o}{\partial x} \\ v(x, y, z) &= v_o(x, y) - z \frac{\partial w_o}{\partial y} \end{aligned} \quad (3.3)$$

For one ply the strain components in the global coordinate system (x, y, z) can be related to the strain in the mid-plane by using Eq. 3.1 as shown in the following Eq. 3.4 and in a matrix form in Eq. 3.5.

$$\begin{aligned} \varepsilon_x(x, y, z) &= \frac{\partial u}{\partial x} = \frac{\partial u_o}{\partial x} - z \frac{\partial^2 w_o}{\partial x^2} \\ \varepsilon_y(x, y, z) &= \frac{\partial v}{\partial y} = \frac{\partial v_o}{\partial y} - z \frac{\partial^2 w_o}{\partial y^2} \\ \gamma_{xy}(x, y, z) &= \frac{\partial u}{\partial y} + \frac{\partial v}{\partial x} = \frac{\partial u_o}{\partial y} + \frac{\partial v_o}{\partial x} - 2z \frac{\partial^2 w_o}{\partial x \partial y} \end{aligned} \quad (3.4)$$

$$\begin{Bmatrix} \varepsilon_x \\ \varepsilon_y \\ \gamma_{xy} \end{Bmatrix} = \begin{Bmatrix} \frac{\partial u_o}{\partial x} \\ \frac{\partial v_o}{\partial y} \\ \frac{\partial u_o}{\partial y} + \frac{\partial v_o}{\partial x} \end{Bmatrix} + z \begin{Bmatrix} -\frac{\partial^2 w_o}{\partial x^2} \\ -\frac{\partial^2 w_o}{\partial y^2} \\ -2\frac{\partial^2 w_o}{\partial x \partial y} \end{Bmatrix} \quad (3.5)$$

The terms γ_{yz} and γ_{xz} are constant through the thickness because of assumption no. 2 (each lamina is elastic). The first three values of Eq. 3.4 can be rewritten as presented below:

$$\begin{Bmatrix} \varepsilon_x^o \\ \varepsilon_y^o \\ \gamma_{xy}^o \end{Bmatrix} = \begin{Bmatrix} \frac{\partial u_o}{\partial x} \\ \frac{\partial v_o}{\partial y} \\ \frac{\partial u_o}{\partial y} + \frac{\partial v_o}{\partial x} \end{Bmatrix} \quad (3.6)$$

In which, ε_x^o , ε_y^o and γ_{xy}^o represent the tension and shearing of the laminate that is called ‘‘mid-surface strains’’. Moreover, the curvatures of the laminate due to bending and twisting can be expressed below:

$$\begin{Bmatrix} k_x \\ k_y \\ k_{xy} \end{Bmatrix} = \begin{Bmatrix} -\frac{\partial^2 w_o}{\partial x^2} \\ -\frac{\partial^2 w_o}{\partial y^2} \\ -2\frac{\partial^2 w_o}{\partial x \partial y} \end{Bmatrix} \quad (3.7)$$

Hence, by substitutions in Eqs. 3.6 and 3.7, the laminate strains can be written as illustrated in the following formulation:

$$\begin{Bmatrix} \varepsilon_x \\ \varepsilon_y \\ \gamma_{xy} \end{Bmatrix} = \begin{Bmatrix} \varepsilon_x^o \\ \varepsilon_y^o \\ \gamma_{xy}^o \end{Bmatrix} + z \begin{Bmatrix} k_x \\ k_y \\ k_{xy} \end{Bmatrix} \quad (3.8)$$

Heretofore, the strains at every point (x, y, z) in the laminate is replaced in terms of the mid-plane strains ε_x^o , ε_y^o and γ_{xy}^o and the three curvatures k_x , k_y and k_{xy} by using Eq. 3.8. The main aim is to write all the functions (displacements, stresses, and strains) in terms of only two variables (x and y) to simplify the analysis. Consequently, it is better to also replace the stress components at every-point (x, y, z) of the laminate in terms of functions of only two variables (x, y) . To do this, the stresses are integrated over the thickness of the laminate to obtain the resultant forces and moments per unit length as: (see Eqs. 3.9 and 3.10)

$$\begin{bmatrix} N_x \\ N_y \\ N_{xy} \end{bmatrix} = \int_{-h/2}^{h/2} \begin{bmatrix} \sigma_x \\ \sigma_y \\ \tau_{xy} \end{bmatrix} dz \quad (3.9)$$

$$\begin{bmatrix} M_x \\ M_y \\ M_{xy} \end{bmatrix} = \int_{-h/2}^{h/2} \begin{bmatrix} \sigma_x \\ \sigma_y \\ \tau_{xy} \end{bmatrix} z dz \quad (3.10)$$

in which N_x , N_y , and N_{xy} are the tensile and shear forces per unit length with units [N/m]. M_x , M_y , and M_{xy} are the moments per unit length with units [N]. The integration in Eq. 3.9 over several laminae. Hence, the integrals can be divided into summations of integrals over each ply as shown in Eqs. 3.11 and 3.12

$$\begin{bmatrix} N_x \\ N_y \\ N_{xy} \end{bmatrix} = \sum_{k=1}^n \int_{h_{k-1}}^{h_k} \begin{bmatrix} \sigma_x \\ \sigma_y \\ \tau_{xy} \end{bmatrix} dz \quad (3.11)$$

$$\begin{bmatrix} M_x \\ M_y \\ M_{xy} \end{bmatrix} = * \sum_{k=1}^n \int_{h_{k-1}}^{h_k} \begin{bmatrix} \sigma_x \\ \sigma_y \\ \tau_{xy} \end{bmatrix} z dz \quad (3.12)$$

where k is the lamina number counting from the bottom to the top, N is the number of laminae in the laminate, and h_k is the coordinate of the top surface of the k_{th} lamina.

Therefore, the resultant forces and moments can be rewritten in terms of mid-plane strains and curvatures as below:

$$[N] = \sum_{k=1}^n \int_{h_{k-1}}^{h_k} \left[[\bar{Q}]_k \varepsilon^o dz + \sum_{k=1}^n \int_{h_{k-1}}^{h_k} [\bar{Q}]_k k^o z dz \right] \quad (3.13)$$

$$[M] = \sum_{k=1}^n \int_{h_{k-1}}^{h_k} \left[[\bar{Q}]_k \varepsilon^o dz + \sum_{k=1}^n \int_{h_{k-1}}^{h_k} [\bar{Q}]_k k^o z^2 dz \right] \quad (3.14)$$

$$\begin{aligned} A_{ij} &= \sum_{k=1}^n [[\bar{Q}_{ij}]_k (h_k - h_{k-1})] \\ B_{ij} &= \frac{1}{2} \sum_{k=1}^n [[\bar{Q}_{ij}]_k (h_k^2 - h_{k-1}^2)] \\ D_{ij} &= \frac{1}{3} \sum_{k=1}^n [[\bar{Q}_{ij}]_k (h_k^3 - h_{k-1}^3)] \\ H_{ij} &= \frac{5}{4} \sum_{k=1}^n \left[[\bar{Q}_{ij}]_k t_k - \frac{4}{t^2} (t_k \bar{h}_k^2 + \frac{t_k^2}{12}) \right] \end{aligned} \quad (3.15)$$

where A_{ij} , B_{ij} , D_{ij} and H_{ij} are the extensional stiffness, the bending-extension coupling stiffness, the bending stiffness, and the transverse shear stiffness, respectively. The disadvantage of the above mentioned equations is: coupling are not included, and to overcome this limitation, A_{11} , B_{11} and D_{11} can be replaced by a new values of equivalent stiffness parameters that include couplings. Once the [A], [B], [D], and [H] matrices have been formulated, then both strains and curvatures at the middle surface can be obtained by using (Eq. 3.16) for a given set of stress resultants. This means that the

*Cross-section width is included for a composite beam

strains can be computed at any point through the thickness of the laminate using Eq. 3.8.

$$\begin{bmatrix} N_x \\ N_y \\ N_{xy} \\ M_x \\ M_y \\ M_{xy} \end{bmatrix} = \begin{bmatrix} A_{11} & A_{12} & A_{16} & B_{11} & B_{12} & B_{16} \\ A_{12} & A_{22} & A_{26} & B_{12} & B_{22} & B_{26} \\ A_{16} & A_{26} & A_{66} & B_{16} & B_{26} & B_{66} \\ B_{11} & B_{12} & B_{16} & D_{11} & D_{12} & D_{16} \\ B_{12} & B_{22} & B_{26} & D_{12} & D_{22} & D_{26} \\ B_{16} & B_{26} & B_{66} & D_{16} & D_{26} & D_{66} \end{bmatrix} \begin{bmatrix} \varepsilon_x^o \\ \varepsilon_y^o \\ \gamma_{xy}^o \\ k_x \\ k_y \\ k_{xy} \end{bmatrix} \quad (3.16)$$

In which the stresses can be computed on each lamina using the constitutive equations of that particular lamina as in the following equations:

$$[\sigma]_k = [\bar{Q}]_k \varepsilon \quad (3.17)$$

where \bar{Q} refers to the reduced transformed stiffness matrix of each ply (see Eq.3.36 for transformation)

$$[\sigma]_k = [\bar{Q}]_k \varepsilon^o + z[\bar{Q}]_k k^o \quad (3.18)$$

A set of equivalent moduli E_x , E_y , G_{xy} , v_{xy} of the MT laminated components, can be obtained by the following equations:

$$\begin{aligned} E_x &= \frac{A_{11}A_{22} - A_{12}^2}{tA_{22}} \\ E_y &= \frac{A_{11}A_{22} - A_{12}^2}{tA_{11}} \\ G_{xy} &= \frac{A_{66}}{t} \\ v_{xy} &= \frac{A_{12}}{A_{22}} \end{aligned} \quad (3.19)$$

The laminate moduli mentioned in Eq. 3.19 are valid only for in-plane loads and they can not be utilized to predict bending response. The bending moduli can be computed by neglecting the terms D_{16} and

D_{26} as presented below:

$$\begin{aligned}
E_x^b &= \frac{12(D_{11}D_{22} - D_{12}^2)}{t^3 D_{22}} \\
E_y^b &= \frac{12(D_{11}D_{22} - D_{12}^2)}{t^3 D_{11}} \\
G_{xy}^b &= \frac{12(D_{66})}{t^3} \\
v_{xy}^b &= \frac{D_{12}}{D_{22}}
\end{aligned} \tag{3.20}$$

where the superscript b refers to bending moduli. If $D_{16} = D_{26} = 0$ in the laminate, it means that the laminate bending moduli will only approximate the true response. A dimensionless measure of how close a laminate is to an equivalent orthotropic material is given by how small the coefficients A_{16} , A_{26} , D_{16} , and D_{26} are for in plane loads as in Eq. 3.21 and bending loads in Eq. 3.22:

$$r_N = \sqrt{\left(\frac{A_{16}}{A_{11}}\right)^2 + \left(\frac{A_{26}}{A_{22}}\right)^2} \tag{3.21}$$

$$r_M = \sqrt{\left(\frac{D_{16}}{A_{11}}\right)^2 + \left(\frac{D_{26}}{D_{22}}\right)^2} \tag{3.22}$$

When there is no symmetry, the dimensionless measure is provided by the coefficients in the B matrix as below:

$$r_B = \frac{3}{(A_{11} + A_{22} + A_{66}t)} \sum_i \sum_j (B_{ij}^2) \tag{3.23}$$

All the above mentioned dimensionless ratios are used to assess the quality of the approximation obtained using equivalent moduli. By achieving more close results to zero, the more accurate the corresponding laminate moduli will be.

3.3.1.1 Preliminary Design of MT Beam

The deflection of a printed FDM/MT laminated beam includes two components that are bending and shear as below:

$$\delta = \delta_b + \delta_s \tag{3.24}$$

where the main contribution in bending deflection δ_b is the bending stiffness (EI) and the shear deflection δ_s is shear stiffness (GA). Opposed to metallic beams, shear deformations can not be ignored for

laminated composite beams because the shear modulus of composite is low (about $E/10$ or less). The significance of the shear deflection δ_s with respect to the bending deflection δ_b varies with the span, the larger the span the lesser the effect of shear. The values of the bending (EI) and shear stiffness (GA) can be computed using the analysis in the next paragraph.

To compute both EI and GA of a structure that consists of one segment or several segments (e.g. I-beam, etc), the next steps should be considered. First, compliance matrix should be obtained as shown below by inverting Eq. 3.16:

$$\begin{bmatrix} \varepsilon_x^o \\ \varepsilon_y^o \\ \gamma_{xy}^o \\ k_x \\ k_y \\ k_{xy} \end{bmatrix} = \begin{bmatrix} \alpha_{11} & \alpha_{12} & \alpha_{16} & \beta_{11} & \beta_{12} & \beta_{16} \\ \alpha_{12} & \alpha_{22} & \alpha_{26} & \beta_{12} & \beta_{22} & \beta_{26} \\ \alpha_{16} & \alpha_{26} & \alpha_{66} & \beta_{16} & \beta_{26} & \beta_{66} \\ \beta_{11} & \beta_{12} & \beta_{16} & \delta_{11} & \delta_{12} & \delta_{16} \\ \beta_{12} & \beta_{22} & \beta_{26} & \delta_{12} & \delta_{22} & \delta_{26} \\ \beta_{16} & \beta_{26} & \beta_{66} & \delta_{16} & \delta_{26} & \delta_{66} \end{bmatrix} \begin{bmatrix} N_x \\ N_y \\ N_{xy} \\ M_x \\ M_y \\ M_{xy} \end{bmatrix} \quad (3.25)$$

Second, based on beam theory assumptions, $N_s = 0$, $M_s = 0$, and assuming no-coupling between normal and shearing effects ($\alpha_{16} \approx 0$, $\beta_{16} \approx 0$, $\delta_{16} \approx 0$), then the compliance equations shown in Eq. 3.25 can be reduced to the following:

$$\begin{Bmatrix} \varepsilon_x^i \\ k_x^i \\ \gamma_{xs}^i \\ k_{xs}^i \end{Bmatrix} = \begin{bmatrix} \alpha_{11} & \beta_{11} & 0 & 0 \\ \beta_{11} & \delta_{11} & 0 & 0 \\ 0 & 0 & \alpha_{66} & \beta_{66} \\ 0 & 0 & \beta_{66} & \delta_{66} \end{bmatrix} \begin{bmatrix} N_x^i \\ M_x^i \\ N_{xs}^i \\ M_{xs}^i \end{bmatrix} \quad (3.26)$$

where ε_x^i and γ_{xs}^i are the mid-plane strains, and k_{xs}^i is the curvature. N_x^i , N_s^i , N_{xs}^i are the normal and shear forces per unit length along the boundary of the beam, instead M_x^i , M_s^i , and M_{xs}^i refer to the moments per unit length on the sides with units [N]. The superscript i indicates the segment number and also to differentiate the beam quantities. The printed laminate can be unsymmetrical as a result of especially orthotropic laminae (isotropic, unidirectional) that are not symmetrically arranged with respect to the middle surface. Under these conditions $\alpha_{16} = \beta_{16} = 0$ and δ_{16} decreases rapidly in magnitude with increasing number of laminae. In addition, Eq. 3.27 can be used to solve the general

problem of bending and torsion.

$$\begin{Bmatrix} N_x^i \\ M_x^i \\ N_{xs}^i \\ M_{xs}^i \end{Bmatrix} = \begin{bmatrix} A_i & B_i & 0 & 0 \\ B_i & D_i & 0 & 0 \\ 0 & 0 & F_i & C_i \\ 0 & 0 & C_i & H_i \end{bmatrix} \begin{Bmatrix} \varepsilon_x^i \\ k_x^i \\ \gamma_{xs}^i \\ k_{xs}^i \end{Bmatrix} \quad (3.27)$$

in which A_i represents to the axial stiffness per unit length; B_i is the coupling between bending curvature and extensional force per unit length; D_i is the bending stiffness M_x^i ; F_i refers to the in-plane shear stiffness under shear N_{xs}^i ; H_i is the twisting stiffness under twisting moment M_{xs}^i and C_i is the coupling between the twisting curvature K_{xs}^s . The neutral axis of bending can be obtained by using the following formula:

$$e_b = \frac{B}{A} \quad (3.28)$$

The bending stiffness passing through the neutral axis of bending which is the product of the elastic modulus times the moments of inertia I_{ss} , I_{rr} , and I_{sr} of classical beam theory, is replaced by the mechanical properties of each segment defined as:

$$\begin{aligned} EI_s &= \bar{D}_i b_i \\ EI_r &= \frac{A_i b_i^3}{12} \end{aligned} \quad (3.29)$$

Shear stiffness of the cross section can be computed as:

$$GA = \frac{b}{h_{44}} \quad (3.30)$$

Based on the above mentioned formulations, it can be noted that the analysis of deformations of MT printed laminated composites can be easily performed using available computer programs at very low computational cost (see Eq. 3.15). Additionally, MT beam deflection can be obtained easily by calculating the beam section properties as illustrated in 3.27. In the next Section 3.3.3, previous experimental results will be compared to the CLT formulations to check the accuracy of the method.

3.3.2 Volume Averaging Stiffness Method (VAS)

It is an analytical model based on a volume averaging stiffness method (VAS) which is utilized to predict the effective elastic moduli of the MT printed composite parts with varying printing pattern, and number of reinforcement layers. The model classifies MT printed components into various regions including: a) solid regions within the part, in which matrix material is printed (e.g. $\pm 45^\circ$ from the longitudinal axis), alternating layer by layer; b) wall regions, in which matrix material border is printed around the perimeter of the part layer by layer and in parallel to the longitudinal axis; c) reinforcement (e.g. CF) regions, in which CF is printed in either a concentric, isotropic or mixed pattern (concentric rings with isotropic layers). Since the width of fibers strand in a layer plus the width of both walls is less than the overall width of the part, Eiger software places a small amount of matrix on either side of CF to fill in the gaps that is referred to as infill matrix region. The model allows each section's properties to be accounted for in order to predict the effective elastic moduli of the whole part as shown in Eqs. 3.31 and 3.32. Measurements of the various dimensions needed for those equations, are obtained from Eiger software or/and experimentally.

$$V_t = L \times W \times T \quad (3.31)$$

where V_t is the total volume of the printed specimen. L , W and T are the active length, width and total thickness, respectively of the part.

$$V_m = N_{ml} \times T_{ml} \times L \quad (3.32a)$$

$$V_{r_c} = (W_{rs} \times N_{cr} \times 2)N_{rl} \times T_{rl} \times L \quad (3.32b)$$

$$V_{r_i} = (W_{rs} \times N_s)N_r \times T_{rl} \times L \quad (3.32c)$$

$$V_{r_{inf}} = (W - W_w - W_{rs} \times N_s)N_{rl} \times T_{rl} \times L \quad (3.32d)$$

in which, V_m is the volume of the matrix within the sample. N_{ml} and N_{rl} refer to number of matrix and reinforcement layers, respectively within the printed part. For embedding/printing fiber within the sample, two distinct patterns are available such as, concentric and isotropic. That are described by V_{r_c} and V_{r_i} , respectively. The volume of the fiber is calculated based on the pattern used. Thus for concentric printing pattern Eq. 3.32b is used, where W_{fs} is the width of each fiber strand embedded that is $\sim .4mm$ (obtained from previous work); N_{cr} is the number of concentric ring embedded and

T_{fl} represents the thickness of each fiber layer. Whereas, for isotropic printing pattern Eq. 3.32c is utilized, in which, N_s (see Eq. 3.33) and N_{fl} are referred to number of isotropic strands embedded per layer and total fiber layers, respectively. As mentioned earlier, all the printed parts include a wall region which is considered when calculating volume of infill in fiber region (W_w is the width of wall).

$$N_s = \frac{W}{0.78} - W_w \times N_w \quad (3.33)$$

In Eq. 3.33, N_w refers to number of wall being printed within the sample. Thus, number of strand can be obtained as a function of printed part width and diameter of strand which was obtained earlier as $0.78mm$.

Mathematical homogenization theory is employed to alter the constitutive characteristics of a heterogeneous composite material to a homogeneous material with effective properties that yield in average/corresponding macroscopic response. A material with aligned prismatic voids and characteristic length linked to cross-section of the void is considered. The effective material properties void density is derived via a mixture model in which each point in the continuum is associated with a tensorial meso-structure variable named as void density (ρ). Consequently based on the investigations and comparison to the experimental results developed later (ρ), is assumed to be 5% and 90% for solid and infill regions respectively. Moreover, the compliance matrix [S] for each region of the composite can be presented as the shown in Eq. 3.34.

$$[S] = \begin{bmatrix} \frac{1}{E_1} & -\frac{v_{21}}{E_2} & -\frac{v_{31}}{E_3} & 0 & 0 & 0 \\ -\frac{v_{12}}{E_2} & \frac{1}{E_2} & -\frac{v_{32}}{E_3} & 0 & 0 & 0 \\ -\frac{v_{13}}{E_1} & -\frac{v_{23}}{E_2} & \frac{1}{E_3} & 0 & 0 & 0 \\ 0 & 0 & 0 & \frac{1}{G_{23}} & 0 & 0 \\ 0 & 0 & 0 & 0 & \frac{1}{G_{13}} & 0 \\ 0 & 0 & 0 & 0 & 0 & \frac{1}{G_{12}} \end{bmatrix} \quad (3.34)$$

Eqs. 3.35 are used to populate the S matrix. S matrix for the solid region and fiber (in case of isotropic pattern not printed in the fiber direction) must be transformed with a rotation matrix as shown in Eqs. 3.36 and 3.37. In Eq. 3.35, E_1 , G_{12} and v_{12} refers to the matrix modulus of elasticity, shear modulus and Poisson's ratio in the longitudinal direction, whereas E_2 and G_{23} and v_{32} in the transverse direction.

$$\begin{aligned}
E_1 &= (1 - \rho_1)E_m \\
E_3 &= E_2 = (1 - \rho_1^{1/2})E_m \\
G_{13} &= G_{12} = G_m \frac{(1 - \rho_1)(1 - \rho_1^{1/2})}{(1 - \rho_1)(1 - \rho_1^{1/2})} \\
G_{23} &= G_m = (1 - \rho_1^{1/2}) \\
v_{13} &= v_{12} = v_m(1 - \rho_1) \\
v_{32} &= v_{31} = v_{23} = v_{21} = v_m(1 - \rho_1^{1/2})
\end{aligned} \tag{3.35}$$

After the S matrices have been computed and rotated, they are multiplied by their corresponding volume fractions, and summed to create the global matrix as developed in Eq. 3.38. Finally, the mechanical properties elastic moduli of the printed composite are found as shown in Eq. 3.40.

$$[T] = \begin{bmatrix} \cos(\theta)^2 & s(\theta)^2 & 0 & 0 & 0 & 2\cos(\theta)\sin(\theta) \\ \sin(\theta)^2 & \cos(\theta)^2 & 0 & 0 & 0 & -2\cos(\theta)\sin(\theta) \\ 0 & 0 & 1 & 0 & 0 & 0 \\ 0 & 0 & 0 & \cos(\theta) & \sin(\theta) & 0 \\ 0 & 0 & 0 & -\sin(\theta) & -\cos(\theta) & 0 \\ -\cos(\theta)\sin(\theta) & \cos(\theta)\sin(\theta) & 0 & 0 & 0 & \cos(\theta)^2 - \sin(\theta)^2 \end{bmatrix} \tag{3.36}$$

$$[\hat{S}_G] = [T]' \times [S]' \times [T] \tag{3.37}$$

In Eq. 3.36 T represents the transformation matrix around z coordinate and \hat{S} is the transformed compliance matrix after rotation between global printed laminate composite and material coordinate system.

$$S_G = V_{fr} \times \hat{S}_r(\theta) + V_{f(m)} \times \hat{S}_r(\theta) + V_{f(infr)} \times \hat{S}_{infr}(\theta) \tag{3.38}$$

where V_{fr} and $V_{f(m)}$ are the volume fractions of the reinforcement and matrix, respectively within the specimen. Instead $V_{f(infr)}$ indicate the volume fraction of the infill inside the reinforcement region. The volume fractions are obtained by Eq. 3.39. It is worth to note that Eq. 3.38 can be modified based

the contribution of each region.

$$\begin{aligned}
 V_{fr} &= \frac{V_f}{V_t} \\
 V_{f(m)} &= \frac{V_m}{V_t} \\
 V_{f(infr)} &= \frac{V_{rinf}}{V_t}
 \end{aligned} \tag{3.39}$$

$$\begin{aligned}
 E_{xx_p} &= \frac{1}{S_{G_{11}}} \\
 E_{yy_p} &= \frac{1}{S_{G_{22}}} \\
 G_{xy_p} &= \frac{1}{S_{G_{66}}} \\
 \nu_{xy_p} &= \frac{-S_{G_{12}}}{S_{G_{11}}}
 \end{aligned} \tag{3.40}$$

In Eq. 3.40, E_{xx_p} and E_{yy_p} are the elastic moduli in the longitudinal and transverse direction of the MT laminated printed composite. Whereas, G_{xy_p} and ν_{xy_p} are the shear modulus and Poisson's ratio in the reinforcement direction (Index p refers to printed laminate).

3.3.3 Analytical Models Verification

To verify the above mentioned analytical models, six different printed composite specimens are introduced as presented in Table 3.2. Samples NR100 and NR50 were printed in accordance with ASTM D638-14 namely of $165mm$, $19mm$ width and $3.2mm$ thickness. While, NCD0 sample has a length of $250mm$, a width of $15mm$ and a thickness of $1mm$. NCD90 sample has a length of $175mm$, width of $25mm$ and thickness of $2mm$. NCMO and NGMO have an active length of $170mm$, a width of $25mm$ wide and a thickness of $2.5mm$ with different LSS for each sample. The cross-section profile of NCD0, NCD90, NCMO and NGMO usually consists of: floor layers, front fiber layers, mid-layers, back fiber layers and ceiling layers. Each section has specific material properties with specific orientation along the longitudinal axis. Most of the matrix layers consist of closed layers of nylon or onyx and alternate orientation between ± 45 from the longitudinal axis. Whereas, fiber layers consist of Kevlar/glass or carbon fiber filament and alternated orientation between $0/\pm 45/90$ from the longitudinal axis. For the sake of brevity, not all the samples are presented in figures; however Fig. 3.11

Table 3.2: Samples part settings used for comparison between experimental and proposed analytical models

Part Settings	NR100	NR50	NCD0	NCD90	NCMO	NGMO
Layer height of (M) (mm)	0.2	0.2	0.2	0.2	0.15	0.114
Layer height of (R)	-	-	0.125	0.125	0.1	0.085
Infill pattern	R	R	T	T	R	R
Printing pattern	-	-	I	I	C	I
Fill Density	100% nylon	50% nylon	100% nylon	100% nylon	100% nylon	100% nylon
LSS- Composition (M)	100	50	61.4	58.7	$[[-45, 45]_{2n}, [C]_{5f}, [-45, 45]_n, [45, -45]_{2n}]_T$	$[[-45, 45]_{2n}, [90/0]_{3g}, [90/0]_{3g}, [45, -45]_{2n}]_T$
Composition (R)	-	-	38.6	41.3		

shows the NCMO arrangement in the left sub-figure with the top view of one layer with 12 concentric ring of CF embedded on the right figure.

In Table 3.2, layer thickness for each layer is defined, where M and R are referred to matrix and reinforcement, respectively used in each case. Moreover, infill pattern and percentage are described that is "R" for rectangular, "T" for triangular, "C" for concentric and "I" for isotropic. The type of material used in each case is described in LSS, in which "n" index refers to nylon, "c" for carbon fiber and "g" for glass fiber.

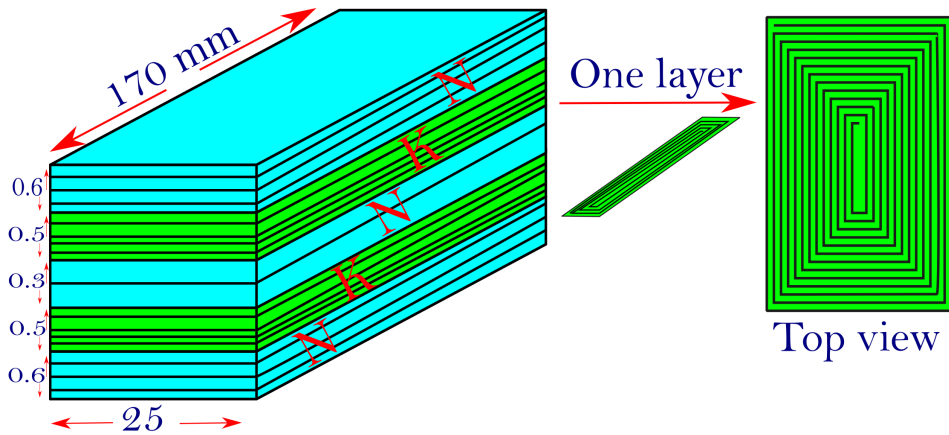


Figure 3.11: Example of tensile specimens configurations

The formulations of the VAS mentioned in Section 3.3.2 was coded in a python script to predict the elastic moduli and Poisson's ratio of the tested specimens. The formulations of CLT was coded in a MatLab script in a dynamic way. Table 3.3 shows a comparison of elastic modulus E and Poisson's ratio obtained from CLT, VAS models and experimental results obtained by previous work done in MUL2 group at the Politecnico di Torino and previous work in [99].

Table 3.3: Comparison of measured and predicted elastic moduli and Poisson's ratio

Sample	Properties	EXP	VAS	CLT	$Error_{VAS}$	$Error_{CLT}$
NR100	E_{xx_p}	898.23	893	–	0.5%	–
NR50	E_{xx_p}	538	482.22	–	10.36%	–
NCD0	E_{xx_p}	21250	21000	–	1.176%	–
NCD90	E_{yy_p}	1510	1403.2	–	7.0728%	–
NCMO	E_{xx_p}	37000	35651	34229	3.645%	7.48918%
	ν_{xy_p}	0.3	0.30521	0.30117	1.73%	0.39%
NGMO	E_{xx_p}	6400	6467.2	6667	1.05%	4.17%
	ν_{xy_p}	0.067	0.21605	0.077123	222.462%	15.10%

It is shown that elastic modulus (E_{xx}) for NR100 is found to be predicted in high accuracy with a difference of 0.5%. However, the error is raised by decreasing the amount of nylon deposited as obtained in sample NR50 (error 10.36%). For sample NCD0 the error was 1.176%, however when the fiber was placed in the transverse direction, the error is increased to 7.0728% as in sample NCD90. Even though this thesis deals only with MT components, however a wider comparison to account all the printing parameters is included by using also MarkOne printer. In addition, NCMO specimen is found to be predicted in high accuracy with a difference of 3.645% and 1.73% for E and Poisson's ratio, respectively. On the other hand, CLT prediction is found with higher error of 4.17% and 7.48918%, respectively for NGMO, NCMO samples. Elastic moduli of NGMO specimen are found with better accuracy of 1.05% with VAS method.

It can be noted that, from the analytically modelled behaviour of a carbon coupon (with 0° fibre arrangement), only the axial stiffness of the fibre will contribute to the overall stiffness behaviour of the modelled coupon. However, tested Carbon coupons are influenced by lateral stiffness due to the embedded printing process for the coupon, which inherently provides lateral stiffness even though the fibres are axially oriented. This can explain the noticeable under-prediction (7.5%) found for carbon coupon specimens.

In a previous study done by Melenka et al. [100] on printed kevlar composite sample, it was noted that accuracy is improved by increasing the amount of fiber embedded. A 0.1% accuracy was reported for specimens with 10% volume fraction. In this study, although the specimens were printed with 40% volume fraction, the prediction accuracy is found to be high. The difference in the accuracy can be clarified due to the fibre arrangements including the fibre placement path (orientation)

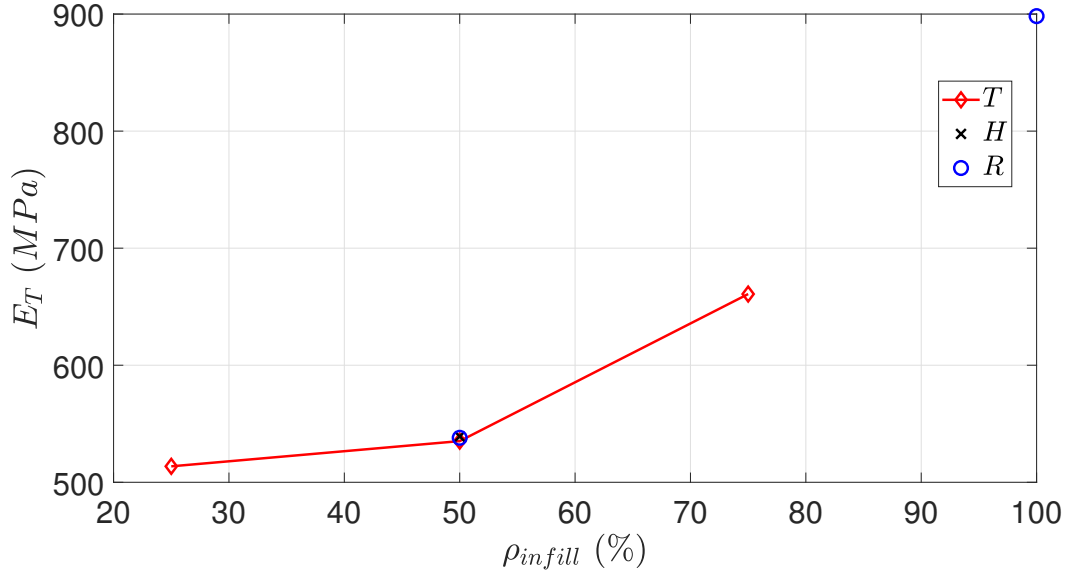


Figure 3.12: E_T with various infill density and pattern

that plays an important role in determining the failure mechanism, and hence has an affect on the accuracy level between analytically estimated and experimentally measured elastic properties. Such finding was related to the poor bonding between the fibres and the Nylon matrix which is not reflected by the analytical model, as a perfect bond between fibres and matrix is a usual analysis restriction inherent in the micromechanical analysis of composite materials [101].

As with MT printers there is the ability to take advantages of the experimental and analytical work, using Eq. 3.41 the modulus of elasticity of honeycomb and fiber can be calculated as

$$\begin{aligned}
 E_h &= \frac{E_T - E_N \times \%V_N}{\%V_h} \\
 E_f &= \frac{E_T - E_N \times \%V_N}{\%V_f}
 \end{aligned}
 \tag{3.41}$$

where, E_h and E_f are the moduli of elasticity of honeycomb and fiber, E_T refers to the Young's modulus of the total printed part and E_N is the nylon Young's modulus. Figure 3.12 presents E_T results as a function of various infill density and pattern. It can be noted that, the variable printing pattern has no difference on the elastic modulus obtained.

3.4 Conclusion

The preliminary experimental investigation on the effect of fiber amount, and their location within the FDM-MT printed sample was carried out with the major aim to investigate the possibility of using FDM-MT structures as flexible elements in compliant mechanism. Moreover, two analytical models including CLT and VAS models have been developed in order to predict the response of printed specimens and their results have been compared to experimental data so as to understand their applicability and accuracy on MT 3D printed structures, as well as to study the impact of various infill density and pattern on the structural behavior of MT 3D printed parts. The results have shown that CLT and VAS models are valid models for predicting elastic moduli and Poisson's ratio despite their simplicity and easy way to calculate the properties. Therefore, based on the observations reported and discussed in this chapter, the following conclusions could be drawn:

1. By increasing the number of filaments within the sample, the stress value raised at strain rate of 0.7%.
2. Carbon fiber filaments embedded on the central layer do not significantly affect the flexural stiffness
3. Isotropic fiber in the transverse direction contribute to increasing both tensile and flexural stiffness.
4. The fibre reinforcement orientation and volume were found to affect the accuracy of the analytical models.
5. VAS model provides more accurate results compared to CLT as it accounts the number of concentric rings, or/and number of fiber strand in each layer. In CLT, such parameters cannot be defined. Further, VAS becomes more accurate by introducing Eq. 3.33 for varying the number of fiber strand depending on the width of the specimen.
6. The void density in the matrix region should be defined as 5% in the VAS model. However, more work should be conducted at a micro-scale level to understand the behavior accurately.
7. Various printing patterns have no effect on the strength of the MT printed specimen, however triangular infill pattern increases the speed while still making a strong part.

However, both analytical models have disadvantages in the prediction of the Young's modulus which will be discussed later in Chapter 4.

Table 3.4: Mechanical properties of the matrix materials obtained by Markforged under ASTM D638

Property	Nylon	Onyx
Tensile modulus [MPa]	940	1400
Tensile stress at break [MPa]	54	30
Tensile strain at break [%]	260	58
Tensile stress at yield [MPa]	31	36
Tensile strain at yield [%]	27	25
Flexural modulus [MPa]	840	2900
Flexural strength at break [MPa]	32	81

Table 3.5: Mechanical properties of the reinforcement materials obtained by Markforged under ASTM D638

Property	Carbon fiber	Aramid	Glass fiber	HSHT glass
Tensile modulus [MPa]	54000	27000	21000	21000
Tensile stress at break [MPa]	700	610	590	600
Tensile strain at break [%]	1.5	2.7	3.8	3.9
Compressive strength [MPa]	320	97	140	192
Compressive modulus [MPa]	54000	28000	21000	21000
Compressive strain at break [%]	0.7	1.5	NA	NA
Flexural modulus [MPa]	51	26	22	21
Flexural strength [MPa]	470	190	210	420
Flexural strain at break [%]	1.2	2.1	1.1	2.2

Chapter 4

Numerical Approach

Three dimensional (3D) MarkTwo[®] (MT) composite structures are built via laying up of different layers that are bonded together and hence will be more capable of carrying loads [102]. Each lamina can be composed of fibers embedded in a matrix. These fibers are placed according to a specific needs that confers high mechanical properties in the longitudinal direction of the fibers, whereas the matrix has the role of holding them together. Modeling of MT composite parts varies from modeling traditional structure. In which, the printed components (e.g. MT parts) show sophisticated behavior on their cross section included different components, for instance, infill component, floor, roof and wall region in each layer having different geometrical and material properties based on infill density. In addition, there is still a gap in obtaining the material properties used (e.g. elastic modulus) as it is usually unknown and sensitive to such specific parameters used (e.g. infill density), making the numerical simulation is elusive and inaccurate. Consequently, in order to achieve accurate numerical analysis/modeling of MT components and in response of the need of a comprehensive numerical assessment of various theories within the Carrera Unified Formulation (CUF) framework. This chapter provides a detailed insight into special modeling techniques for MT parts including a novel preprocessing platform within the CUF which easily describe the modeling parameters and discretization in an accurate and time efficient way that accounts all the details of the MT printed components. The chapter begins with illustration of background and motivation of numerical approach implemented for general laminates as in Section 4.1. The CUF structural formulation is presented in Section 4.2, then analysis of various MT printed parts is carried out and compared with analytical results to verify the capability of proposed platform. Section 4.8 mentions the conclusion and future recommendations.

4.1 Numerical Background and Motivation

The use of composite materials has been increased in various industries including aerospace, automotive, nuclear and biomedical fields. This mainly is due to their high strength, stiffness and lightness. However, the behavior of composite structures is determined by a broader range of parameters

compared to conventional structures and hence study of their mechanics becomes elusive. Moreover, new and important problems arise including delamination and a reliable structure model is needed to predict accurately distribution of normal and transverse shear stress [103]. MT produces composite structures in a form of laminates by laying up layers by layer. The classical beam model developed by Euler and Bernoulli [103, 104] provides inaccurate results when dealing with thick deep laminated beam, since shear effects are neglected as mentioned earlier in Section 3.3.1. Timoshenko [105, 106] suggested his well-known theory in which constant distribution of shear deformation is assumed with the aim of overcoming the limitations mentioned earlier. The main disadvantage of this theory is the need of using shear correction factor which is a problem dependent. Therefore, classical and first shear deformation theories are considered to be inadequate to analyze laminated composite beams, and thus, more higher order models should be conceived [103]. Reddy [107] introduced a plate theory which gives a parabolic distribution of the transverse shear strains making sure that the transverse shear stresses are null on the top and bottom surfaces. By utilizing such model, exact closed form solutions for static, buckling and dynamic analyses of cross ply laminated beams with arbitrary boundary conditions were introduced in Khdeir et al. [108, 109] and Khdeir [110].

On the other hand, Surana and Nguyen [111] used Lagrange's polynomials by presenting two-dimensional curved beam element to obtain various higher-order theories. So, the hierarchical property of the expressions makes it possible for the displacement expansion in the transverse direction to be of arbitrary polynomial order p , thereby permitting strains of at least order $(p-1)$. In addition, Matsunaga [112] have presented a theory whereupon the displacement components can be expanded into power series of the thickness coordinate (z). Additionally, axial stresses were calculated through the constitutive relations, however, the transverse shear stresses were computed by integration of the three dimensional equilibrium equations. On the other side, Rao et al. [113] computed the free vibrations of laminated beams by adopting a mixed theory via using a Taylor's series expansion.

All the above mentioned theories are based on the equivalent single layer (ESL) in which discontinuity distribution of shear stresses triggered by continuity of shear strains at interface that represents the main restriction of this models. Consequently, many researchers have developed a new theory called layer wise approach to overcome this limitation. For example, Shimpi and Ghugal [114] propose a new layer-wise trigonometric model for two-layered cross-ply beams. The main characteristic is that the shear stresses are derived directly from the constitutive equations that fulfill both the condition of continuity of shear stresses at the interface and at free condition at the free surfaces. This model illustrates

that number of layers related to the number of unknowns. On the same topic, Tahani [115] presented two theories for analyzing the static and dynamic behavior of the laminated beams. In the first case, a layer-wise plate theory was adapted to beams, whereas the second model was obtained via following a simple procedure similar to the one used in the development of plate and shell theories. Unfortunately, by increasing the number of layers, the layer wise becomes unfavorable since it is too expensive in terms of computational cost. To overcome this problem, many researchers have adopted layer independent theories in which zig-zag or Heaviside's functions are extensively utilized. Murakami [116] considered to be the first to develop and use a zig-zag function into Reissner's new mixed variational principle to develop a plate theory (for a complete review of Murakami's zig-zag method, see [117]). Vidal and Polit [118, 119] presented a refined sine model by providing a Heaviside function for each layer to satisfy the continuity conditions for both displacements and transverse shear stress and the free conditions of the upper and lower surfaces. Subsequently, the same authors introduced Murakami's zig-zag function in the sine model (Ref. [120]) so as to take into account the discontinuity of the first derivative of the displacements. A further example is can found in (Ref. [121]), where a new linear two-nodes beam element is evaluated based on the combination of classical Timoshenko theory and the refined zig-zag kinematics proposed by [122].

It is noted that various trials have been conducted to present a general and reliable theory to capture every aspect of composite structure. In this chapter, a variety of higher-order theories are tested for studying the static behavior of MT laminated beams. These theories provides a procedure to obtain refined structural models derived from Carrera's Unified Formulation (CUF), which offers a procedure to obtain refined structural models. Therefore, the order and types of theories as free input parameters can be considered. CUF was first developed for plate and shell models. For example, in Carrera [123], It is presented an extensive definition of possible approaches to plate and shell laminated structures and introduced the Unified Formulation and to acquire distinct models based on displacements and transverse stress assumptions. Lately, CUF has been extended to the beam model. Carrera and Giunta [124] have studied/studied/investigated the higher-order theories capabilities via using N-order Taylor type (TE) expansions of the section coordinates to introduce the displacement variables. The study was performed on beams with rectangular and I-shaped cross-sections and the governing differentials equations were solved via the Navier type closed-form solution. In contrary, In Carrera et al. [125] unknown displacements were expanded by using N-order Lagrange polynomials (LE) which were defined on a set of sampling points belonging to the section. Carrera et al. [125] expanded the unknown

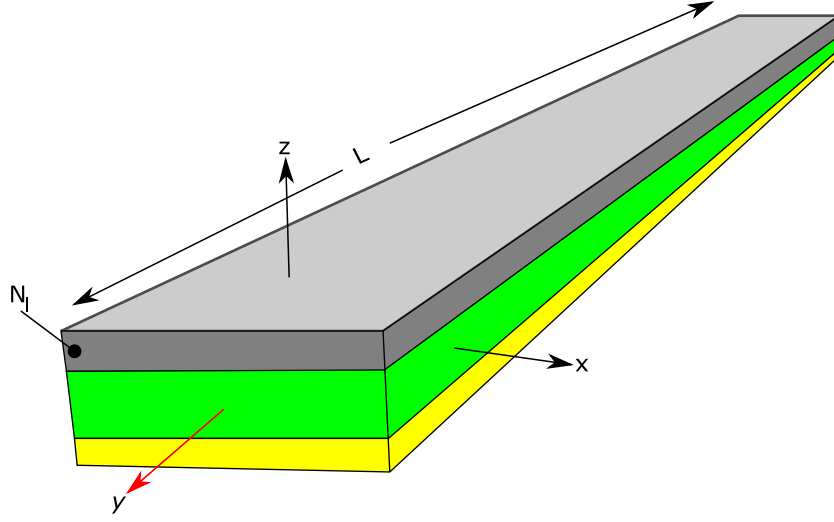


Figure 4.1: MT Laminated beam and its related Cartesian coordinate system

displacements via using N-order Lagrange polynomials (LE) which were defined on a set of sampling points belonging to the section. Instead, in Carrera and Giunta [124] investigated the higher-order theories capabilities via adopting N-order Taylor type (TE) expansions of the section coordinates to introduce the displacement variables. The study was performed on beams with rectangular and I-shaped cross-sections and the governing differential equations were solved via the Navier type closed-form solution.

4.2 Structural Formulation

4.2.1 Preliminary Considerations

Consider a generic MT laminated beam structure with N_l layered of length L as depicted in Fig. 4.1. A Cartesian coordinate frame is used, in which x and z are the cross-section coordinates and y is orthogonal and places along the beam axis (in red). The vector includes the 3D displacement components of a given point in the structural domain is expressed as:

$$\mathbf{u}(x, y, z) = \left\{ u_x \quad u_y \quad u_z \right\}^T \quad (4.1)$$

Subsequently, the stress ($\boldsymbol{\sigma}$) and strain ($\boldsymbol{\epsilon}$) states can be written in the following vectorial form:

$$\begin{aligned}\boldsymbol{\sigma} &= \left\{ \sigma_{xx} \quad \sigma_{yy} \quad \sigma_{zz} \quad \sigma_{xz} \quad \sigma_{yz} \quad \sigma_{xy} \right\}^T \\ \boldsymbol{\epsilon} &= \left\{ \epsilon_{xx} \quad \epsilon_{yy} \quad \epsilon_{zz} \quad \epsilon_{xz} \quad \epsilon_{yz} \quad \epsilon_{xy} \right\}^T\end{aligned}\quad (4.2)$$

In respect of the constitutive relations, each layer is assumed to be of linear elastic material, so the Hooke law can be applied at layer level as the following:

$$\boldsymbol{\sigma} = \tilde{\mathbf{C}}\boldsymbol{\epsilon} \quad (4.3)$$

where $\tilde{\mathbf{C}}$ refers to the material matrix as defined below:

$$\tilde{\mathbf{C}} = \begin{pmatrix} \tilde{C}_{11} & \tilde{C}_{12} & \tilde{C}_{13} & 0 & 0 & \tilde{C}_{16} \\ & \tilde{C}_{22} & \tilde{C}_{23} & 0 & 0 & \tilde{C}_{26} \\ & & \tilde{C}_{33} & 0 & 0 & \tilde{C}_{36} \\ & & & \tilde{C}_{44} & \tilde{C}_{45} & 0 \\ & & & & \tilde{C}_{55} & 0 \\ \text{sym.} & & & & & \tilde{C}_{66} \end{pmatrix} \quad (4.4)$$

The material coefficients \tilde{C}_{ij} described the functions of the elastic moduli along both the longitudinal and the transverse directions of the fiber, the shear moduli, the Poisson ratios, and the fiber orientation angle. Regarding the geometrical relations, the Green–Lagrange nonlinear strain components are included [126]. Consequently, the displacement–strain relations are expressed as below:

$$\boldsymbol{\epsilon} = \boldsymbol{\epsilon}_l + \boldsymbol{\epsilon}_{nl} = (\mathbf{b}_l + \mathbf{b}_{nl})\mathbf{u} \quad (4.5)$$

where \mathbf{b}_l and \mathbf{b}_{nl} refers to the linear and nonlinear differential operators, respectively [126]. These operators are defined below.

$$\mathbf{b}_l = \begin{bmatrix} 0 & \partial_y & 0 \\ \partial_x & 0 & 0 \\ 0 & 0 & \partial_z \\ \partial_z & 0 & \partial_x \\ 0 & \partial_z & \partial_y \\ \partial_y & \partial_x & \partial_0 \end{bmatrix}, \quad \mathbf{b}_{nl} = \begin{bmatrix} \frac{1}{2}(\partial_y)^2 & \frac{1}{2}(\partial_y)^2 & \frac{1}{2}(\partial_y)^2 \\ \frac{1}{2}(\partial_x)^2 & \frac{1}{2}(\partial_x)^2 & \frac{1}{2}(\partial_x)^2 \\ \frac{1}{2}(\partial_z)^2 & \frac{1}{2}(\partial_z)^2 & \frac{1}{2}(\partial_z)^2 \\ \partial_x\partial_z & \partial_x\partial_z & \partial_x\partial_z \\ \partial_y\partial_z & \partial_y\partial_z & \partial_y\partial_z \\ \partial_x\partial_y & \partial_x\partial_y & \partial_x\partial_y \end{bmatrix} \quad (4.6)$$

in which $\partial_x = \frac{\partial(\cdot)}{\partial x}$, $\partial_y = \frac{\partial(\cdot)}{\partial y}$, and $\partial_z = \frac{\partial(\cdot)}{\partial z}$. It is worth to note that parameters P_{ij} give the capability of tuning the kinematics assumptions, for more see Ref. [126, 127]

4.2.2 Carrera Unified Formulation

According to the current structural model based on the CUF framework, the displacement field \mathbf{u} can be represented as the product of two elements: one along the beam axis and one over the cross-section. For example, in one-dimensional model, the beam contribution is referred to the beam axis y and the other contribution is a function of x and z . The displacement field becomes as shown in Eq. 4.7 :

$$\mathbf{u}(x, y, z) = F_\tau(x, z)\mathbf{u}_\tau(y), \quad \tau = 1, 2, \dots, N \quad (4.7)$$

in which, \mathbf{u}_τ is the displacement vector, and F_τ represents the function expansion applied to approximate the behavior of the beam cross-section. N is the number of the expansion terms. Several choices are available for the expansion functions, in which for instance, Taylor polynomials [124, 126], Lagrange expansion [128], Legendre polynomials [129], and Chebyshev polynomials [126, 130] can be used. The generalized displacements \mathbf{u}_τ can be defined as functions of the unknown nodal displacement vector, $\mathbf{q}_{\tau i}$ and the one dimensional shape functions N_i is illustrated below :

$$u_\tau(y) = N_i \mathbf{q}_{\tau i}, \quad i = 1, 2, \dots, k \quad (4.8)$$

Among the others, in this work both Lagrange and Taylor polynomials are adopted to discretize the displacement field over the cross-section and they allow the employment of the Layer-wise (LW) and Equivalent Single Layer (ESL) approaches, respectively.

4.2.2.1 Layer Wise

The use of the Lagrange polynomials allows any cross-sectional geometry to be considered and an accurate description of the physical domain to be achieved. In this way, we have an accurate description of the physical surface of the problem. The degree of the interpolation is given by the number of the Lagrange points (LPs) used for discretization; for instance, a 4 points LE (L4) provides a linear interpolation, a 9 points LE (L9) ensures a quadratic interpolation and a 16 point LE (L16) gives a cubic interpolation as shown in Fig. 4.2

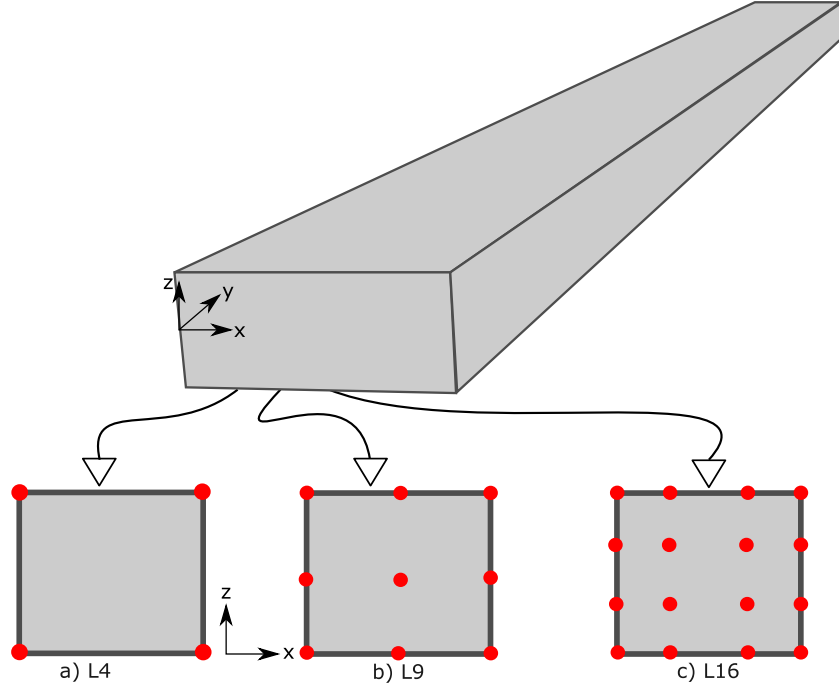


Figure 4.2: Example of typical solid MT cross-section discretized by; a) Four, b) Nine, c) sixteen Lagrange points

A comprehensive review about LW theories can be found in [131]. This approach treats each layer individually and both displacement and transverse shear stress continuity may be satisfied between each layer; as a result, it can yield results consistent with 3D elasticity solutions. In this thesis only nine points (L9) cubic is used and their interpolation functions are given by:

$$\begin{aligned}
 F_{\tau} &= \frac{1}{4}(r^2 + rr_{\tau})(s^2 + ss_{\tau}), & \tau &= 1, 3, 5, 7 \\
 F_{\tau} &= \frac{1}{2}s_{\tau}^2(s^2 + ss_{\tau})(1 - r) + \frac{1}{2}r_{\tau}^2(r^2 + rr_{\tau})(1 - s^2), & \tau &= 2, 4, 6, 8 \\
 F_{\tau} &= (1 - r^2)(1 - s^2), & \tau &= 9
 \end{aligned} \tag{4.9}$$

Where r and s can be from -1 and $+1$. Therefore, based on different elements, the cross-section displacement fields can be represented after substituting in 4.7. For example, the complete displacement field of one single L9 element is as follows:

$$\begin{aligned}
 u_x &= F_1u_{x1} + F_2u_{x2} + F_3u_{x3} + F_4u_{x4}\dots + F_9u_{x9} \\
 u_y &= F_1u_{y1} + F_2u_{y2} + F_3u_{y3} + F_4u_{y4}\dots + F_9u_{y9} \\
 u_z &= F_1u_{z1} + F_2u_{z2} + F_3u_{z3} + F_4u_{z4}\dots + F_9u_{z9}
 \end{aligned} \tag{4.10}$$

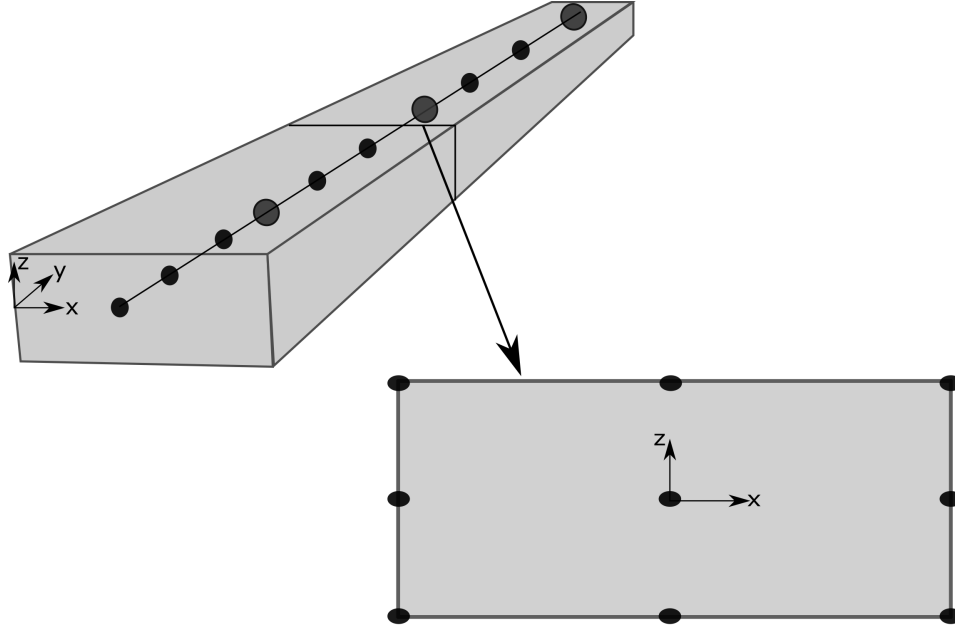


Figure 4.3: Representation of the finite element (FE) and Lagrange expansion (LE) theories employed over the macroscale structure of MT printed laminated solid beam

Table 4.1: Details of Taylor expansion

Order	T	F_τ	Second-order (TE2)
0	1	$F_1 = 1$	$u_x = u_{x_1} + xu_{x_2} + zu_{x_3} + x^2u_{x_4} + xzu_{x_5} + z^2u_{x_6}$
1	3	$F_2 = xF_3 = z$	$u_y = u_{y_1} + xu_{y_2} + zu_{y_3} + x^2u_{y_4} + xzu_{y_5} + z^2u_{y_6}$
2	6	$F_4 = x^2F_5 = xzF_6 = z^2$	$u_x = u_{x_1} + xu_{x_2} + zu_{x_3} + x^2u_{x_4} + xzu_{x_5} + z^2u_{x_6}$
3	10	$F_7 = x^3F_8 = xz^2F_9 = xz^2F_{10} = z^3$	
\vdots	T	F_τ	
N	$(N+1)(N+2)/2$	$F_{(N+1)(N+2)/2} = x^N F_{(N+1)(N+2)/2} = z^N$	

where $u_{x_1}(y), \dots, u_{z_9}(y)$ are the unknown variables of the problem and refer to the transitional displacement components of each of the nine points of the L9 element. The above displacement variables are the only unknowns, which their position are not on the beam element axis. For the sake of brevity F_τ is not fully explained here, but for more details readers can refer to [132]. A graphical representation of the spatial discretisation of the macroscale structure is shown in Fig. 4.3. Instead, ESL approach allows the treatment of the multi-layered MT structure as a one single-layered, through an appropriate homogenization of the cross-section properties [133]. The description of Taylor expansion (TE) and displacement fields is reported in Table 4.1: whereon x_A, y_A and z_A refer to the coordinates of a generic point “A” of coordinates (x, y, z) . The number of the Degrees Of Freedom (DOFs) is equal to the displacement and derivatives of the TE and, for example in case of TE2, they are 18.

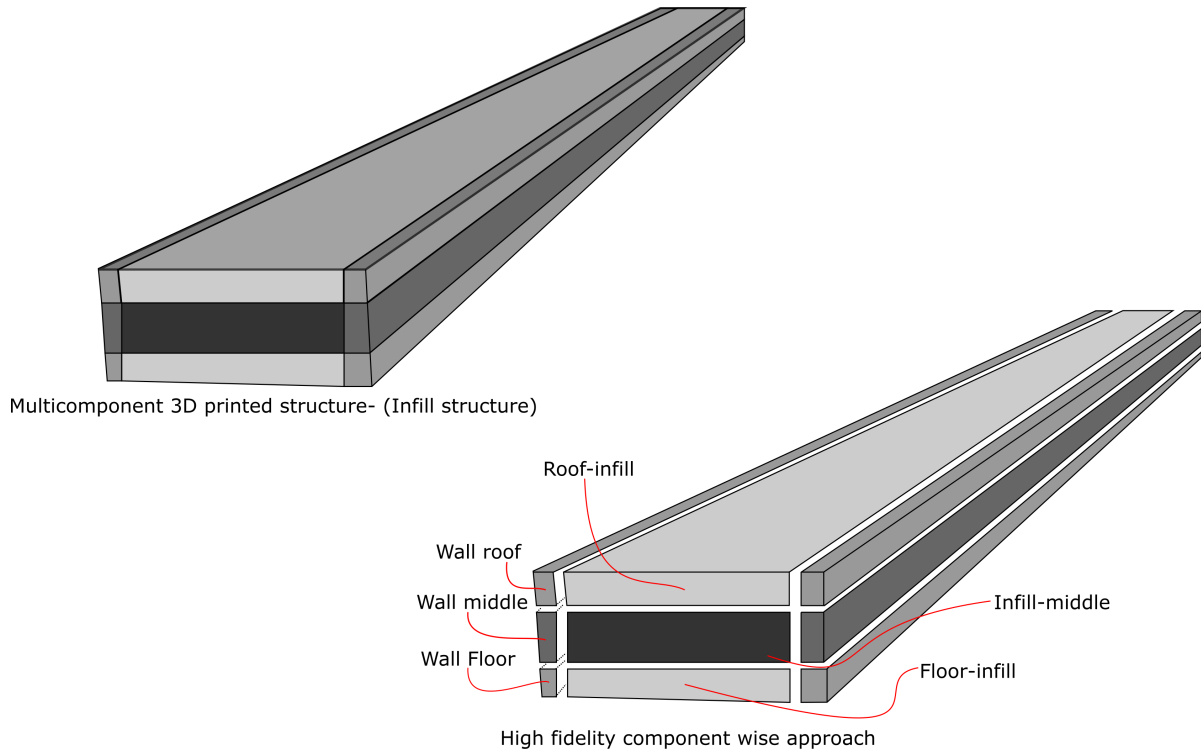


Figure 4.4: Component-wise approach

4.2.3 High Fidelity Modeling of 3D Printed Structure

Since most of FDM structures, i.e. MT printed specimens are composed of different components/regions, such as, infill, wall, floor, and roof region. These components/regions usually have various materials and geometrical behavior as depicted in Fig. 4.4. In a MT printed structure, for instance, infill region can be of different material properties that cannot be added along with the same element of wall or floor/roof components. An efficient FE modelling of the multicomponent 3D printed structures (MC3DPS) often requires considering of each component separately with different elements – beams – to build sufficiently accurate models with a reasonable number of DOFs.

The advanced capabilities of CUF 1D beam models mentioned earlier can be used to model the MC3DPS. LE formulation was presented to implement component wise (CW) model to divide the MT cross section into various sub domains, for instance, floor and roof and, infill as shown in Fig. 4.5. In order to solve the one-dimensional problem, the Finite Element model is used. The shape functions N_i are introduced to approximate the displacement over the beam axis (y). The vector \mathbf{u} can be written as in Eq. 4.11

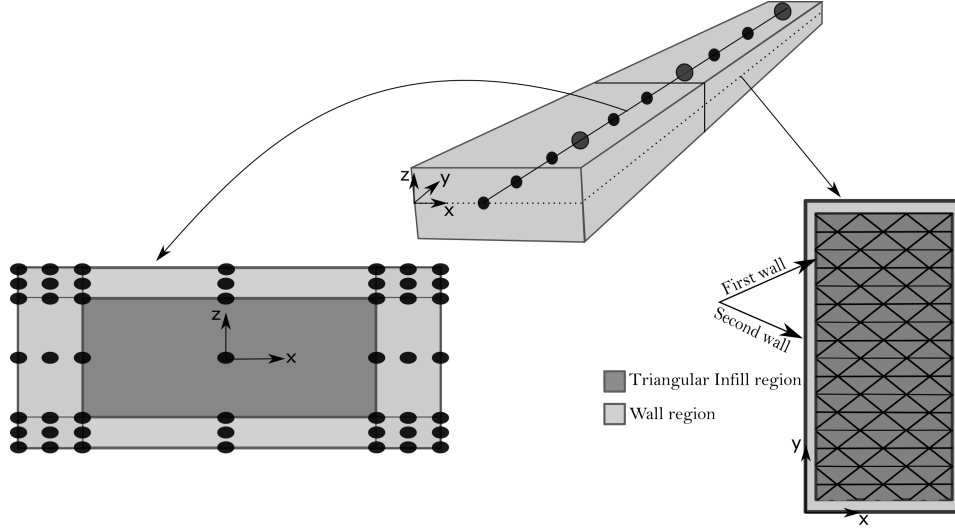


Figure 4.5: Left: Cross section L9 expansion discretization, middle: FEM discretization four noded beam element of MT printed laminated honeycomb (infill) beam, Right: Top view of the printing features of the infill region with triangular pattern

$$\mathbf{u}(x, y, z) = F\tau(x, z)\mathbf{N}_i(y)\mathbf{u}_{\tau i} \quad (4.11)$$

where $\mathbf{u}_{\tau i}$ represents the nodal displacements vector. various elements (B2: element with two nodes, B3: elements with three nodes, B4 element with four nodes are adopted in this work and the index i referred to the node of the beam element. The shape functions can be arbitrarily chosen but in this work the used shape function are reported in [132, 134–137]. The governing equations can be obtained via the Principle of Virtual Displacements (PVD) as in Eq. 4.12. In the static case, it is expressed as the equivalence between the work of the external loads (δL_{ext}) and the strain energy (L_{int}). The term δ denotes the virtual variation.

$$\delta L_{int} = \delta L_{ext} \quad (4.12)$$

The strain energy can be written as a function of the stress and the virtual strain components as below:

$$\delta L_{int} = \int_V \delta \boldsymbol{\epsilon}^T \boldsymbol{\sigma}, dV \quad (4.13)$$

$$\delta \boldsymbol{\epsilon} = bF_s(x, z)\mathbf{N}_j(y)\delta \mathbf{u}_{sj} \quad (4.14)$$

In accordance with the Hooke's law and the geometrical relations, the internal work can be defined as a

function of the shape functions and the expansion utilised will be to represent properties of the material and geometrical cross-section as in the following:

$$\delta L_{int} = \delta \mathbf{u}_{sj}^T \int_V \mathbf{N}_j(y) F_s(x, z) b^T \hat{C} b F_\tau(x, z) \mathbf{N}_i(y) dV \mathbf{u}_{\tau i} \quad (4.15)$$

in which, the stiffness matrix $\mathbf{K}^{ij\tau s}$ is denoted by the integral. It is represented in term of fundamental nucleus (FN). Consequently, to obtain the global stiffness matrix varying the indices i, j, τ should be done for a combination of i and j . The assembly of multilayered and multicomponent structures' stiffness matrix can be achieved by two methods based on the approach used (LW, ESL or CW) as shown in Fig. 4.6 and is discussed in the following. For example, the first one on the top right is used for Taylor expansions and sums the contributions of each single layer into an one equivalent. Instead, LW models (shown in the middle of Fig. 4.6 permits taking the generalised displacements of each individual layer independently. Then, compatibility conditions are imposed at the interfaces of two consecutive laminae by considering the following:

$$\mathbf{u}_{top}^k = \mathbf{u}_{bottom}^{k+1} \quad (4.16)$$

where k indicates the k -th layer of the MT printed laminate. Pagani et al. [138] was the first to introduce employing Hierarchical Legendre expansion (HLE) for the analysis of classical laminates and thin-walled structures and, more recently, LE was applied for the study of VSC by Viglietti et al. [139, 140]. Based on this approach, and taking advantage of the CUF capacities, the LW modelling can be extended straightforwardly to any component on the cross-section with no loss of generalisation (i.e case of CW). Indeed, by extending the meaning of the index k from the layer to a generic component of the cross-section, one can generate independent kinematics for the matrix, the fibre or any other component and then impose the compatibility of displacements at the interfaces. Thus, the assembly of the stiffness matrix of a component-wise (CW) model remains formally the same as that of LW approaches. Finally, the loading vector can be achieved from the external work and by substituting in Eq.4.12 as.

$$\delta L_{ext} = \delta \mathbf{u}^T \mathbf{P} = \delta \mathbf{u}_{sj}^T \mathbf{N}_{jp} F_{sp} P \quad (4.17)$$

where, N_{jp} and F_{sp} are the values of the evaluated function at the point load (\mathbf{P}) application.

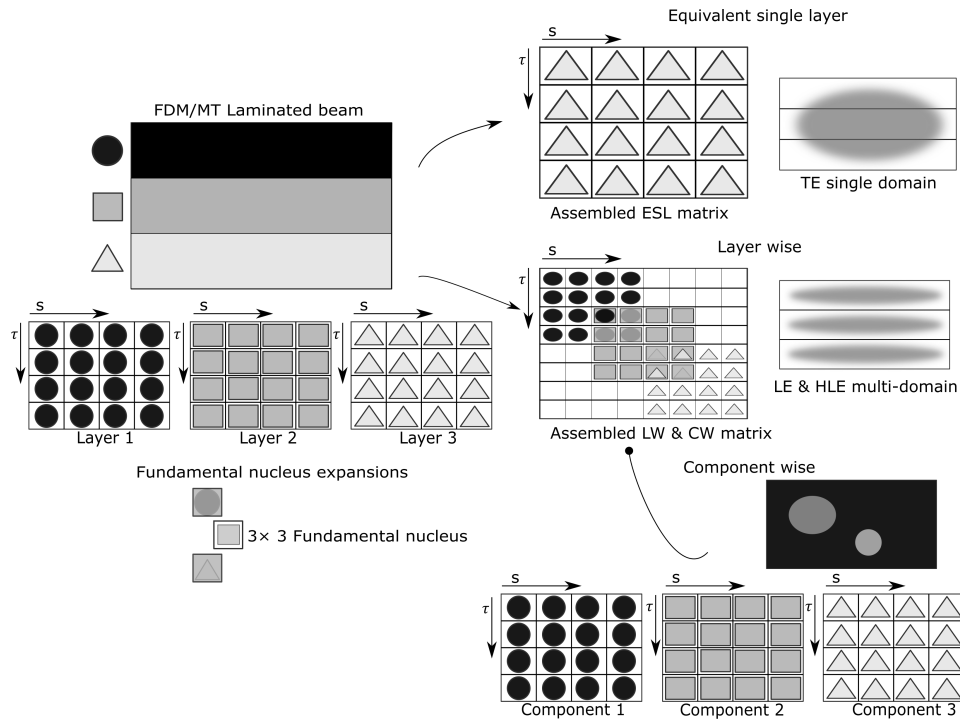


Figure 4.6: Assembly procedure of the stiffness matrix through ESL, LW and CW approaches

4.3 Modeling Techniques and Guidelines for MT Structures

The preprocessing of a MT laminated composite structure finite element analysis is a very crucial step as the MT structure includes several regions, for instance, floor, roof and infill region as well as reinforcement layers and their orientation, hence defining the model and taking into consideration all details accurately is a challenge and time consuming. Moreover, it determines the quality of the simulation and consequently the accuracy of the results. Therefore, opposed to complexity of most of the commercial preprocessing packages, CUF preprocessing developed for 3D printed structures, in particular, MT parts simplifies the definition of MT printed structures in an easy and time efficient way. Therefore the kinematic depends from the elements used in the expansion. CUF-3D capture all the detailed cross-section. Further, it enables the end-user to refine the mesh, and within reasonable limits, the geometry, in order to obtain finer results. The CUF-3D preprocessing has been written using python 3.9 programming language, in the next section, code manual is introduced as well as some of the equations used including discretization convention sign, material modeling, and defects appeared in the 3D-MT parts.

4.3.1 CUF Requirements and Installtion

The software is available to download freely at www.mul2.polito.it. The operating system required is windows, for further details check the manual at the MUL2 group website. Moreover, it is suggested to download notepad++ and paraview; all requirements are not equally important, CUF can run without these prerequisites, however, the visualization of the results might not be appeared without such prerequisites. The description of the model including, geometry, discretization, material properties, ply book, analysis type, and boundary conditions should be added/defined in a notepad file and should be named as "*CUF_iinputs*". In addition, genetic algorithm can be defined so an optimization specimen can be produced. Figure 4.7 contains a flow diagram of the dependencies of the new module CUF-3D in MUL2 software.

in which input file contains seven sections. For example, the user required to create geometry by adding length, width, thickness and number of actual printed layers. Then it is required to define the number of nodes per each element and number of element as well as kinematic model whether Taylor (TE) or Lagrange (LE) and their expansion number Figure 4.8 illustrates an example of input file which describes the model.

4.4 Numerical Results

Three distinct cases of beams are considered and compared to analytical solutions and/or commercial software package ABAQUS to verify the accuracy of the CUF towards MT printed specimens. In the first case, a cantilever beam made up of fifty isotropic layers is considered. The geometric features of the structure are shown in Fig. 4.9a. The material used is nylon with the Young modulus and the Poisson's ratio equal to 940 MPa and 0.34, respectively. The second case is considering a cantilever beam made up of seven orthotropic layers with the geometric features and LSS of the structure as presented in Fig. 4.9b. Analysis are carried out considering a square cross section with a concentrated load of $F_z = -10\text{N}$ that is applied on the free tip. The third case has the same geometric and LSS of the second but with different boundary condition as simply supported. Isotropic material layer is labeled with the number 1, whereas orthotropic material is labeled with the number 2. Before the finite element analysis (FEA) of 3D MT printed composite beams is reported. It is important to consider the results from the convergence study. Table 4.2 illustrates the material used and summarize the LSS for various

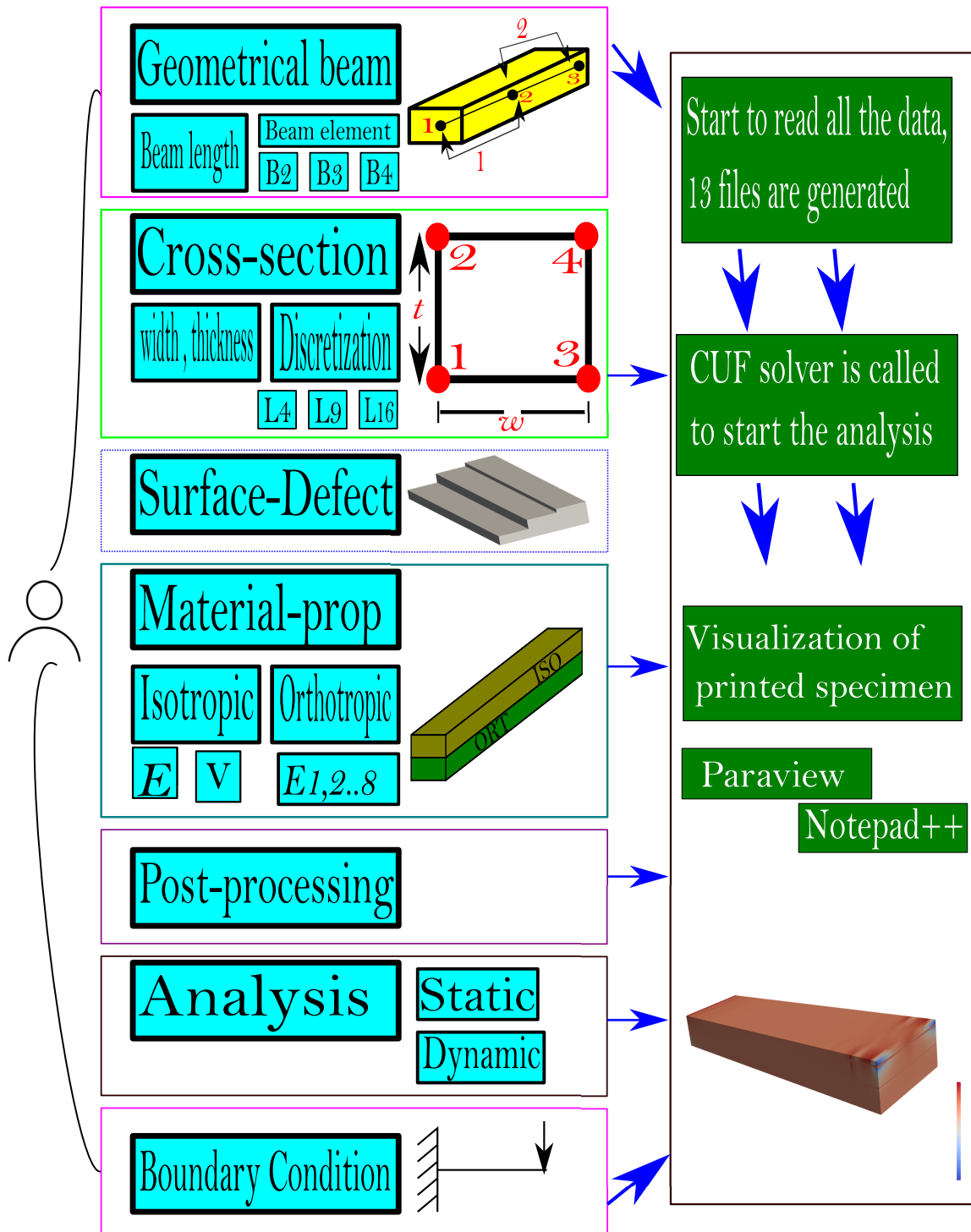


Figure 4.7: Flow diagram of the novel CUF 3D

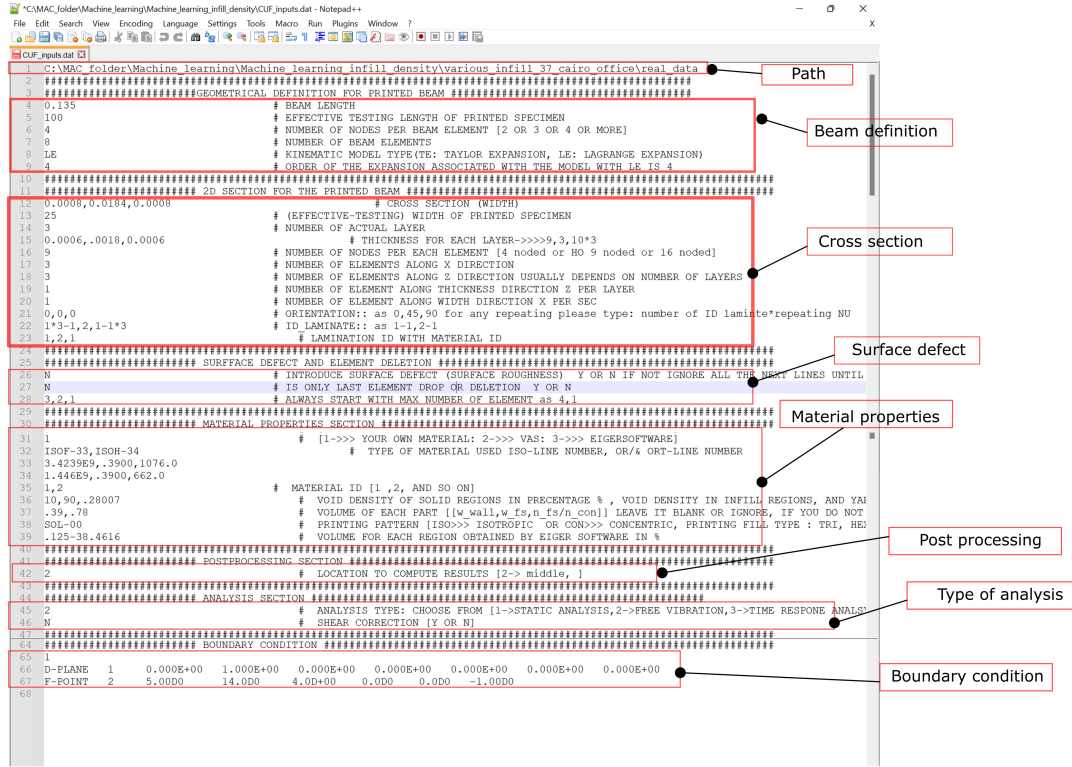


Figure 4.8: Example of CUF-3D input file

cases considered.

Figures 4.10 and 4.11 present the convergence study of first case (ISOCB) for σ_{yy} and σ_{yz} , respectively. In which, B2 (two node element), B3 (three node), and B4 (high order four node) represents the number of nodes per element. Also, the index (i) B_i shows the number of elements used in the convergence study.

It can be seen that, it is important to consider the convergence study to choose the correct /suitable number of elements as it affects the results especially in the shear stresses in case of cantilever and normal stresses in case of fixed ended. The study shows that eight to ten finite elements must be

Table 4.2: Material properties and LSS used for the numerical analysis

Material type	$E_1 (MPa)$	$E_2 = E_3$	ν_{12}	$\nu_{13} = \nu_{23}$	G_{12}	$G_{13} = G_{23}$
Carbon-fiber	50210	1552.34	.3807	.0141	18182.81	765.38
Nylon	940	940	.39	.39	-	-
Sample	LSS					
Cantilever beam "ISOCB"	$[N]_{50}$					
Cantilever beam "ORTCB"	$[N_4/CF_3/N_{17}/CF_2/N_{17}/N_4]_T$					
Fixed ended "ORTFE"	$[N_4/CF_3/N_{17}/CF_2/N_{17}/CF_3/N_4]_T$					

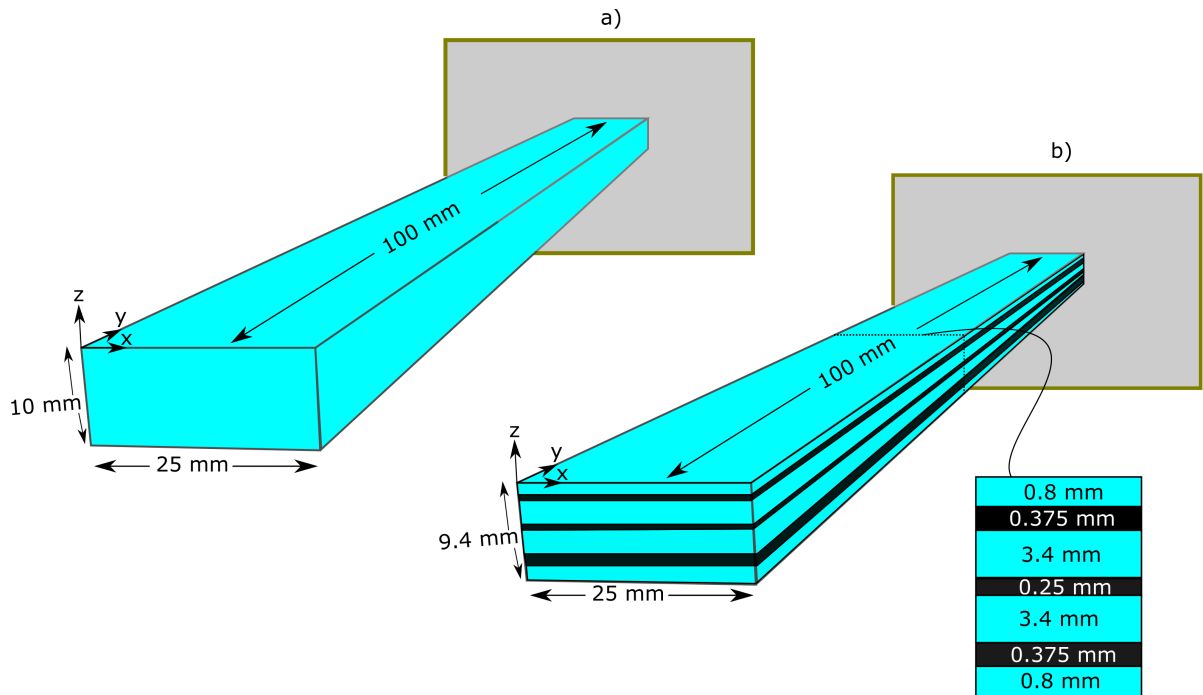


Figure 4.9: a) The fifty-layer nylon printed beam, b) The fifty-layer CFN printed beam

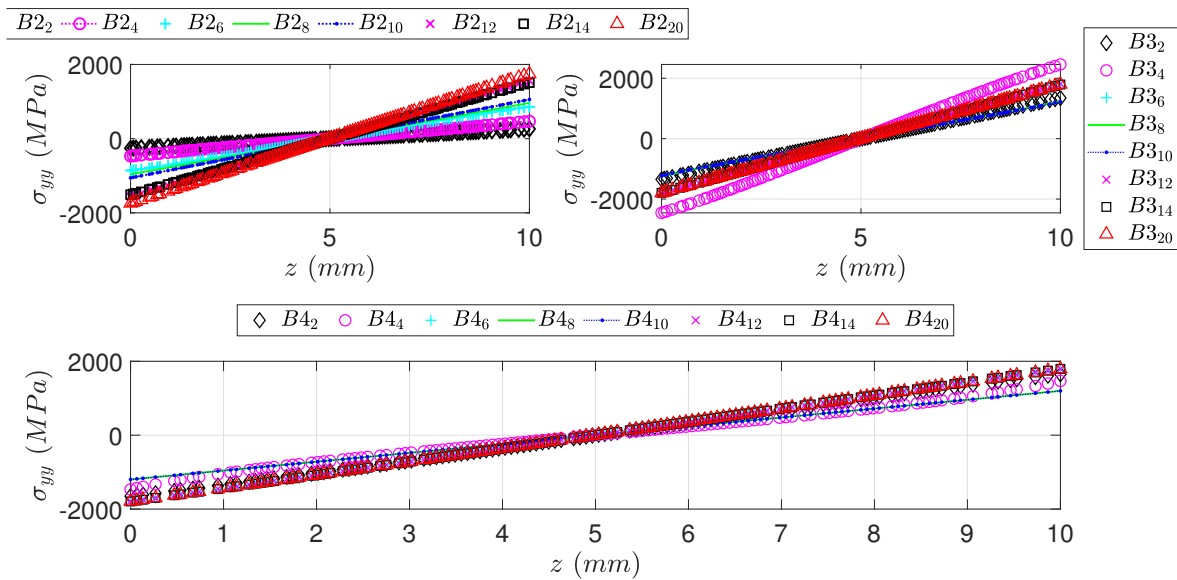


Figure 4.10: Mesh Convergence Study for σ_{yy} with different beam elements at L9

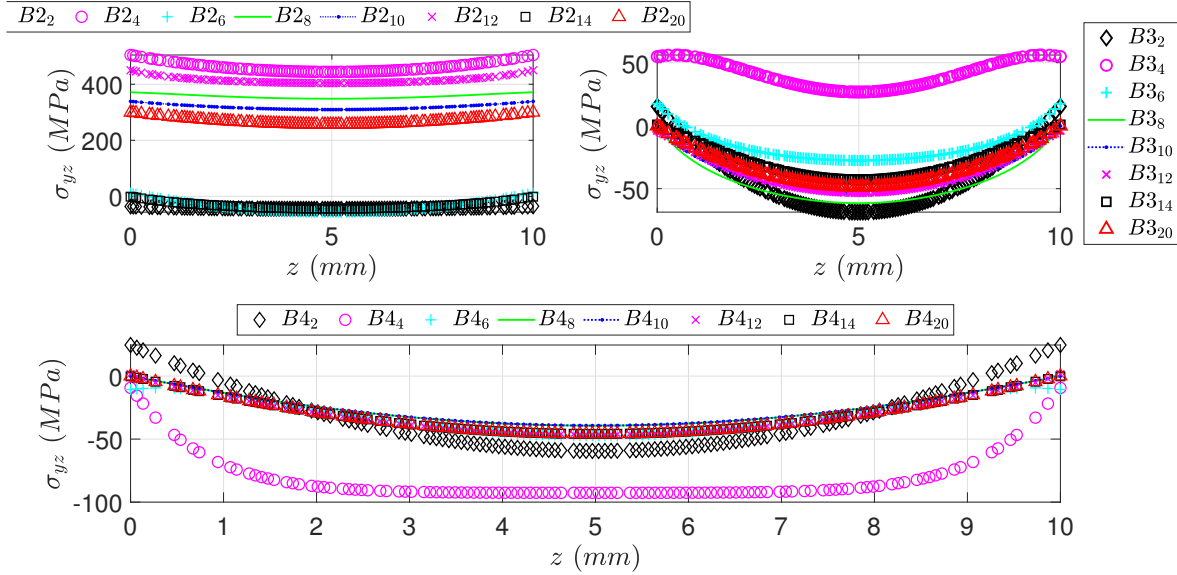


Figure 4.11: Mesh Convergence Study for σ_{yz} with different beam elements at L9

used to ensure the convergence.

4.4.1 Analysis of MT Printed Beams

In order to ensure the convergence, ten finite elements are used to model the structure along the y -axis. The structure is loaded at the tip by a concentrated load of $F_z = -10N$. The results are illustrated in a numerical and graphical form. In Fig. 4.12 the distribution of σ_{yy} and σ_{yz} at mid-span for a variety of expansions are shown. These distributions are compared with the analytical solutions derived by theory of elasticity reported in Lekhnitskii et al. [141].

It can be noted that Lagrange B3 and B4 noded beam elements are in strong agreement with the analytical results for both normal and shear stresses. However, as expected Taylor with low expansion gives incorrect results. Instead, by increasing the Taylor expansion, the results becomes more close to the correct results.

For the orthotropic MT printed cantilever "ORTCB" case, Figs .4.13 and 4.14 present the distributions of σ_{yy} and σ_{yz} , respectively at mid-span for a variety of expansions compared to both analytical solutions derived by theory of elasticity reported in Lekhnitskii et al.[141] and solutions performed in a commercial FEA package ABAQUS. The element type used in ABAQUS was solid element C3D20 and continuum shell elements SC8R. It is revealed that results provided by LE with

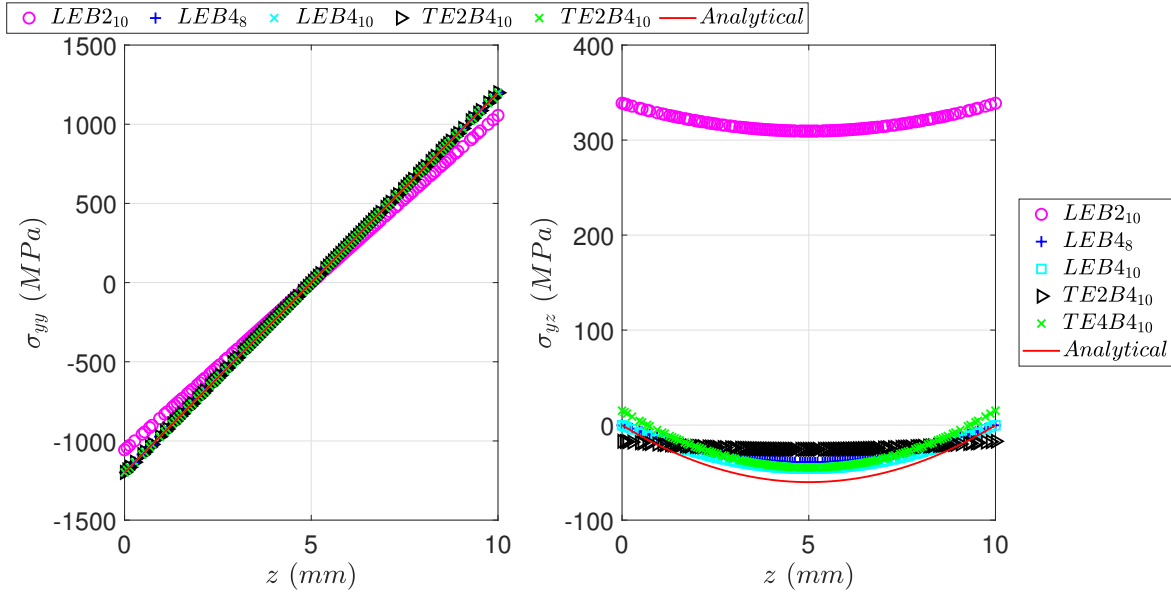


Figure 4.12: Distribution of stresses through the thickness of a cantilever beam (ISOCB):
left) σ_{yy} , right) σ_{yz}

Table 4.3: Comparison of DOF, stresses generated from various models

FE Mesh	DOF	σ_{yy}	σ_{yz}
Analytical	—	87.7	-47.4545
CUF 10 – B4 – TE2	198	112.2661	-35.0283
CUF 10 – B4 – TE4	1395	111.9462	-25.0162
CUF 10 – B2 + Q9	9999	100.1374	13.6335
CUF 10 – B4 + Q9	28179	87.8582	-48.2126
Abaqus Continuum shell-SC8R	143418	78.09	—
Abaqus 3D solid-C3D20	220464	85.5	-49.4

B4 noded beam element expansions are in strong agreement with the analytical solution both in term of normal, shear stresses while in contrast, the remaining LE with B2 noded beam element, TE_4 and TE_2 , theories underestimate, generally, the shear stresses. On the other hand, if we consider the distribution of the shear stress, σ_{yy} (see Fig. 4.13), the best solution is furnished by (LE) with high order beam element. In Table 4.3 the degree of freedoms, normal and shear stresses computed along the thickness are compared to the analytical results. In addition the results are compared to different element type used in ABAQUS.

Moreover, For the orthotropic MT printed fixed ended "ORTFE" case, Figs. 4.15 and 4.16 show the distributions of σ_{yy} and σ_{yz} respectively at quarter-span for a variety of expansions. The

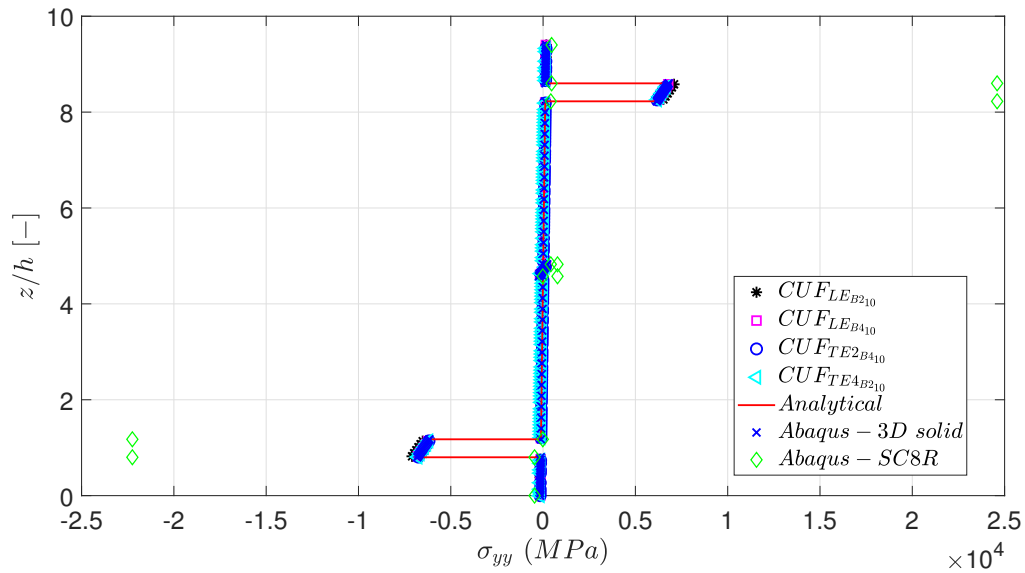


Figure 4.13: Distribution of stresses σ_{yy} through the thickness of a composite cantilever beam (ORTCB)

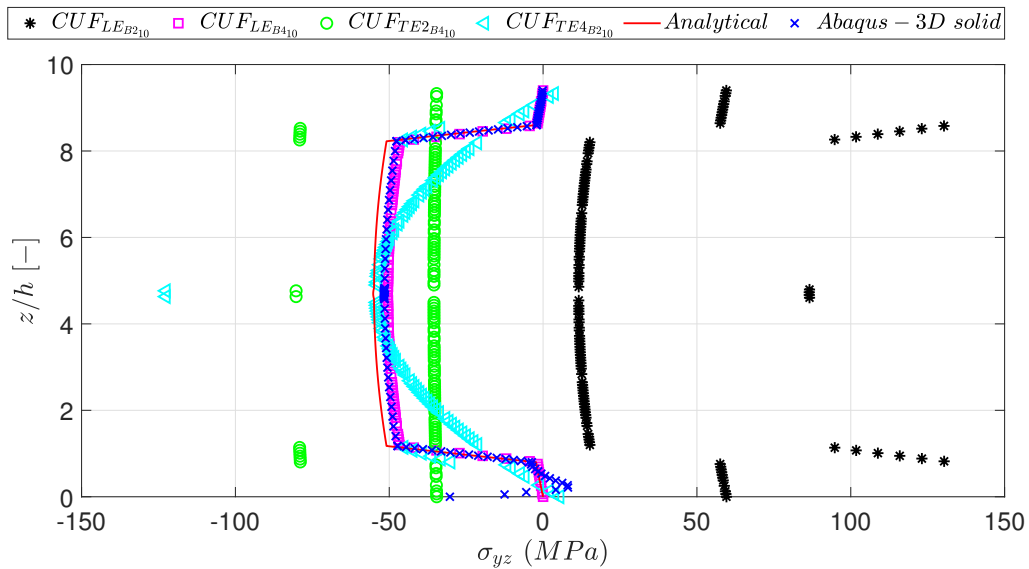


Figure 4.14: Distribution of stresses σ_{yz} through the thickness of a composite cantilever beam (ORTCB)

Table 4.4: Comparison of stresses generated from various models for fixed ended beam

FE Mesh	DOF	σ_{yy}	σ_{yz}
CUF TE2-B4-12	198	-2.3093	-18.4820
CUF 12B2+Q9	1395	-4.0448	-25.1026
CUF 12B3+Q9	9999	-2.2390	-25.5469
CUF 12B4+Q9	28179	-2.2346	-25.7984
Abaqus 3D solid	220464	-2.5497	-25.5279

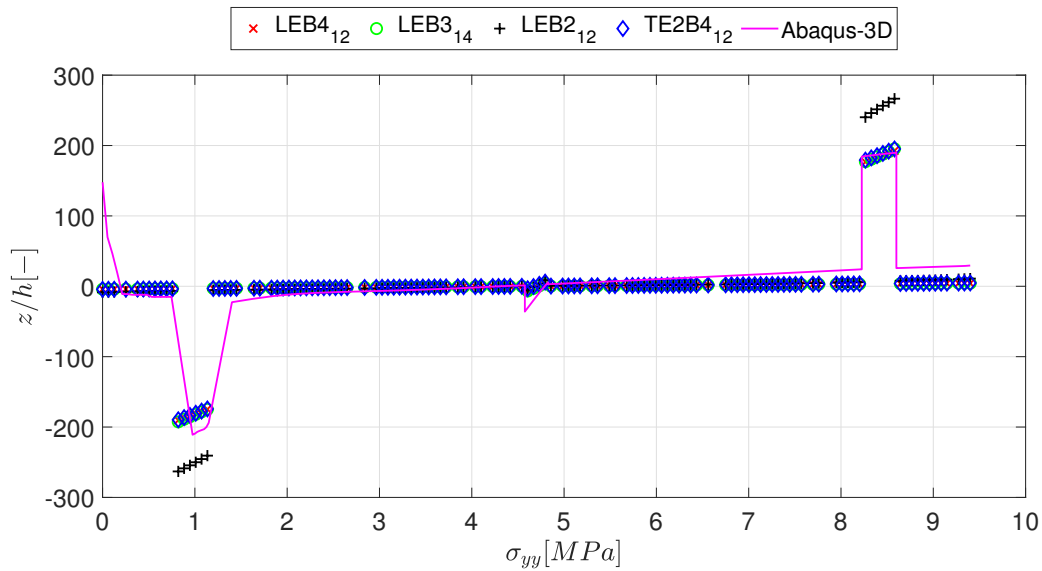


Figure 4.15: Distribution of stresses σ_{yy} through the thickness of a composite fixed ended beam (ORTFE)

results are then compared solutions performed in a commercial FEA package ABAQUS mainly solid element C3D20. The results have the same behaviour of the previous case (ORTCB), however it can be noted that the model requires more number of elements through the thickness. revealed that results provided by LE with 4 noded beam element expansions are in strong agreement with the analytical solution both in term of normal, shear stresses while in contrast, the remaining LE with 2 noded beam element, TE_4 and TE_2 , theories underestimate, generally, the shear stresses. On the other hand, if we consider the distribution of the shear stress, σ_{yy} (see Fig. 4.13), the best solution is furnished by (LE) with high order beam element. In Table4.3 the degree of freedoms, normal and shear stresses computed along the thickness are compared to the analytical results. In addition the results are compared to different element type used in ABAQUS.

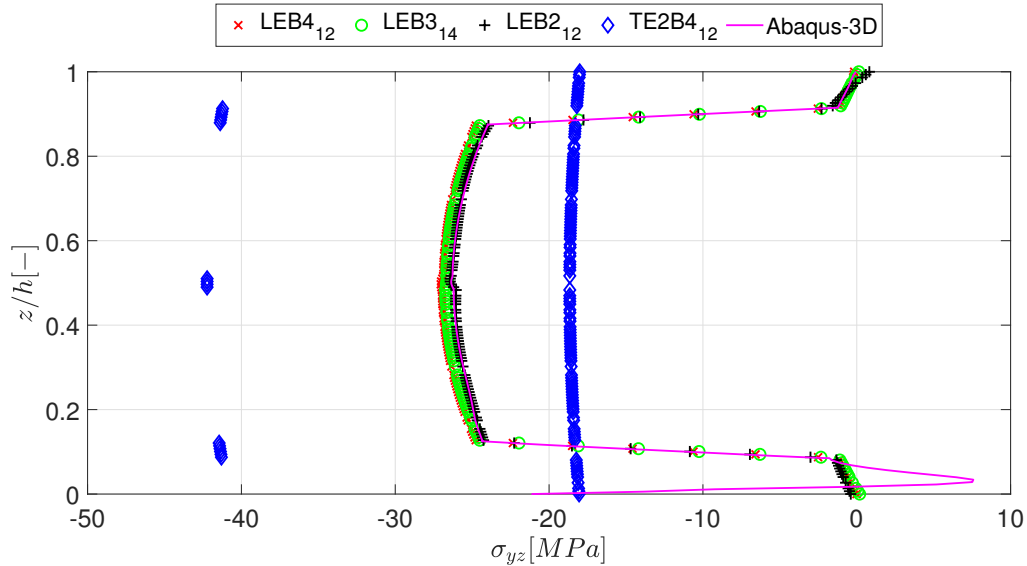


Figure 4.16: Distribution of stresses σ_{yz} through the thickness of a composite fixed ended beam (ORTFE)

4.5 New Approach for FDM/MarkTwo Material Characterization

Most studies use the experimental approach to characterize material properties of the FDM/MT printed structures and since setting up experimental work are laborious as an extensive experimental tools is required, a paradigm to obtain the properties via a fast numerical tool is of interest. For example, a lot of research was carried out to investigate property structure relationship in 3D printing/FDM printing to understand the several parameters influence on the material properties including printing temperature, infill angle, and densities, and layer thickness [17, 142–149]. Melenka et al. [100] obtained elastic properties of kevlar reinforced structures printed by a MarkOne and apply volume average stiffness method (VAS) to predict the elastic properties *. Abadi et al. [99] developed mathematical expressions for assessing elastic properties of fiber reinforced structures printed using FDM. Consequently, accurate models are needed to provide a clear understanding of their structural performance without the need for many experimental work. Various numerical studies have been done for the analysis of the FDM parts. For example, Masrol and Siswanto [150] carried out a numerical simulation using various element types. Coelho et al. [151] used the available predictive capabilities in a commercial finite element analysis software Abaqus. Abadi et al. [99] utilizes the Abaqus software to predict the

*For more information regarding analytical method VAS, please review Sec. 3.3.2

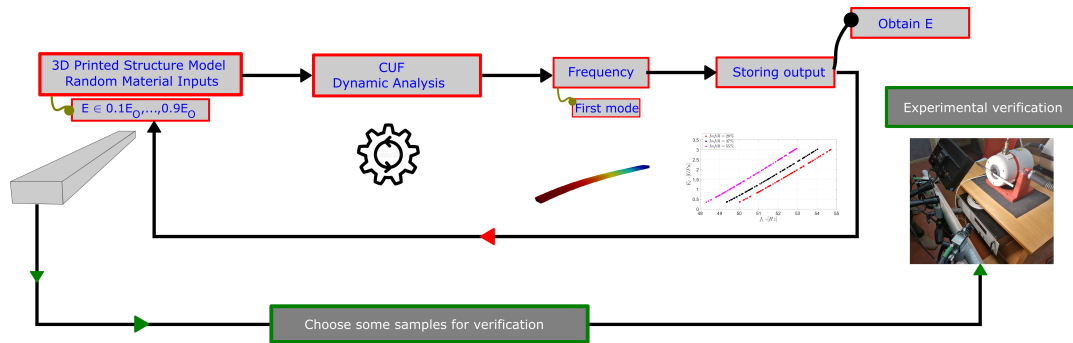


Figure 4.17: Flowchart for the new approach of predicting material properties of 3D-FDM structure

damage and failure modes in the FDM printed coupons.

Given the mentioned previous work, and in addition to, existing micro and meso numerical models are exhibited in the literature to simulate and analyze the mechanical behavior of FDM printed part [152]. However, there is still a gap in obtaining the material properties used (e.g. elastic modulus) in the infill component as it is usually unknown and sensitive to such specific parameters used (e.g. infill density), making the numerical simulation is elusive and inaccurate.

To circumvent that research absence, developing a way for the accurate prediction of material properties for different components within the MT printed structures is a challenge. In view of this, CUF-CW approach mentioned in the previous section has been applied to give accurate results [128, 129, 153, 154] with low computational cost. The current section aims to characterize the material properties based on the inverse problem formulation. The inverse problem approach proceeds in the opposite direction with respect to standard forward models. Leverage the resulting numerical model explained earlier in Sec. 4.2.3 to build a data driven model that allows obtaining directly the material properties. Free vibration experimental test has been performed to validate the accuracy of the proposed approach. The first fundamental frequency and mode was evaluated by using the digital image correlation (DIC) technique. Figure 4.17 presents the flowchart of the new approach procedures, and in the next subsections, we will explain in details.

4.5.1 Infill Material Characterization

The beams considered for the infill region material characterization have the following geometrical features: length of 135 mm, thickness of 3 mm, and width of 20 mm as shown in Fig. 4.18.

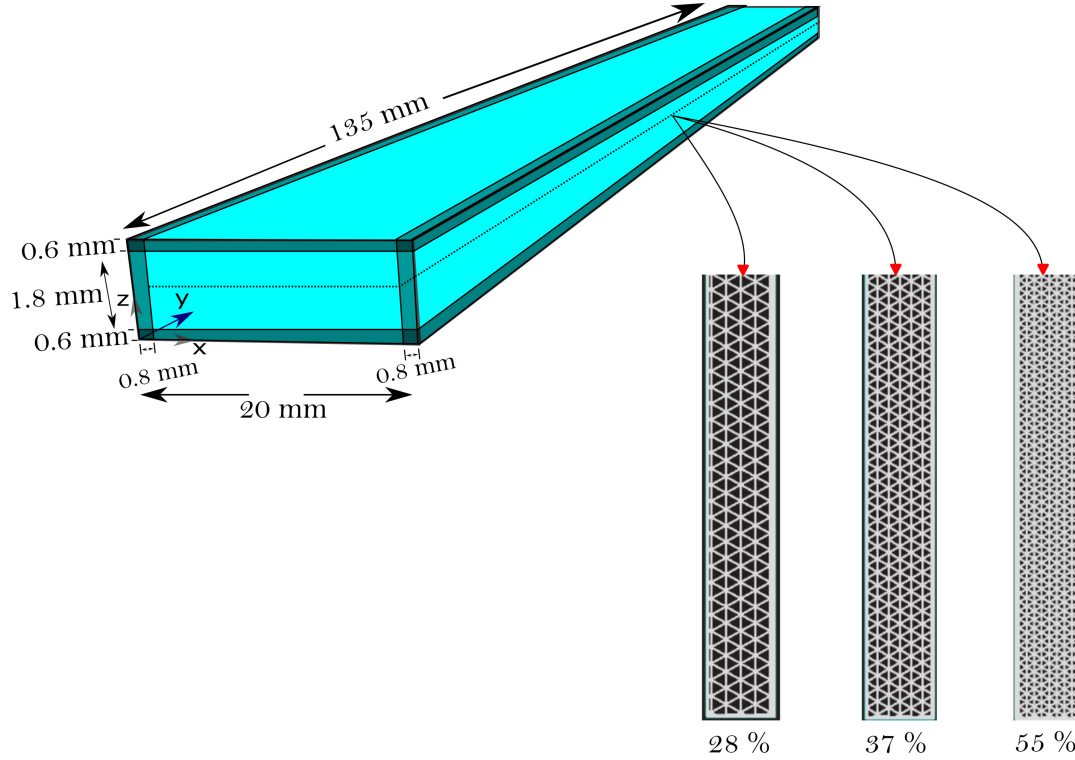


Figure 4.18: Left: Infill beam considered for infill component material characterization, right: Top view of infill part within the beam

For instance, three layers in floor of total thickness of 0.6 mm and roof components of same value were considered. Instead, the infill region has 1.8 mm of thickness (9 layers, each layer of 0.2 mm) and width of 18.4 mm. Figure 4.18 shows the infill internal top view of various infill densities included.

First, we carry 100 randomly simulation, whereupon, a set values between 0.1 and 0.9 of Young's modulus of onyx captured from Markforged[®] datasheet mentioned earlier in Ch. 3 in Table 3.4 ($E_{O_r} \in [0.1E_O, \dots, 0.9E_O]$). In which, E_{O_r} is the generated values of the onyx modulus of elasticity, while E_O indicate to modulus of elasticity of onyx obtained from datasheet available. The infill density experimentally measured for 28% is 622, 37% is 662, and finally 55% is 728 kg/m^3 . Figure 4.19 reports the dynamic responses outputs in form of database. The results presents the first natural frequency mode based on possible input parameters of Young's modulus with density adopted experimentally for various infill percentages.

It is shown that, the Young's modulus of infill is increased by increasing the percentage of the infill as expected. In the next section, experimental verification will be done to verify the accuracy of the proposed approach.

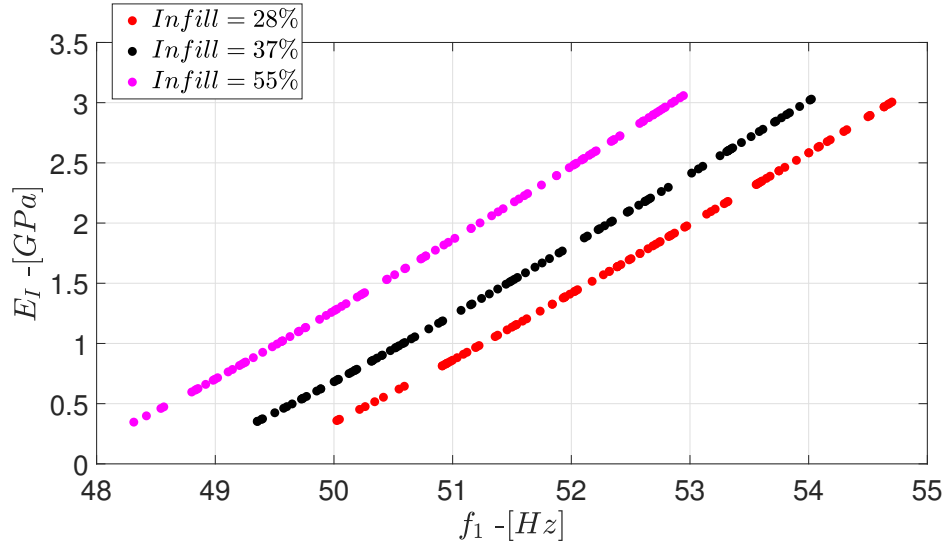


Figure 4.19: Scatter plots comparing the observed frequency for first mode of the various FDM infill beams

4.6 Experimental Verification

Since, in the above section we present a new approach for the infill component material characterization, so to verify the approach we consider several beams including printing at least three layers of onyx at the floor, roof regions, and two lateral polymeric material (wall component) should be placed around the border of each layer. Then, the filling percentage of 28%, 37%, and 55% is added. Figure 4.20 shows the electro-dynamic shaker testing system by Brüel and Kjaer[®] which was used to perform free vibration analysis. The shaker testing system generates different range of frequencies up to 500 hz. The results have been calculated by means of a Q-400 Digital Image Correlation (DIC) system by Dantec Dynamics[®]. It can measure true full field, non-contact and three dimensional shape, strains and various displacements on structure produced with any material. Figure 4.20 presents the DIC equipment attached with the specimen, that is composed of 2 megapixel cameras for high-frequency image tracking, one light source, as well as data acquisition unit.

Table 4.5 illustrates the first natural frequency mode of both predicted results and experimental obtained via DIC for various beams with different infill percentages. Moreover, the predicted infill modulus of elasticity based on the inverse formulation for the 28%, 37%, and 55% infill percentages is presented in Table 4.5. In which, f_1 -Exp refer to the experimental results obtained and $f_1 - CUF$ is the numerical results calculated via CUF-CW random generation. E_I is infill modulus



Figure 4.20: Left: Electro-dynamic shaker testing system, right: digital image correlation

Table 4.5: Validation of results between experimental and CUF-CW modeling of various Infill percentages

Model	$f_1 - \text{Exp}[\text{Hz}]$	$f_1 - \text{CUF}$	$E_I - [\text{GPa}]$	$\rho_e - \text{Kg}/\text{m}^3$
100SW20T3	46.077	47.158	-	1144.000
28TRI20T3	50.664	50.664	0.682	622.000
37TRI20T3	51.370	51.972	1.446	662.000
55TRI20T3	51.225	51.028	1.997	728.000

of elasticity obtained by inverse method and ρ_e is the density of the considered infill beams obtained experimentally.

The Table revealed that, by increasing the percentage of the infill, infill material properties are increased. Further, infill region material properties has great sensitivity for the density of the infill part. Therefore, it is important to include the correct values of the infill material properties to get an accurate simulation results, which can be used later in advanced mechanical studies such as optimization of 3D printed parts.

4.7 Static Condensation

MT is considered to be promising in producing multi-body parts and smart structures as will be presented later in Chapter 5, however the computational cost for analyzing such structures is too ex-

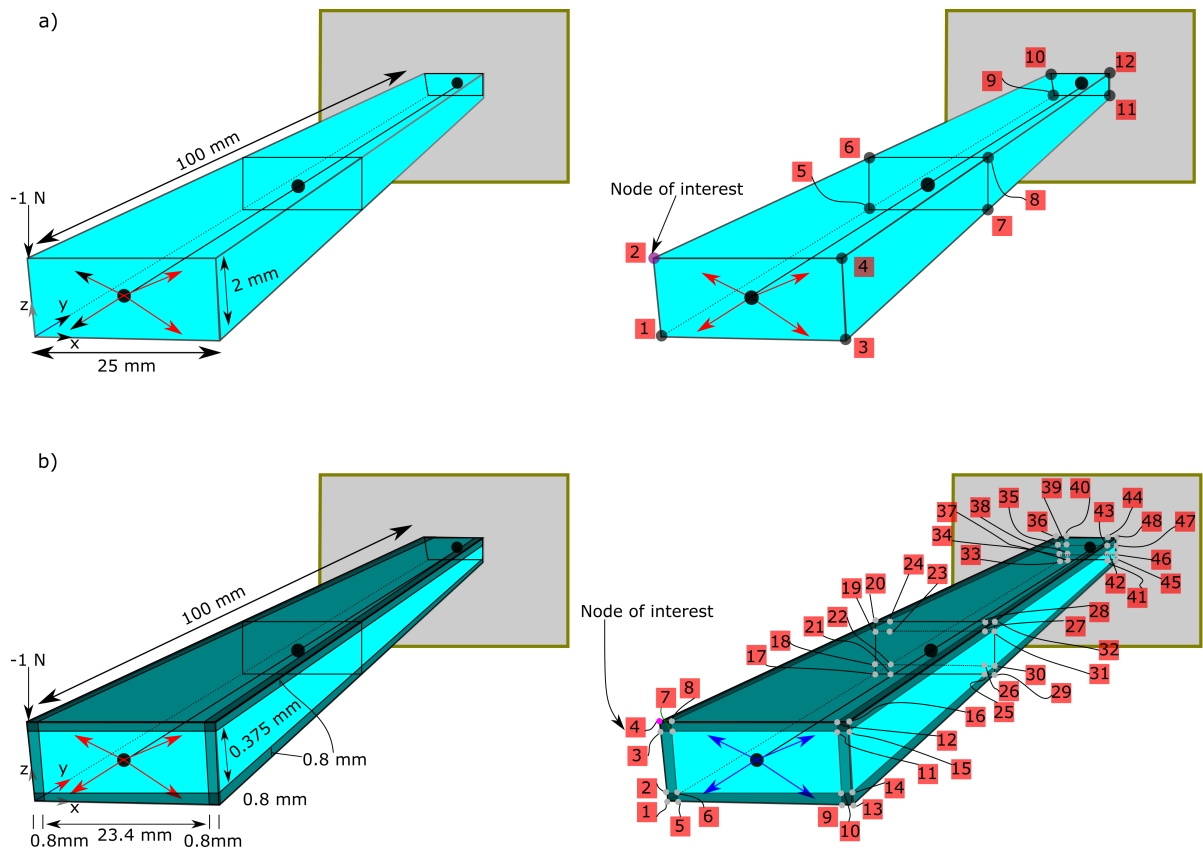


Figure 4.21: a) Left: Generic isotropic solid FDM structure with equivalent single layer (Taylor), Right: Layerwise (Lagrange polynomials); b) Left: Generic FDM composite structure with equivalent single layer (Taylor), Right: Layerwise (Lagrange polynomials)

ensive and/or analytical models is still limited or elusive to be obtained. Static condensation approach is usually used in big structures or multi body applications in which number of degree of freedoms in an analysis can be reduced and hence stiffness matrix is reduced as well. It is actually performing part of the solution before assembling the system of equations. This results in a huge computational cost reduction. This is achieved by arranging the nodes of interest (needs to be reduced or condensed) in the first nodal coordinates and the remaining primary degrees of freedom are the last p nodal coordinates. Figure 4.21a illustrates an example of a cantilever beam made up of isotropic material discretized with L4 and one element of 3 noded beam element; in which, equivalent single layer (Taylor) approach presented on the left, and layerwise (Lagrange polynomials) on the right. While, FDM composite structure made up of three layers is shown in Fig. 4.21b.

To verify the efficiency of the proposed method, two cases are investigated as presented in Table 4.6; first is an isotropic beam made of onyx and second is a composite structure made of three

Table 4.6: Models parameters used for static condensation verification

Sample	dimensions-mm	LSS
ISOCB	L= 100, W= 25, T = 2	-
ORTCB	L= 100, W=25, T = 1.975	$[O_4, CF, O_4]_T$

layers (floor and roof layers are made of onyx and middle layer of carbon fiber). The node of interest for the first case is node number 2, while node number 4 for the composite beam case. The geometrical features is presented in Table 4.6. The material properties of the first case are adopted from Table 3.4 mentioned earlier in Ch. 3, while in the second case the material properties are utilised from Table 4.2.

With such procedure the stiffness equation for a structure can be represented as presented below:

$$\begin{Bmatrix} K_{ss} & K_{sp} \\ K_{ps} & K_{pp} \end{Bmatrix} = \begin{bmatrix} u_s \\ u_p \end{bmatrix} = \begin{bmatrix} F_s \\ F_p \end{bmatrix} \quad (4.18)$$

in which u_s is the displacement vector corresponding to the slave degrees of freedom to be reduced and u_p refers to the vector containing the remaining p primary degrees of freedom. A simple multiplication of the equations system in Eq. 4.18 yields the following two matrix equations:

$$[K]_{ss}u_s + [K]_{sp}u_p = F_s \quad (4.19)$$

$$[K]_{ps}u_s + [K]_{pp}u_p = F_p \quad (4.20)$$

By solving Eq.4.19 for the displacement vector u_s and subsequently substituting it in Eq.4.20. This results in Eq.4.21

$$u_s = [K]_{ss}^{-1}(F_s - [K]_{sp}u_p) \quad (4.21)$$

$$\bar{F}_p = [\bar{K}]u_p \quad (4.22)$$

where, \bar{F}_p is the condensed stiffness equation. $[\bar{k}]$ refers to the condensed stiffness matrix and \bar{F}_p refers

Table 4.7: Comparison of Displacement obtained by full K and condensed matrix

Sample	FE Mesh	DOF_f	DOF_r	$\delta_{z_f} - [mm]$	δ_{z_r}
ISOCB	CUF 1 - B3 + L4	36	3	-5.813	-5.813
ORTCB	CUF 1 - B3 + L4	144	3	-7.403	-7.403

to the force vector.

$$\bar{F} = F_p - [K]_{ps}[K]_{ss}^{-1}F_s \quad (4.23)$$

$$[\bar{K}_{red}] = [K]_{pp} - [K]_{ps}[K]_{ss}^{-1}[K]_{ps} \quad (4.24)$$

Therefore, the solution of the above equation 4.22 give the displacement vector u_p at the primary nodal coordinates and the reduced displacements u_p . Table 4.7 shows the two cases considered.

where, DOF_f is the degree of freedom of the whole system, whereas, DOF_r is the degree of freedom of the reduced system. δ_{z_f} and δ_{z_r} refers to the displacements in the z direction for full system and reduced system respectively. It can be noted that, the reduced stiffness matrix provides a very precise results to the whole system.

4.8 Conclusion

In this chapter, several one-dimensional finite elements based on different kinematic/Lagrange and Taylor expansions in accordance with the Carrera's Unified Formulation (CUF) have been employed to verify the capability of CUF to analyses the laminated MT beams. A novel preprocessing platform within CUF frame-work has been developed in one single computer program to describe the model in an easy and time efficient way. It also accounts the several regions appeared in the laminated MT structures. To verify the proposed model, various cases are considered in terms of LSS and boundary conditions. Hence the following final remarks can be made:

- The current proposed tool (CUF-CW) formulation-1D models are able to analyze 3D-FDM printed laminated beams and provide accurate solutions with very low computational cost compared to 3D solid FE, and have the ability to include all the regions/components within the printed structure.

- The computed results indicate that for isotropic case, all the TE and LE models can produce good results. However, orthotropic cases LE four noded beam elements are the most accurate models.
- The exponential function becomes very important when the structure is cantilever.
- The results obtained indicate that higher order four noded-beam (B4) elements are considered to be valuable for the investigation of the static behavior and gives very accurate results.
- CUF-CW model can be leveraged for retrieval of the mechanical properties for different geometrical features and infill percentages as presented in Fig. 4.17.
- Onyx infill material properties are very sensitive to the infill density, which affects the accuracy of the simulation and optimization problem.
- Static condensation can be easily applied to reformulate the stiffness and mass matrices based on partitions of the stiffness matrix
- Micro-scale analysis should be considered to account the voids appeared in the MT structures.

Chapter 5

Industrial Application

Three dimensional (3D) printing is used in the industrial field for fast prototypes. Recently, its usage has been expanded for the production of end user parts which require major customization. Opposed to material subtractive techniques (MST) 3D printing can be used to produce complex shapes. Topology optimization (TO) integrated with 3D printing can be considered to be a powerful tool which will be capable of producing components characterized by similar stiffness but smaller inertia than those manufactured by MST, which is useful in high-speed automatic machinery design which requires motor torque reduction to minimize costs and energy consumption. Moreover, size optimization (SO) can be integrated with TO and 3D printing to fabricate components characterized by proper stiffness to be included in mechanism to tune their dynamic mechanical characteristics. In fact, due to their ability to passively store and release mechanical energy, elastic elements can replace those conventional elements to compensate kinetic energy variations, which drastically reduce motor torque requirements. The required elasticity can be easily introduced in the mechanism by replacing standard kinematic pairs with compliant joints (CJ) in the form of flexible MT laminated composites, also assuring lightness, precision and ease of realization.

This chapter analyzes the potentiality of FDM/MT in combination with TO and CJ design (CJD) for the realization of automated machinery mechanisms subjected to inertial loads. A pusher mechanism is considered: both the advantages and disadvantages of adopting the procedure are shown with respect to the standard steps. This chapter is organized as described in the following. First, an introduction about structural optimization, including their different techniques and automated production machines, is presented in Sec. 5.1. Description of the original mechanism and of the procedure for its redesign are presented in Sec. 5.2. Fabrication of mechanism by means of MarkTwo® (MT) is presented in Subsection 5.2.1. Substitution of links and kinematic pairs with CJ is reported in Subsection 5.2.2; SO of the flexible MT laminates in 5.2.3 and mechanical dissipation analysis are reported in Sec. 5.2.4. Finally, some meaningful conclusions based on the above analysis are obtained.

5.1 Introduction

Structural optimization is a major key in the industrial field and optimization modules are available in most CAD/CAE software. In general, optimization allows the designer to introduce the best structure geometry [155] that ensures both high-performance mechanical behavior (i.e. high stiffness, given natural frequencies, low weight and actuation torque/force) and cost effectiveness. Among the available structural optimization methods, SO are the most used approaches [156–163].

TO is a finite element (FE) based method that optimizes the material arrangement within a given design space (that is constituted by a FE mesh) for given boundary and constraint conditions. This process results in a complex shapes that are often elusive to manufacture with MST, unless proper manufacturing constraints are added in the optimization, which however greatly limits its potentiality. Consequently, TO is typically used in association with 3D printing. A more suitable approach for MST is SO: starting from some boundary, constraint conditions and one or more cost functions, SO seeks the result by changing the domain parameters of the geometry (such as the component thickness or width). Due to the high-volume production associated with MST, applicability also to 3D printing and lower computational burden than that of TO, SO is currently the most used design method in the industrial field. It also provides a very efficient CAD/CAE interaction: the parameters defined with the CAD tool are easily used for the CAE optimizations. In this context, the potentialities of TO and SO can be enhanced by the possibility of introducing continuous reinforcing fibers in plastic components realized through FDM such as MT machine. In fact, while remaining characterized by the low weight typical of polymers, the resulting components show mechanical properties comparable to those of high-performance metallic materials like aluminum alloys. Moreover, the proper arrangement of the fibers within the layers makes it possible to have components with better behavior. Orthotropic materials can be realized with a wide range of mechanical properties [164]. As an example, considering a lamina in which the fibers are positioned along the major direction on the neutral axis, a high resistance in the tension/compression direction and a very low flexural resistance are achieved. In contrast, by moving the fibers away from the neutral axis, the flexural resistance is also increased. Additionally, by considering the orientation of the fibers, the mechanical behavior in the other directions can be defined as well [16].

Automated production machines consist of mechanisms that are subjected to an input periodic motion trajectory and are mainly loaded by inertial actions. By adding properly designed elastic

elements in these mechanisms, the required actuation torque/force can be reduced. In particular, CJ [165] like flexible laminates can be adopted and sized to introduce an elastic component in the mechanism which put it in “resonance” with the input motion trajectory so as to reduce the required motor effort. In addition to modify the mechanism dynamic mechanical characteristic, CJ offer several advantages [166] with respect to the traditional kinematic pairs, including lightness, backlash-free operation and ease of manufacturing and assembling, which convey motion precision and low-cost production [167]. Their adoption for dynamic applications and repetitive motions is mainly limited by fatigue resistance and reduced deflection ranges.

This chapter investigates the potentialities of MT manufactured continuous fiber reinforced nylon (MT-CFRN) components, in combination with TO and size-optimized CJ, for the realization of mechanisms subjected to predominant inertial loads and compares the results with those obtainable with the standard and much more widespread MST. In particular, this section addresses the redesign of the single degree-of-freedom (DOF) position-controlled Stephenson six-bar planar linkage as depicted in 5.1, which is commonly used in automated machines as a pusher mechanism. Redesign is conducted with the simultaneous objectives of reducing motor torque requirements and maintaining high motion precision. This is achieved by a new design approach which is aimed at finding the optimal geometry of the links that minimizes the Root Mean Square (RMS) value of the motor torque while also maximizing the stiffness-to-weight ratio of the mechanism.

5.2 The Original Mechanism and the New Design Procedures

The schematic of the position-controlled pusher mechanism considered here in this work is shown in Fig.5.2. It consists of a slider-crank linkage and a parallelogram four-bar linkage (see Fig.5.2 links 3-6). Link 6 is the frame of the overall system. An electric motor (The input position, crank “link 1”) is the input of the whole system. Link 2 (the rod) connects the crank to link 3 (namely, the output of the pusher mechanism (the slider), which translates along a circular trajectory due to the constraints imposed by links 4 and 5). All connections between the links are made via bearings (ball/needle) that are placed at points A-D, O_1 , O_2 and O_3 . To describe the motion of the entire mechanism, a Cartesian reference system is fixed to the frame, featuring: the x-axis passing through points O_2 and O_3 , y-axis normal to the x-axis and passing through point O_1 , z-axis chosen according to the right-hand rule. α refers to the angular position of the crank with respect to the x-axis. Table 5.1 illustrates the

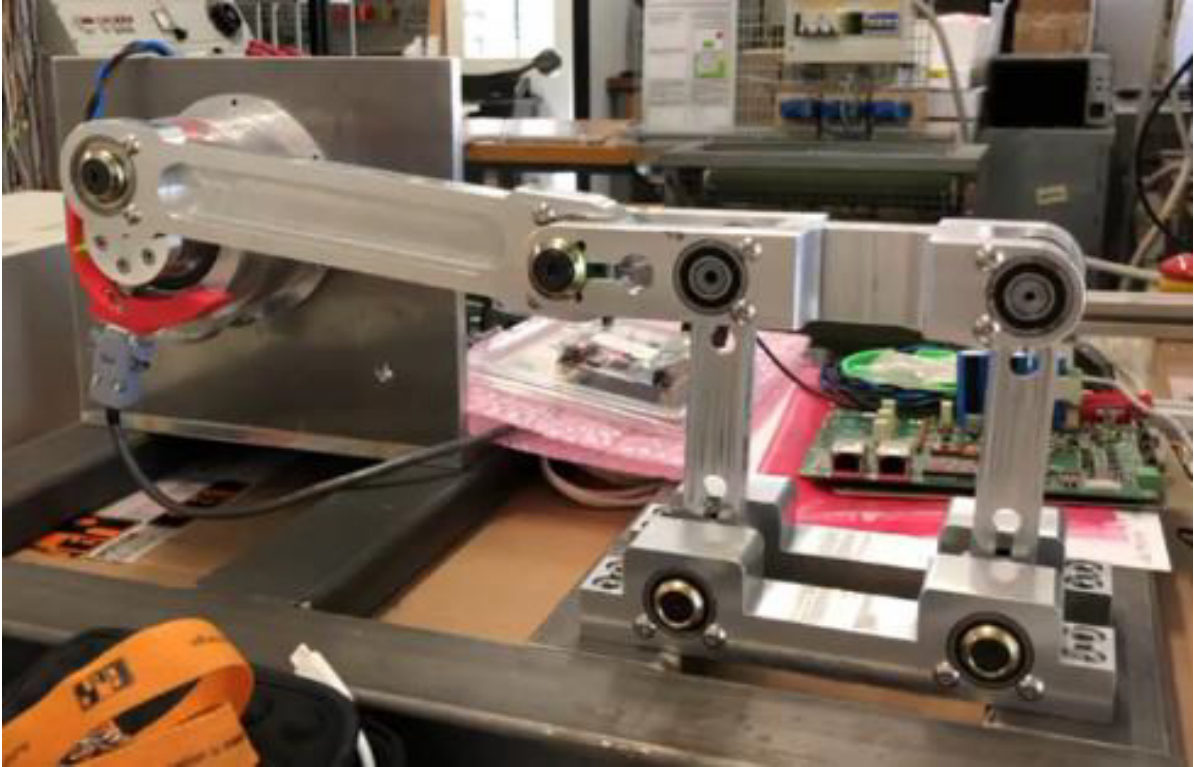


Figure 5.1: Stephenson six-bar planar linkage

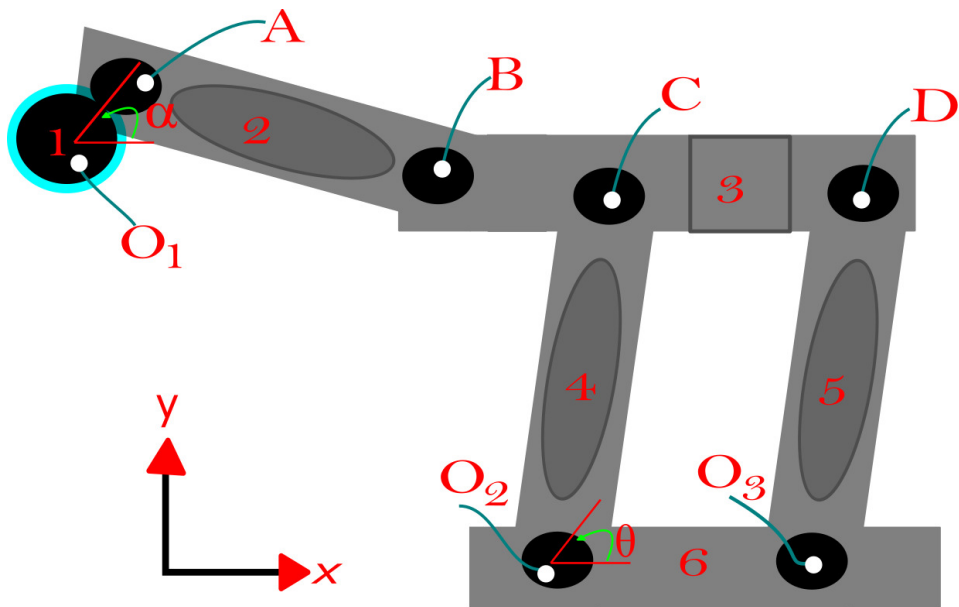


Figure 5.2: Schematic of original pusher mechanism

Table 5.1: Mechanism dimensions

l_1	$ O_1A $	30
l_2	$ AB $	230
l_3	$ O_2C $	170
l_4	$ BD $	120
l_5	$ CD = O_2O_3 $	110
O_1	$[0, 116.1895, 0]$	
O_2	$[290, 0, 0]$	

dimensions of the links. For a full rotation of the crank, the slider performs a 60 mm translation along the x -direction and a 3.8105 mm translation along the y -direction.

All links/elements of the original pusher mechanism as shown in Figs. 5.1 and 5.2 have been produced with MST. The material used was aluminum alloy 7000 series. During nominal operating conditions, the motor is requested to provide a peak torque of $T_{m,peak} = 2.19\text{Nm}$ and an RMS torque of $T_{m,peak} = 1.21\text{ Nm}$ over a full cycle. In order to reduce the motor torque requirements without losing rigidity and motion precision, this thesis develops a new design as illustrated in Fig. 5.3. In particular, Fig. 5.3a shows the original pusher mechanism, and Fig. 5.3b highlights how most of the parts are replaced by CJ. The following procedures are used to obtain the new proposed design:

- Utilizing FDM printing, in particular MT to produce the majority of the parts of the mechanism.
- Replacing the majority of rigid links and traditional kinematic pairs with CJ (mainly, flexible MT laminates).
- Reducing the mass of the bulky and stiff parts of the mechanism via TO.
- Redesigning the CJ via SO to make the mechanism operating under a “resonating” condition, enabling the bidirectional transfer between link kinetic energy and CJ elastic energy while involving the minimum power flow from/to the motor.

5.2.1 Mechanism Fabrication by MT

As stated earlier, the MT printer commercialized by MarkForged[®] has been used to produce the proposed mechanism. MT realizes CFRT parts by depositing continuous fibers on a polymeric matrix made of the proprietary material “white nylon or onyx that consists of nylon filled with chopped carbon fibers” (whose mechanical properties are shown in Table 3.4). The following continuous fibers

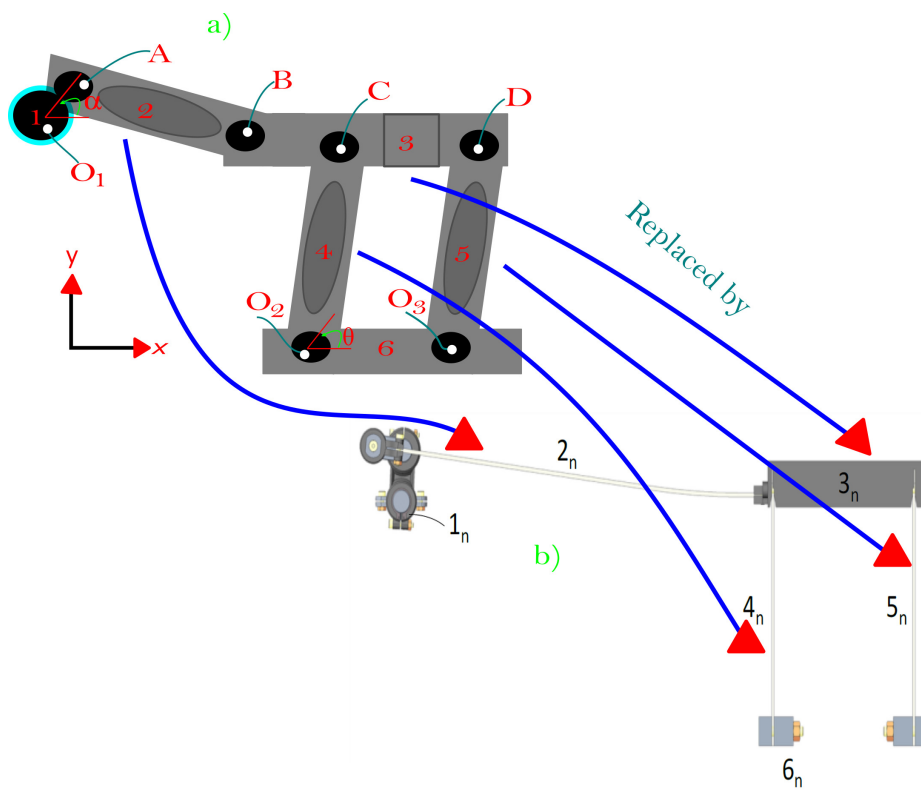


Figure 5.3: a) Schematic of original pusher mechanism, b) novel mechanism proposed

can be used to print CFRT parts: carbon fiber, Kevlar, fiberglass and high-strength high-temperature fiberglass. Among them, carbon fiber has the highest strength so that carbon-fiber-reinforced-onyx (CFRO) presents mechanical characteristics along some directions that are comparable to those of high-performance metallic materials, like aluminum alloys, thus perfectly fitting automated machinery applications.

5.2.2 Substitution of Links and Kinematic Pairs with CJ

As depicted in Fig. 5.3, bearings employed in the original mechanism B, C, O_2 and O_3 are replaced by CJ. Hence links 2, 4 and 5 are replaced completely with the new flexible MT laminates with suitably design stiffness. In particular, fibers are deposited in each layer along the y -axis, with the tray plane of the printer being normal to the z -axis so that the proper flexural stiffness around the z -axis is designed and a much higher stiffness around the x -axis is obtained. High flexural stiffness along the y -axis direction is guaranteed by the overall rearrangement of the three flexible MT laminates within the mechanism.

5.2.3 Size Optimization of the Flexible MT Laminates

The Pseudo-Rigid-Body (PRB) model is employed for the analysis [168]. Hence, a Fixed-Guided (FG) model is utilized for links 4 and 5, whereas a Fixed-Pin (FP) model is adopted for link 2. The resulting PRB model is reported in Fig. 5.4. In the model rigid links are connected to each other through virtual revolute joints with torsional springs in parallel. Torsional spring constants are: k_1 for the connections of links $G_{4,n}$ and $G_{5,n}$ with links $G_{3,n}$ and $G_{2,n}$; k_2 for the connection of link $G_{2,n}$ with link $G_{3,n}$. The kinematic equivalence of the new mechanism with the original one (MST manufactured) is guaranteed by matching the virtual revolute joints of the PRB model shown in Fig. 5.4 with the real ones of Fig. 5.2. This provides the MT laminate of the new mechanism to be longer than the actual length of the respective links. For the optimization section, the thickness of each laminate are between 1 and 7 mm (namely, s_2 for link 2_n and s_3 for links 4_n and 5_n) is considered as the only changing parameter (between 1 and 7 mm). The width of the laminas is fixed and chosen as $b = 20$ mm. Based on the PRB model theory, the expression of the torsional spring stiffnesses is given as in Eqs. 5.1 [169]:

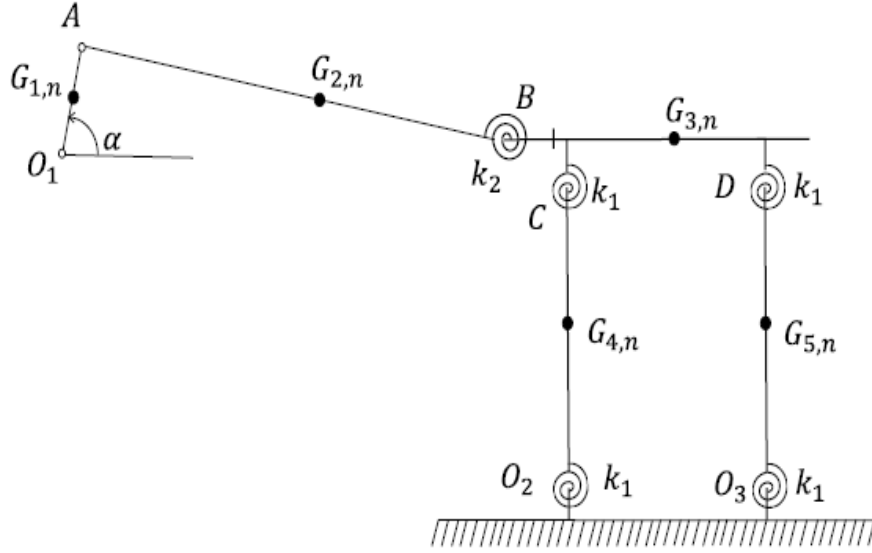


Figure 5.4: Kinematic equivalent mechanism

$$\begin{aligned}
 k_1 &= \gamma K_{\Theta} \frac{E_{pz} I_2}{I_{2,n}} \\
 k_2 &= 2\gamma K_{\Theta} \frac{E_{pz} I_3}{I_{3,n}}
 \end{aligned}
 \tag{5.1}$$

where, $l_{2,n}$ and $l_{3,n}$ respectively refer to the lengths of laminates number 2_n , and number 4_n and 5_n . Instead, $I_2 = \frac{bs_2^3}{12}$ and $I_3 = \frac{bs_3^3}{12}$ respectively describe the area moment of inertia of laminates 2_n , and number 4_n and 5_n (see Fig. 5.3). γ and K_{Θ} are both constants that depend on the force direction.

In order to prevent failure of the mechanism, the compression force F_2 acting on the laminate 2_n has to be lower than the Euler's critical load given by the expression below:

$$F_{2,max} \leq \pi^2 \frac{E_{pz} I_2}{l_0^2}
 \tag{5.2}$$

in which, $l_0 = 0.7l$ and l is the effective length for the fixed-pin beam " $l_{2,n}$ ". Hence, the stiffness of laminates 4_n and 5_n should be lower than the stiffness of laminate 2_n . Such limitation is marked as a relationship between the design parameters s_2 and s_3 , which is introduced to the optimization. The functional to be minimized for the optimization consists in the RMS value of the motor torque, TRMS,

over a full motion cycle of the mechanism. By applying Lagrange approach the design parameters s_2 and s_3 are obtained. For the computation of the kinetic energy, the following equations are used:

$$J_i = \pi^2 \frac{1}{12} \rho_{CFRO} s_i l_{i,n} b (l_{i,n}^2 + b^2) \quad (5.3)$$

$$m_i = \rho_{CFRO} s_i l_{i,n} b \quad (5.4)$$

where, mass is described by m_i and inertia defined as J_i . The i -index refers to i_{th} -laminate and it is changed as a function of s_i .

5.2.4 Mechanical Dissipation Experimental Analysis

In the model of motor torque, the inherent viscous damping due to the deformation of the laminate together with the bearing friction is ignored. In accordance to the experimental investigation, it can be noted that the laminate damping coefficient magnitude has the same order as the one of the bearings in the original mechanism and its contribution on the motor torque is expected to be low with respect to the inertial and elastic ones. However, if such dissipations have to be accounted, torsional dampers with appropriate damping coefficients can be added in parallel to each torsional spring of the PRB model. Therefore, in order to analyze the system which is represented by (3_n) , (4_n) , (5_n) and (6_n) (referred as to the two-rocker-slider system), a test rig (see Fig. 5.5) has been developed. Its scope is twofold: verify the analytical design procedure and estimate the damping ratio ζ of the two-rocker-slider system. An equivalent one DOF mass-spring-damper model has been applied to obtain ζ . The stiffness and damper are given by the rockers. Whereas the mass is equal to the slider. Consequently, the thickness of laminates (4_n) and (5_n) is designed so that the resonance frequency of the system coincides with 10 Hz, namely the nominal operating frequency of the entire mechanism. In the rig, laminas (4_n) and (5_n) are fixed to the frame to one end and fixed to a mobile platform (7) that simulates the slider to the other one. The mass of the platform and the test parts attached have the same mass of the link 3_n which is optimized via TO. In the tests, the platform is moved to a known value and then released. Motion of the two-rocker-slider system is acquired with the sensors presented in Fig. 5.5 and then the damping ratio is computed.

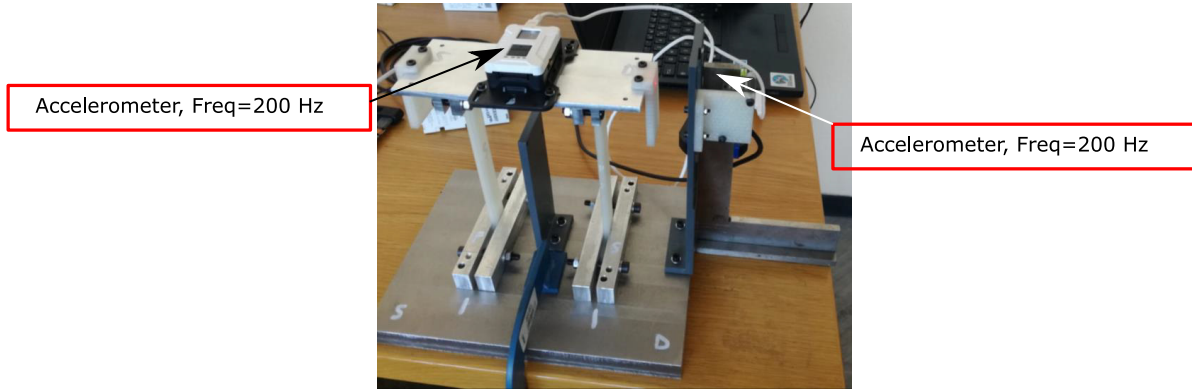


Figure 5.5: Test platform for the damping measurement

Table 5.2: Material properties used and LSS

Component	Original	Optimized (%)	Reduction (%)
Crank	0.0759	0.0235	70
Rod	0.3220	0.0346	90
Slider	0.4010	0.0906	75
Rocker	0.0765	0.0104	85

5.3 Results

The proposed designing approach mentioned earlier can be considered to be successful and promising in terms of weight reduction. The new slider results to be 0.09 kg which means about 75% mass reduction. CJ design provides better mass reduction. Table 5.2 shows comparison of the weight of the links of the redesigned mechanism and those of the original traditional mechanism: reduction values between 70% and 90% are obtained.

The mass is reduced thanks to the following two main keys:

- The density of the printed CFRN material is less than half the density of the aluminum alloy AA7075.
- The new proposed mechanism does not need bearings. In this case, the slider is lightened by the removal of twelve bearings (480g).

On the other hand, based on the experimental tests performed with the set-up of Fig.5.5, a damping ratio ζ of 0.04 and a natural frequency of 10.7 Hz of the two-rocker-slider system are obtained. Fig. 5.6 shows the comparison between the displacement of the platform considering the analytical model

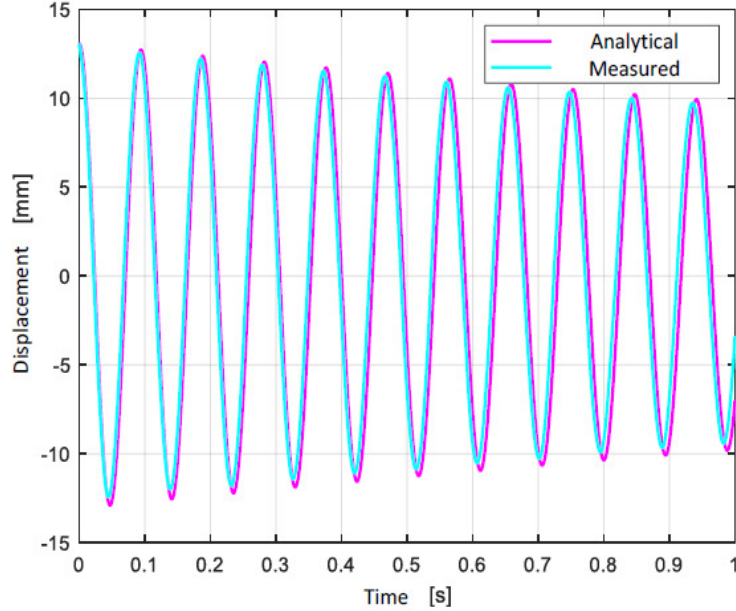


Figure 5.6: Kinematic equivalent mechanism

(in which the damping ratio is implemented) and the displacement measured from the test rig.

Finally, Fig.5.7 shows the RMS motor torque as a function of both thickness of the rockers named as s_2 and s_3 . It can be noted that the optimal value of the motor torque (denoted by $T_{m,rms,opt}$) is 0.05 Nm and occurs for 2.05 mm and 1.07 mm for $s_{2,opt}$ and $s_{3,opt}$, respectively. The maximum motor torque value over the cycle time is 0.11 Nm. This means that, as compared to the original mechanism, the peak motor torque was reduced to about 95%, while a 96% reduction of the RMS motor torque is obtained.

5.4 Conclusion

In this chapter, a novel design approach employing CJ, TO and SO is presented and successfully applied to a Stephenson six bar link age which is used as a pusher mechanism in automated machinery. The results show a huge weight reduction of about 75% as opposed to the original mechanism. This is due to the low density offered by laminate (most of the layers are produced in plastic as well as feature small thickness. Moreover, the geometry and set up of the proposed compliant mechanism are both very simple and straightforward. Peak value of the required motor torque is lowered to

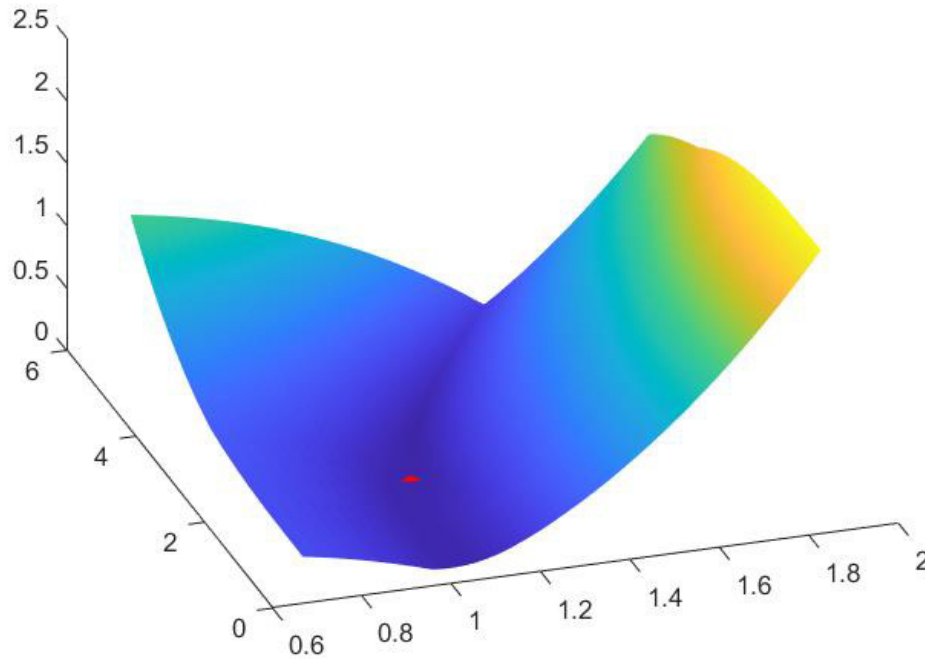


Figure 5.7: RMS motor torque surface

one tenth. However, the major contribution is due to the introduction of elasticity through CJ. Indeed, the appropriate sizing of CJ (flexible laminates in this case) enables to put the mechanism in a “resonating” condition. On the other hand, compared to the traditional techniques such as the CNC machining and casting processes, 3D-FDM is more time-consuming during both design and manufacturing stages which makes it not suitable for high volume production. Further, the design requires several steps to be completed, which are rather dependent on the designer expertise, especially the TO that requires surface redesign procedures.

Chapter 6

Future Work Directions

The stated overarching aim of this thesis was to present several work in the three dimensional (3D) printing of the smart structures field. In which we identified the proper position of the reinforcements filaments within the 3D printed structure, in particular, MarkTwo[®] (MT) printed components and provided a selective compliance for flexure straight beam applications. Then we have used the advanced capabilities of Carrera Unified Formulation (CUF) 1D beam models to model the multicomponent 3D printed structures (MC3DPS) by implementing a component wise (CW) model to divide the MT structure cross section into various sub domains to include all the details within each component with a very low computational cost but yet providing accurate results. Moreover, we have leverged the CUF-CW tool to predict the material properties of the structures based on various infill densities instead of relying only on many experimental work and analysis the multi body structures via linking static condensation method within the CW-CUF platform. Finally, we integrated FDM-MT, topology optimization (TO) , and compliant joints design (CJD) to optimize automated machinery mechanisms subjected to inertial loads. Throughout the developed work, we encountered many interesting questions that are worthy of future exploration and which further improve the current numerical model or lead to the development of a new analytical model, which to be widely adopted in the future by the research community. The details of these questions is provided in the following sections.

6.1 Experimental Characterization

In the proposed experimental analysis of straight beam flexures (SBF) realized in carbon fiber reinforced Nylon White material with the fused filament fabrication machine MT commercialized by MarkForged[®] we outlined the dependency of the tensile and flexural responses of the considered SBF on the arrangement of the continuous carbon fibers within the polymeric matrix. Generally, the results revealed that for the same geometry and amount of material, SBF mechanical characteristics can be tuned by simply changing the disposition of the fibers within the matrix. This feature perfectly fits the needs of compliant mechanisms, which require flexible elements with selective compliance that has

to be selectable based on the application. But we ignore the usage of different thicknesses of the layers, which could have effect on the behaviour of SBF, as well as the usage of different reinforcement, and/or polymer material. In addition , we did not characterize the samples at a micro-scale level. *Future work:* What is the effect of using different thickness of polymer material? How does it vary across the printed specimen? What is the effect of using Kevlar, glass fiber as reinforcement ? Will the micro-scale experimental investigation be able to capture the void and provide us with more details on the voids of the printed structures? Can different techniques including chemical, heat, ultrasound be used to reduce defect and improve printed parts ? How is it possible to efficiently implement them?

6.2 Numerical Analysis

Throughout the thesis, we provided a detailed insight into special modeling techniques for MT parts including a novel preprocessing platform within the CUF which easily describes the modeling parameters and discretization in a precise and time efficient way that accounts all the details of the MT printed components. We used the advanced capabilities of CUF 1D beam models to model the MC3DPS. We have done this by using LE formulation to implement CW model to divide the MT cross section into various sub domains; for instance, we included floor and roof, and infill as independent components with specific material and geometrical features. However, we ignored including voids, defects, and cracks within the framework of our model. Moreover, we always assumed density, and material properties of different region. *Future work:* How to extend the current model to account possible voids at a micro-scale level and/or via a multi-scale modeling tool? What are the material properties based on various wall numbers? And how do they vary across the printed specimen? How could we extend the model to include material non-linearity, and how will it make the model more complicated ? Since our aim is to analyse and design multibody parts, and in particular flexure based compliant mechanisms, will it be possible to develop an analytical solution with minimal computational cost ? As mentioned earlier, 3DP have matured and shown potentiality to be adopted for end-part production instead of being a prototyping tool [15]. 3D printing process has various process parameters including infill densities, number of walls, materials, etc which influence the part quality and properties. Therefore, it is necessary to have a detailed understanding of the relationship between such parameters and part quality, density and so on; this requires interdisciplinary understanding such as solid liquid, interaction, fluid dynamics, grain growth development and thermal mechanical interaction. That is to fully

understanding the influence, interdisciplinary is required. Given these complexities, it may be elusive if not possible to establish a model which accounts all 3D process precisely parameters and accurately via physics based numerical simulations/experimental works. In this context, machine learning (ML) data driven models may be adopted as an instrumental tool as optimization of 3D printing process can be achieved with partial or incomplete data. Therefore, will it be possible to present a data driven model which uses the ML especially in the area of predicting the mechanical behavior ?

6.3 Compliant Joint Application

Throughout the industrial application chapter, we analyzed the potentiality of MT in combination with topology optimization (TO) and compliant joint (CJ) design for the realization of automated machinery mechanisms subjected to inertial loads in which a pusher mechanism is considered. The novel CJ is presented and successfully applied to a Stephenson six bar link age. The results have shown a huge weight reduction of about 75% opposed to the original mechanism. Nonetheless, opposed to the traditional techniques processing time such as CNC machining and casting, the development process proposed here is more time-consuming during both design and manufacturing steps. In fact, the design requires several steps to be completed, which are rather dependent on the designer expertise, especially the TO and surface redesign procedures. The manufacturing phase takes longer than traditional CNC machining and casting processes making the FDM not suitable for high volume production. *Future work:* Will it be possible to reduce such time via mass production 3D printing? Will it be possible to apply the proposed development process in other end user applications ?

References

- [1] J. Z. Gul, M. Sajid, M. M. Rehman, G. U. Siddiqui, I. Shah, K.-H. Kim, J.-W. Lee, and K. H. Choi, “3d printing for soft robotics—a review,” *Science and technology of advanced materials*, vol. 19, no. 1, pp. 243–262, 2018.
- [2] G. Arena, R. MJ Groh, A. Brinkmeyer, R. Theunissen, P. M. Weaver, and A. Pirrera, “Adaptive compliant structures for flow regulation,” *Proceedings of the Royal Society A: Mathematical, Physical and Engineering Sciences*, vol. 473, no. 2204, p. 20170334, 2017.
- [3] S. Daynes, K. Potter, and P. Weaver, “Bistable prestressed buckled laminates,” *Composites Science and Technology*, vol. 68, no. 15-16, pp. 3431–3437, 2008.
- [4] A. Brinkmeyer, A. Pirrera, M. Santer, and P. Weaver, “Pseudo-bistable pre-stressed morphing composite panels,” *International Journal of Solids and Structures*, vol. 50, no. 7-8, pp. 1033–1043, 2013.
- [5] E. Eckstein, A. Pirrera, and P. Weaver, “Multi-mode morphing using initially curved composite plates,” *Composite Structures*, vol. 109, pp. 240–245, 2014.
- [6] A. Pirrera, D. Avitabile, and P. Weaver, “Bistable plates for morphing structures: a refined analytical approach with high-order polynomials,” *International Journal of Solids and Structures*, vol. 47, no. 25-26, pp. 3412–3425, 2010.
- [7] P. M. Reis, “A perspective on the revival of structural (in) stability with novel opportunities for function: from buckliophobia to buckliophilia,” *Journal of Applied Mechanics*, vol. 82, no. 11, p. 111001, 2015.
- [8] G. D. Goh, S. Agarwala, G. Goh, V. Dikshit, S. L. Sing, and W. Y. Yeong, “Additive manufacturing in unmanned aerial vehicles (uavs): Challenges and potential,” *Aerospace Science and Technology*, vol. 63, pp. 140–151, 2017.

- [9] P. Parandoush and D. Lin, "A review on additive manufacturing of polymer-fiber composites," *Composite Structures*, vol. 182, pp. 36–53, 2017.
- [10] S. V. Murphy and A. Atala, "3d bioprinting of tissues and organs," *Nature biotechnology*, vol. 32, no. 8, pp. 773–785, 2014.
- [11] E. Kroll and D. Artzi, "Enhancing aerospace engineering students' learning with 3d printing wind-tunnel models," *Rapid Prototyping Journal*, 2011.
- [12] K. V. Wong and A. Hernandez, "A review of additive manufacturing," *International scholarly research notices*, vol. 2012, 2012.
- [13] X. Wang, M. Jiang, Z. Zhou, J. Gou, and D. Hui, "3d printing of polymer matrix composites: A review and prospective," *Composites Part B: Engineering*, vol. 110, pp. 442–458, 2017.
- [14] A. Turon Travesa *et al.*, *Simulation of delamination in composites under quasi-static and fatigue loading using cohesive zone models*. Universitat de Girona, 2006.
- [15] G. D. Goh, S. L. Sing, and W. Y. Yeong, "A review on machine learning in 3d printing: applications, potential, and challenges," *Artificial Intelligence Review*, vol. 54, no. 1, pp. 63–94, 2021.
- [16] M. Refat, L. Luzi, L. Agostini, R. Pucci, G. Berselli, and R. Vertechy, "Fused filament fabrication of continuous fiber-reinforced thermoplastics for compliant mechanisms," in *Smart Materials, Adaptive Structures and Intelligent Systems*, vol. 85499. American Society of Mechanical Engineers, 2021, p. V001T07A015.
- [17] I. Gibson, D. W. Rosen, B. Stucker, M. Khorasani, D. Rosen, B. Stucker, and M. Khorasani, *Additive manufacturing technologies*. Springer, 2021, vol. 17.
- [18] M. Caminero, J. Chacón, I. García-Moreno, and J. Reverte, "Interlaminar bonding performance of 3d printed continuous fibre reinforced thermoplastic composites using fused deposition modelling," *Polymer Testing*, vol. 68, pp. 415–423, 2018.
- [19] J. Chacón, M. A. Caminero, E. García-Plaza, and P. J. Núñez, "Additive manufacturing of pla structures using fused deposition modelling: Effect of process parameters on mechanical properties and their optimal selection," *Materials & Design*, vol. 124, pp. 143–157, 2017.

- [20] P. K. Penumakala, J. Santo, and A. Thomas, "A critical review on the fused deposition modeling of thermoplastic polymer composites," *Composites Part B: Engineering*, vol. 201, p. 108336, 2020.
- [21] B. N. Turner, R. Strong, and S. A. Gold, "A review of melt extrusion additive manufacturing processes: I. process design and modeling," *Rapid Prototyping Journal*, 2014.
- [22] B. N. Turner and S. A. Gold, "A review of melt extrusion additive manufacturing processes: II. materials, dimensional accuracy, and surface roughness," *Rapid Prototyping Journal*, 2015.
- [23] I. G. Ian Gibson, "Additive manufacturing technologies 3d printing, rapid prototyping, and direct digital manufacturing," 2015.
- [24] I. Gibson, D. Rosen, and B. Stucker, "Introduction and basic principles. in additive manufacturing—3d printing, rapid prototyping, and direct digital manufacturing," 2015.
- [25] A. C. F. on Additive Manufacturing Technologies and A. C. F. on Additive Manufacturing Technologies. Subcommittee F42. 91 on Terminology, *Standard terminology for additive manufacturing technologies*. ASTM International, 2012.
- [26] C. Hull, "U. s. patent no. 4, 575, 330," 1986.
- [27] B. Berman, "3-d printing: The new industrial revolution," *Business horizons*, vol. 55, no. 2, pp. 155–162, 2012.
- [28] H. Bikas, P. Stavropoulos, and G. Chryssolouris, "Additive manufacturing methods and modelling approaches: a critical review," *The International Journal of Advanced Manufacturing Technology*, vol. 83, no. 1-4, pp. 389–405, 2016.
- [29] H.-J. L. Dirk, C. Ward, and K. D. Potter, "The engineering aspects of automated prepreg layup: History, present and future," *Composites Part B: Engineering*, vol. 43, no. 3, pp. 997–1009, 2012.
- [30] D. Wagg, I. Bond, P. Weaver, and M. Friswell, *Adaptive structures: engineering applications*. John Wiley & Sons, 2008.

- [31] S. Daynes, P. Weaver, and K. Potter, “Aeroelastic study of bistable composite airfoils,” *Journal of Aircraft*, vol. 46, no. 6, pp. 2169–2174, 2009.
- [32] S. Daynes, P. Weaver, and J. Trevarthen, “A morphing composite air inlet with multiple stable shapes,” *Journal of Intelligent Material Systems and Structures*, vol. 22, no. 9, pp. 961–973, 2011.
- [33] M. Santer, “Self-actuated snap back of viscoelastic pulsing structures,” *International Journal of Solids and Structures*, vol. 47, no. 24, pp. 3263–3271, 2010.
- [34] K. Williams, G. Chiu, and R. Bernhard, “Adaptive-passive absorbers using shape-memory alloys,” *Journal of Sound and Vibration*, vol. 249, no. 5, pp. 835–848, 2002.
- [35] A. Brinkmeyer, “Time-dependent bistable morphing structures,” Ph.D. dissertation, University of Bristol, 2014.
- [36] I. K. Kuder, A. F. Arrieta, W. E. Raither, and P. Ermanni, “Variable stiffness material and structural concepts for morphing applications,” *Progress in Aerospace Sciences*, vol. 63, pp. 33–55, 2013.
- [37] F. T. Calkins and J. H. Mabe, “Shape memory alloy based morphing aerostructures,” *Journal of Mechanical Design*, vol. 132, no. 11, p. 111012, 2010.
- [38] G. A. Thuwis, M. M. Abdalla, and Z. Gürdal, “Optimization of a variable-stiffness skin for morphing high-lift devices,” *Smart materials and structures*, vol. 19, no. 12, p. 124010, 2010.
- [39] O. Tabata, S. Konishi, P. Cusin, Y. Ito, F. Kawai, S. Hirai, and S. Kawamura, “Micro fabricated tunable bending stiffness devices,” *Sensors and Actuators A: Physical*, vol. 89, no. 1-2, pp. 119–123, 2001.
- [40] M. H. Shirk, T. J. Hertz, and T. A. Weisshaar, “Aeroelastic tailoring-theory, practice, and promise,” *Journal of Aircraft*, vol. 23, no. 1, pp. 6–18, 1986.
- [41] L. L. Howell, S. P. Magleby, and B. M. Olsen, *Handbook of compliant mechanisms*. John Wiley & Sons, 2013.
- [42] L. L. Howell, *Compliant mechanisms*. John Wiley & Sons, 2001.

- [43] S. Vogel, "Cats' paws and catapults, 1998."
- [44] H. Troeger, "Considerations in the application of flexural pivots," *Automatic Control*, vol. 17, no. 4, pp. 41–46, 1962.
- [45] L. L. Howell and A. Midha, "A method for the design of compliant mechanisms with small-length flexural pivots," *Journal of mechanical design*, vol. 116, no. 1, pp. 280–290, 1994.
- [46] N. M. Sevak and C. McLarnan, "Optimal synthesis of flexible link mechanisms with large static deflections," *Journal of Engineering for Industry*, vol. 97, no. 2, pp. 520–526, 1975.
- [47] S. Zelenika and F. De Bona, "Analytical and experimental characterisation of high-precision flexural pivots subjected to lateral loads," *Precision Engineering*, vol. 26, no. 4, pp. 381–388, 2002.
- [48] N. D. Mankame and G. Ananthasuresh, "Topology synthesis of electrothermal compliant mechanisms using line elements," *Structural and multidisciplinary optimization*, vol. 26, no. 3-4, pp. 209–218, 2004.
- [49] G. Bögelsack, "Nachgiebige mechanismen in miniaturisierten bewegungssystemen," in *Proceedings of the 9th World Congress on Theory of Mach. and Mech*, 1995.
- [50] B. Caulfield, P. McHugh, and S. Lohfeld, "Dependence of mechanical properties of polyamide components on build parameters in the sls process," *Journal of Materials Processing Technology*, vol. 182, no. 1-3, pp. 477–488, 2007.
- [51] C. R. Garcia, J. Correa, D. Espalin, J. H. Barton, R. C. Rumpf, R. Wicker, and V. Gonzalez, "3d printing of anisotropic metamaterials," *Progress In Electromagnetics Research*, vol. 34, pp. 75–82, 2012.
- [52] B. Tymrak, M. Kreiger, and J. M. Pearce, "Mechanical properties of components fabricated with open-source 3-d printers under realistic environmental conditions," *Materials & Design*, vol. 58, pp. 242–246, 2014.
- [53] Q. Sun, G. Rizvi, C. Bellehumeur, and P. Gu, "Effect of processing conditions on the bonding quality of fdm polymer filaments," *Rapid Prototyping Journal*, vol. 14, no. 2, pp. 72–80, 2008.

- [54] P. Tran, T. D. Ngo, A. Ghazlan, and D. Hui, "Bimaterial 3d printing and numerical analysis of bio-inspired composite structures under in-plane and transverse loadings," *Composites Part B: Engineering*, vol. 108, pp. 210–223, 2017.
- [55] R. Melnikova, A. Ehrmann, and K. Finsterbusch, "3d printing of textile-based structures by fused deposition modelling (fdm) with different polymer materials," in *IOP Conference Series: Materials Science and Engineering*, vol. 62, no. 1. IOP Publishing, 2014, p. 012018.
- [56] H. Gu, C. Ma, J. Gu, J. Guo, X. Yan, J. Huang, Q. Zhang, and Z. Guo, "An overview of multi-functional epoxy nanocomposites," *Journal of Materials Chemistry C*, vol. 4, no. 25, pp. 5890–5906, 2016.
- [57] J. Gu, X. Yang, Z. Lv, N. Li, C. Liang, and Q. Zhang, "Functionalized graphite nanoplatelets/epoxy resin nanocomposites with high thermal conductivity," *International Journal of Heat and Mass Transfer*, vol. 92, pp. 15–22, 2016.
- [58] J. Dou, Q. Zhang, M. Ma, and J. Gu, "Fast fabrication of epoxy-functionalized magnetic polymer core-shell microspheres using glycidyl methacrylate as monomer via photo-initiated miniemulsion polymerization," *Journal of Magnetism and Magnetic Materials*, vol. 324, no. 19, pp. 3078–3082, 2012.
- [59] J. R. C. Dizon, A. H. Espera Jr, Q. Chen, and R. C. Advincula, "Mechanical characterization of 3d-printed polymers," *Additive Manufacturing*, vol. 20, pp. 44–67, 2018.
- [60] I. ASTM, "Astm52900-15," *Standard Terminology for Additive Manufacturing—General Principles—Terminology*, ASTM International, West Conshohocken, PA, 2015.
- [61] S. M. Malhotra SK, Goda K, "Part one introduction to polymer composites. in: Polymer composites," Wiley-VCH; 2012, Tech. Rep., 2012.
- [62] L. Blok, M. Longana, H. Yu, and B. Woods, "An investigation into 3d printing of fibre reinforced thermoplastic composites," *Additive Manufacturing*, vol. 22, pp. 176–186, 2018.
- [63] S. H. Huang, P. Liu, A. Mokasdar, and L. Hou, "Additive manufacturing and its societal impact: a literature review," *The International Journal of Advanced Manufacturing Technology*, vol. 67, no. 5-8, pp. 1191–1203, 2013.

- [64] F. P. Rad, R. Vertechy, G. Berselli, and V. Parenti-Castelli, "Analytical compliance analysis and finite element verification of spherical flexure hinges for spatial compliant mechanisms," *Mechanism and Machine Theory*, vol. 101, pp. 168–180, 2016.
- [65] Y. Moon and J. Choi, "A compliant parallel mechanism for needle intervention," in *2013 35th Annual International Conference of the IEEE Engineering in Medicine and Biology Society (EMBC)*. IEEE, 2013, pp. 4875–4878.
- [66] M. B. Hong and Y.-H. Jo, "Design and evaluation of 2-dof compliant forceps with force-sensing capability for minimally invasive robot surgery," *IEEE Transactions on Robotics*, vol. 28, no. 4, pp. 932–941, 2012.
- [67] N. P. Belfiore, M. Balucani, R. Crescenzi, and M. Verotti, "Performance analysis of compliant mems parallel robots through pseudo-rigid-body model synthesis," in *Engineering Systems Design and Analysis*, vol. 44861. American Society of Mechanical Engineers, 2012, pp. 329–334.
- [68] A. Saucedo-Carvajal, H. Kennedy-Cabrera, J. Hernández-Torres, A. Herrera-May, and J. Mireles Jr, "Compliant mems mechanism to extend resolution in fourier transform spectroscopy," in *Micromachining and Microfabrication Process Technology XIX*, vol. 8973. SPIE, 2014, pp. 203–211.
- [69] Y. Tian, D. Zhang, and B. Shirinzadeh, "Dynamic modelling of a flexure-based mechanism for ultra-precision grinding operation," *Precision Engineering*, vol. 35, no. 4, pp. 554–565, 2011.
- [70] S. Polit and J. Dong, "Development of a high-bandwidth xy nanopositioning stage for high-rate micro-/nanomanufacturing," *IEEE/ASME Transactions on mechatronics*, vol. 16, no. 4, pp. 724–733, 2010.
- [71] L. Weisbord and J. Paros, "How to design flexure hinges," *Machine Design*, vol. 27, no. 3, pp. 151–157, 1965.
- [72] N. Lobontiu, J. S. Paine, E. Garcia, and M. Goldfarb, "Corner-filletted flexure hinges," *J. Mech. Des.*, vol. 123, no. 3, pp. 346–352, 2001.

- [73] Y. Tian, B. Shirinzadeh, D. Zhang, and Y. Zhong, “Three flexure hinges for compliant mechanism designs based on dimensionless graph analysis,” *Precision Engineering*, vol. 34, no. 1, pp. 92–100, 2010.
- [74] N. Lobontiu and M. Cullin, “In-plane elastic response of two-segment circular-axis symmetric notch flexure hinges: The right circular design,” *Precision Engineering*, vol. 37, no. 3, pp. 542–555, 2013.
- [75] F. P. Rad, G. Berselli, R. Vertechy, and V. P. Castelli, “Evaluating the spatial compliance of circularly curved-beam flexures,” in *Computational Kinematics*. Springer, 2014, pp. 377–386.
- [76] G. Berselli, F. P. Rad, R. Vertechy, and V. P. Castelli, “Comparative evaluation of straight and curved beam flexures for selectively compliant mechanisms,” in *2013 IEEE/ASME International Conference on Advanced Intelligent Mechatronics*. IEEE, 2013, pp. 1761–1766.
- [77] S. T. Smith, *Flexures: elements of elastic mechanisms*. Crc Press, 2000.
- [78] B. P. Trease, Y.-M. Moon, and S. Kota, “Design of large-displacement compliant joints,” 2005.
- [79] D. Farhadi Machekposhti, N. Tolou, and J. Herder, “The scope for a compliant homokinetic coupling based on review of compliant joints and rigid-body constant velocity universal joints,” in *International Design Engineering Technical Conferences and Computers and Information in Engineering Conference*, vol. 45035. American Society of Mechanical Engineers, 2012, pp. 379–392.
- [80] J. Hesselbach, J. Wrege, A. Raatz, and O. Becker, “Aspects on design of high precision parallel robots,” *Assembly Automation*, 2004.
- [81] G. Palmieri, M. Palpacelli, and M. Callegari, “Study of a fully compliant u-joint designed for minirobotics applications,” 2012.
- [82] J. O. Jacobsen, G. Chen, L. L. Howell, and S. P. Magleby, “Lamina emergent torsional (let) joint,” *Mechanism and Machine Theory*, vol. 44, no. 11, pp. 2098–2109, 2009.
- [83] K. Lussenburg, A. Sakes, and P. Breedveld, “Design of non-assembly mechanisms: A state-of-the-art review,” *Additive Manufacturing*, vol. 39, p. 101846, 2021. [Online]. Available: <https://www.sciencedirect.com/science/article/pii/S2214860421000117>

- [84] Y.-q. Yang, X.-b. Su, D. Wang, and Y.-h. Chen, “Rapid fabrication of metallic mechanism joints by selective laser melting,” *Proceedings of the Institution of Mechanical Engineers, Part B: Journal of Engineering Manufacture*, vol. 225, no. 12, pp. 2249–2256, 2011.
- [85] R. MacCurdy, R. Katzschmann, Y. Kim, and D. Rus, “Printable hydraulics: A method for fabricating robots by 3d co-printing solids and liquids,” in *2016 IEEE International Conference on Robotics and Automation (ICRA)*. IEEE, 2016, pp. 3878–3885.
- [86] B. N. Peele, T. J. Wallin, H. Zhao, and R. F. Shepherd, “3d printing antagonistic systems of artificial muscle using projection stereolithography,” *Bioinspiration & biomimetics*, vol. 10, no. 5, p. 055003, 2015.
- [87] Y. Wei, Y. Chen, Y. Yang, and Y. Li, “Novel design and 3-d printing of nonassembly controllable pneumatic robots,” *IEEE/ASME Transactions on Mechatronics*, vol. 21, no. 2, pp. 649–659, 2015.
- [88] F. Calignano, D. Manfredi, E. Ambrosio, S. Biamino, M. Pavese, and P. Fino, “Direct fabrication of joints based on direct metal laser sintering in aluminum and titanium alloys,” *Procedia CIRP*, vol. 21, pp. 129–132, 2014.
- [89] Y. Chen and J. Lu, “Minimise joint clearance in rapid fabrication of non-assembly mechanisms,” *International Journal of Computer Integrated Manufacturing*, vol. 24, no. 8, pp. 726–734, 2011.
- [90] X. Su, Y. Yang, D. Wang, and Y. Chen, “Digital assembly and direct fabrication of mechanism based on selective laser melting,” *Rapid Prototyping Journal*, 2013.
- [91] C. Mavroidis, K. J. DeLaurentis, J. Won, and M. Alam, “Fabrication of non-assembly mechanisms and robotic systems using rapid prototyping,” *J. Mech. Des.*, vol. 123, no. 4, pp. 516–524, 2001.
- [92] J. Cali, D. A. Calian, C. Amati, R. Kleinberger, A. Steed, J. Kautz, and T. Weyrich, “3d-printing of non-assembly, articulated models,” *ACM Transactions on Graphics (TOG)*, vol. 31, no. 6, pp. 1–8, 2012.
- [93] K. J. De Laurentis, F. F. Kong, and C. Mavroidis, “Procedure for rapid fabrication of non-assembly mechanisms with embedded components,” in *International Design Engineering Tech-*

- nical Conferences and Computers and Information in Engineering Conference*, vol. 36533. American Society of Mechanical Engineers, 2002, pp. 1239–1245.
- [94] J. S. Cuellar, G. Smit, D. Plettenburg, and A. Zadpoor, “Additive manufacturing of non-assembly mechanisms,” *Additive Manufacturing*, vol. 21, pp. 150–158, 2018.
- [95] M. W. Groenewegen, M. E. Aguirre, and J. L. Herder, “Design of a partially compliant, three-phalanx underactuated prosthetic finger,” in *International Design Engineering Technical Conferences and Computers and Information in Engineering Conference*, vol. 57120. American Society of Mechanical Engineers, 2015, p. V05AT08A040.
- [96] R. Mutlu, G. Alici, M. in het Panhuis, and G. Spinks, “Effect of flexure hinge type on a 3d printed fully compliant prosthetic finger,” in *2015 IEEE International Conference on Advanced Intelligent Mechatronics (AIM)*. IEEE, 2015, pp. 790–795.
- [97] S. Hill and S. Canfield, “An assessment of fused deposition modeling for the manufacturing of flexural pivots in an anthropomorphic robotic hand design,” in *International Design Engineering Technical Conferences and Computers and Information in Engineering Conference*, vol. 50169. American Society of Mechanical Engineers, 2016, p. V05BT07A066.
- [98] J. A. Mirth, “An examination of trispiral hinges suitable for use in abs-based rapid prototyping of compliant mechanisms,” in *International Design Engineering Technical Conferences and Computers and Information in Engineering Conference*, vol. 46360. American Society of Mechanical Engineers, 2014, p. V05AT08A026.
- [99] H. Al Abadi, H.-T. Thai, V. Paton-Cole, and V. Patel, “Elastic properties of 3d printed fibre-reinforced structures,” *Composite Structures*, vol. 193, pp. 8–18, 2018.
- [100] G. W. Melenka, B. K. Cheung, J. S. Schofield, M. R. Dawson, and J. P. Carey, “Evaluation and prediction of the tensile properties of continuous fiber-reinforced 3d printed structures,” *Composite Structures*, vol. 153, pp. 866–875, 2016.
- [101] R. M. Jones, *Mechanics of composite materials*. CRC press, 2018.
- [102] E. J. Barbero, *Introduction to composite materials design*. CRC press, 2010.

- [103] E. Carrera, M. Filippi, and E. Zappino, "Laminated beam analysis by polynomial, trigonometric, exponential and zig-zag theories," *European Journal of Mechanics-A/Solids*, vol. 41, pp. 58–69, 2013.
- [104] L. Euler, "Theory of elasticity," *Bousquet, Lausanne and Geneva*, 1744.
- [105] S. P. Timoshenko and J. N. Goodier, "Theory of elasticity," 1951.
- [106] S. Timoshenko, "On the correction for shear of the differential equation (or transverse vibration of prismatic bars)," *Philosophical Magazine*, vol. 41, pp. 744–746, 1921.
- [107] J. N. Reddy, "A simple higher-order theory for laminated composite plates," 1984.
- [108] A. Khdeir and J. Reddy, "Buckling of cross-ply laminated beams with arbitrary boundary conditions," *Composite Structures*, vol. 37, no. 1, pp. 1–3, 1997.
- [109] A. Khdeir and J. Reddy, "An exact solution for the bending of thin and thick cross-ply laminated beams," *Composite Structures*, vol. 37, no. 2, pp. 195–203, 1997.
- [110] A. Khdeir, "Dynamic response of antisymmetric cross-ply laminated composite beams with arbitrary boundary conditions," *International journal of engineering science*, vol. 34, no. 1, pp. 9–19, 1996.
- [111] K. Surana and S. Nguyen, "Two-dimensional curved beam element with higher-order hierarchical transverse approximation for laminated composites," *Computers & structures*, vol. 36, no. 3, pp. 499–511, 1990.
- [112] H. Matsunaga, "Interlaminar stress analysis of laminated composite beams according to global higher-order deformation theories," *Composite structures*, vol. 55, no. 1, pp. 105–114, 2002.
- [113] M. K. Rao, Y. Desai, and M. Chitnis, "Free vibrations of laminated beams using mixed theory," *Composite Structures*, vol. 52, no. 2, pp. 149–160, 2001.
- [114] R. P. Shimpi and Y. M. Ghugal, "A new layerwise trigonometric shear deformation theory for two-layered cross-ply beams," *Composites Science and Technology*, vol. 61, no. 9, pp. 1271–1283, 2001.

- [115] M. Tahani, “Analysis of laminated composite beams using layerwise displacement theories,” *Composite Structures*, vol. 79, no. 4, pp. 535–547, 2007.
- [116] H. Murakami, “Laminated composite plate theory with improved in-plane responses,” 1986.
- [117] E. Carrera, “Historical review of zig-zag theories for multilayered plates and shells,” *Appl. Mech. Rev.*, vol. 56, no. 3, pp. 287–308, 2003.
- [118] P. Vidal and O. Polit, “A family of sinus finite elements for the analysis of rectangular laminated beams,” *Composite Structures*, vol. 84, no. 1, pp. 56–72, 2008.
- [119] —, “Assessment of the refined sinus model for the non-linear analysis of composite beams,” *Composite Structures*, vol. 87, no. 4, pp. 370–381, 2009.
- [120] —, “A sine finite element using a zig-zag function for the analysis of laminated composite beams,” *Composites Part B: Engineering*, vol. 42, no. 6, pp. 1671–1682, 2011.
- [121] E. Oñate, A. Eijo, and S. Oller, “Simple and accurate two-noded beam element for composite laminated beams using a refined zigzag theory,” *Computer Methods in Applied Mechanics and Engineering*, vol. 213, pp. 362–382, 2012.
- [122] A. Tessler, M. Di Sciuva, and M. Gherlone, “A refined zigzag beam theory for composite and sandwich beams,” *Journal of Composite Materials*, vol. 43, no. 9, pp. 1051–1081, 2009.
- [123] E. Carrera, “Theories and finite elements for multilayered, anisotropic, composite plates and shells,” *Archives of Computational Methods in Engineering*, vol. 9, no. 2, pp. 87–140, 2002.
- [124] E. Carrera and G. Giunta, “Refined beam theories based on a unified formulation,” *International Journal of Applied Mechanics*, vol. 2, no. 01, pp. 117–143, 2010.
- [125] E. Carrera, M. Petrolo, C. Wenzel, G. Giunta, and S. Belouettar, “Higher order beam finite elements with only displacement degrees of freedom,” in *XIX Congresso AIMETA, Ancona (IT)*, 2009, pp. 1–11.
- [126] X. Xu, E. Carrera, H. Yang, E. Daneshkhah, and R. Augello, “Evaluation of stiffeners effects on buckling and post-buckling of laminated panels,” *Aerospace Science and Technology*, vol. 123, p. 107431, 2022.

- [127] E. Carrera, A. Pagani, and R. Augello, “Evaluation of geometrically nonlinear effects due to large cross-sectional deformations of compact and shell-like structures,” *Mechanics of Advanced Materials and Structures*, vol. 27, no. 14, pp. 1269–1277, 2020.
- [128] E. Carrera and M. Petrolo, “Refined beam elements with only displacement variables and plate/shell capabilities,” *Meccanica*, vol. 47, no. 3, pp. 537–556, 2012.
- [129] E. Carrera, A. G. de Miguel, and A. Pagani, “Hierarchical theories of structures based on legendre polynomial expansions with finite element applications,” *International Journal of Mechanical Sciences*, vol. 120, pp. 286–300, 2017.
- [130] M. Filippi, A. Pagani, M. Petrolo, G. Colonna, and E. Carrera, “Static and free vibration analysis of laminated beams by refined theory based on chebyshev polynomials,” *Composite Structures*, vol. 132, pp. 1248–1259, 2015.
- [131] E. Carrera, “Cz requirements—models for the two dimensional analysis of multilayered structures,” *Composite structures*, vol. 37, no. 3-4, pp. 373–383, 1997.
- [132] E. Carrera, M. Cinefra, M. Petrolo, and E. Zappino, *Finite element analysis of structures through unified formulation*. John Wiley & Sons, 2014.
- [133] M. Filippi and E. Carrera, “Capabilities of 1d cuf-based models to analyse metallic/composite rotors,” *Advances in aircraft and spacecraft science*, vol. 3, no. 1, p. 001, 2016.
- [134] A. Pagani and A. Sanchez-Majano, “Stochastic stress analysis and failure onset of variable angle tow laminates affected by spatial fibre variations,” *Composites Part C: Open Access*, vol. 4, p. 100091, 2021.
- [135] A. Pagani, M. Enea, and E. Carrera, “Component-wise damage detection by neural networks and refined fes training,” *Journal of Sound and Vibration*, vol. 509, p. 116255, 2021.
- [136] —, “Quasi-static fracture analysis by coupled three-dimensional peridynamics and high order one-dimensional finite elements based on local elasticity,” *International Journal for Numerical Methods in Engineering*, vol. 123, no. 4, pp. 1098–1113, 2022.

- [137] R. Azzara, E. Carrera, and A. Pagani, “Nonlinear and linearized vibration analysis of plates and shells subjected to compressive loading,” *International Journal of Non-Linear Mechanics*, vol. 141, p. 103936, 2022.
- [138] A. Pagani, A. de Miguel, and E. Carrera, “Cross-sectional mapping for refined beam elements with applications to shell-like structures,” *Computational Mechanics*, vol. 59, no. 6, pp. 1031–1048, 2017.
- [139] A. Viglietti, E. Zappino, and E. Carrera, “Analysis of variable angle tow composites structures using variable kinematic models,” *Composites Part B: Engineering*, vol. 171, pp. 272–283, 2019.
- [140] —, “Free vibration analysis of variable angle-tow composite wing structures,” *Aerospace Science and Technology*, vol. 92, pp. 114–125, 2019.
- [141] S. G. Lekhnitskii, “Anisotropic plates,” Foreign Technology Div Wright-Patterson Afb Oh, Tech. Rep., 1968.
- [142] T. J. Gordelier, P. R. Thies, L. Turner, and L. Johanning, “Optimising the fdm additive manufacturing process to achieve maximum tensile strength: a state-of-the-art review,” *Rapid Prototyping Journal*, 2019.
- [143] M. F. Afrose, S. Masood, P. Iovenitti, M. Nikzad, and I. Sbarski, “Effects of part build orientations on fatigue behaviour of fdm-processed pla material,” *Progress in Additive Manufacturing*, vol. 1, no. 1, pp. 21–28, 2016.
- [144] I. Durgun and R. Ertan, “Experimental investigation of fdm process for improvement of mechanical properties and production cost,” *Rapid Prototyping Journal*, 2014.
- [145] S. H. R. Sanei and D. Popescu, “3d-printed carbon fiber reinforced polymer composites: a systematic review,” *Journal of Composites Science*, vol. 4, no. 3, p. 98, 2020.
- [146] B. Akhouni and A. Behraves, “Effect of filling pattern on the tensile and flexural mechanical properties of fdm 3d printed products,” *Experimental Mechanics*, vol. 59, no. 6, pp. 883–897, 2019.
- [147] S. R. Rajpurohit and H. K. Dave, “Effect of process parameters on tensile strength of fdm printed pla part,” *Rapid Prototyping Journal*, 2018.

- [148] S. Ding, B. Zou, P. Wang, and H. Ding, “Effects of nozzle temperature and building orientation on mechanical properties and microstructure of peek and pei printed by 3d-fdm,” *Polymer Testing*, vol. 78, p. 105948, 2019.
- [149] C. Vălean, “Mars, avina.”
- [150] S. Masrol and W. A. Siswanto, “Stress concentration analysis of plate with circular hole: Elasticity theory and finite element comparison,” in *Applied Mechanics and Materials*, vol. 465. Trans Tech Publ, 2014, pp. 1385–1389.
- [151] A. M. G. Coelho, J. T. Mottram, and K. A. Harries, “Finite element guidelines for simulation of fibre-tension dominated failures in composite materials validated by case studies,” *Composite Structures*, vol. 126, pp. 299–313, 2015.
- [152] L. Li, Q. Sun, C. Bellehumeur, and P. Gu, “Composite modeling and analysis for fabrication of fdm prototypes with locally controlled properties,” *Journal of manufacturing processes*, vol. 4, no. 2, pp. 129–141, 2002.
- [153] E. Carrera, G. Giunta, and M. Petrolo, *Beam structures: classical and advanced theories*. John Wiley & Sons, 2011.
- [154] R. Azzara, E. Carrera, M. Filippi, and A. Pagani, “Time response stress analysis of solid and reinforced thin-walled structures by component-wise models,” *International Journal of Structural Stability and Dynamics*, vol. 20, no. 14, p. 2043010, 2020.
- [155] H.-S. Park and X.-P. Dang, “Structural optimization based on cad–cae integration and metamodeling techniques,” *Computer-Aided Design*, vol. 42, no. 10, pp. 889–902, 2010.
- [156] L. Luzi, A. Carloni, L. Agostini, R. Pucci, M. Refat, G. Berselli, and R. Vertechy, “3d printed resonant compliant mechanism to reduce motor torque requirements of machines with cyclic operation,” in *Smart Materials, Adaptive Structures and Intelligent Systems*, vol. 85499. American Society of Mechanical Engineers, 2021, p. V001T07A012.
- [157] C. Li, I. Y. Kim, and J. Jeswiet, “Conceptual and detailed design of an automotive engine cradle by using topology, shape, and size optimization,” *Structural and Multidisciplinary Optimization*, vol. 51, no. 2, pp. 547–564, 2015.

- [158] R. C. Shieh, “Massively parallel structural design using stochastic optimization and mixed neuralnet/finite element analysis methods,” *Computing Systems in Engineering*, vol. 5, no. 4-6, pp. 455–467, 1994.
- [159] B. MP and N. Kikuchi, “Generating optimal topologies in structural design using a homogenization method,” *Computer Methods in Applied Mechanics and Engineering*, vol. 71, pp. 197–224, 1988.
- [160] K. S. N. Kikuchi, “Layout optimization using the homogenization method,” *Optimization of large structural systems*, vol. 231, p. 157, 2013.
- [161] H. Eschenauer, A. Schumacher, and T. Vietor, “Decision makings for initial designs made of advanced materials,” in *Topology design of structures*. Springer, 1993, pp. 469–480.
- [162] Y. Xie and G. P. Steven, “Optimal design of multiple load case structures using an evolutionary procedure,” *Engineering computations*, 1994.
- [163] C. Schäfer and E. Finke, “Shape optimisation by design of experiments and finite element methods—an application of steel wheels,” *Structural and Multidisciplinary Optimization*, vol. 36, no. 5, pp. 477–491, 2008.
- [164] B. Poissenot-Arrigoni, A. Scheyer, and S. R. Anton, “Determination of orthotropic mechanical properties of 3d printed parts for structural health monitoring,” in *Sensors and Smart Structures Technologies for Civil, Mechanical, and Aerospace Systems 2017*, vol. 10168. International Society for Optics and Photonics, 2017, p. 101681D.
- [165] P. Bilancia, G. Berselli, L. Bruzzone, and P. Fanghella, “A cad/cae integration framework for analyzing and designing spatial compliant mechanisms via pseudo-rigid-body methods,” *Robotics and Computer-Integrated Manufacturing*, vol. 56, pp. 287–302, 2019.
- [166] J. Guo and K.-M. Lee, “Compliant joint design and flexure finger dynamic analysis using an equivalent pin model,” *Mechanism and Machine Theory*, vol. 70, pp. 338–353, 2013.
- [167] G. J. Monkman, S. Hesse, R. Steinmann, and H. Schunk, *Robot grippers*. John Wiley & Sons, 2007.

- [168] L. L. Howell, “Compliant mechanisms,” in *21st century kinematics*. Springer, 2013, pp. 189–216.
- [169] T. A. Dutra, R. T. L. Ferreira, H. B. Resende, and A. Guimaraes, “Mechanical characterization and asymptotic homogenization of 3d-printed continuous carbon fiber-reinforced thermoplastic,” *Journal of the Brazilian Society of Mechanical Sciences and Engineering*, vol. 41, no. 3, pp. 1–15, 2019.